STUDY ON THE CONTROL OF SUPERSONIC CAVITY FLOW OSCILLATIONS

September 2007

Department of Advanced Systems Control Engineering
Graduate School of Science and Engineering
Saga University

Md. Mahbubul Alam

STUDY ON THE CONTROL OF SUPERSONIC CAVITY FLOW OSCILLATIONS

By

Md. Mahbubul Alam

A dissertation submitted in partial fulfillment of the
requirement for the degree of

Doctor of Philosophy (Ph.D.)
in
Mechanical Engineering

Department of Advanced Systems Control Engineering
Graduate School of Science and Engineering
Saga University

September 2007

Supervisor: Professor Toshiaki Setoguchi

Graduate School of Science and Engineering
Saga University
Saga, Japan

CERTIFICATE OF APPROVAL

PH.D. THESIS

This is to certify that the Ph.D. thesis of

Md. Mahbubul Alam

has been approved by the Examining Committee
for the thesis requirement for the Doctor of
Philosophy degree at the September 2007 graduation.

Thesis committee:

Prof. Toshiaki Setoguchi (Supervisor)

Prof. Kenji Kaneko (Member)

Prof. Shigeru Matsuo (Member)

Prof. Kenbu Teramoto (Member)

ACKNOWLEDGMENTS

I gratefully acknowledge my sincere veneration, indebtedness and would like to express my profound gratitude and deep respect to my supervisor, Professor Toshiaki Setoguchi, Department of Mechanical Engineering, Saga University, for his valuable guidance, suggestions and encouragement through all phases of this research work. It is also a great honor and privilege for me to work with my supervisor and to share his valuable knowledge and expertise.

I wish to convey my sincere thanks and deep appreciations to Professor Shigeru Matsuo for providing valuable advice and supports during this research. His critical remarks and corrections have improved the quality of this thesis considerably.

I also wish to pay my gratefulness to Dr. Masanori Tanaka for his valuable suggestions and helpful supports during my research. I would also like to thank my lab-mates particularly Mr. Nishizaki, Mr. Kim, Mr. Alam, Mr. Umezaki, Mr. Nakano, and Mr. Higashi for their help and cooperation during my study.

I am especially indebted to the authority of Saga University, Japan Science Society, Japan Student Service Organization, Saga City for providing financial support to carry out this research work. Sincere appreciations are also due to the authority of CUET (Chittagong University of Engineering and Technology), Bangladesh, for granting the study leave/deputation and giving this opportunity to study in Japan.

I feel a deep sense of gratitude for my mother and late father who formed part of my vision and taught me the good things that really matter in life. The happy memory of my father still provides a persistent inspiration for my journey in this life. I am grateful for my brothers and sisters Faroque, Ferdous, Philip, Nazrul, Rasna, Hiron and Rehana, for rendering me the sense and the value of brotherhood. I am glad to be one of them.

I am very grateful to my wife Khadija, for her love and patience during the study period. Some of the best experiences that we lived through in this period were the birth of our daughters Mahiba Tasnim and Naysia Tazmin who provided an additional and joyful dimension to our life mission.

Finally, I would like to express my gratitude and thanks to all faculty members of the Department of Advanced Systems Control Engineering, Mechanical Engineering and the PSJP authority of Saga University for time to time help and suggestions in different aspects during my tenure at Saga University.

ABSTRACT

Control of cavity-induced pressure oscillations has been investigated numerically for a supersonic two-dimensional flow over open square cavities at Mach number 1.83 at the cavity entrance. A number of passive suppression techniques have been investigated by modifying the front wall of a square cavity with leading edge plates, sub-cavity, porous and spherical surfaces to determine the effectiveness of the proposed control methods on cavity-induced pressure oscillations.

The introduction of a sub-cavity near the front wall of the cavity covered by a leading edge plate helped to alter the oscillating shear layer in a favorable way so that some of the undesirable effects resulting from supersonic cavity flows were eliminated. It was observed that the upstream compression waves that impinged on the leading edge wall below the flat plat were not able to disturb the shear layer due to the obstruction imposed by the plate and consequently the amplitudes of the shear layer oscillations were greatly reduced. The introduction of the flat plate also prevents the formation of self-sustained feedback loop. The results also showed that the resultant amount of attenuation of cavity-induced pressure oscillations was dependent on the length and thickness of the leading edge plate, and also on the depth of the sub-cavity.

A sub-cavity with a porous wall near the front wall of the cavity covered by a flat plate had also been investigated to determine the effectiveness of proposed control method on the cavity-induced pressure oscillations. The simulation results of controlled cavity showed that the sub-cavity with the porous wall is effective in reducing the oscillations. The results also showed that the length of the leading edge plate and sub-cavity, porosity, the size of perforation of the porous wall had an influence in controlling the oscillations.

Simulations have also been done by modifying the front wall of the cavity with spherical surfaces to suppress the oscillations in a supersonic free stream flow. The results showed that the introduction of spherical surfaces in the cavity changed the flow field in a favorable way such that the upstream compression waves became weaker and the disturbance of the shear layer by the reflected compression waves was not strong enough to regenerate the instability waves to sustain the process by completing the feedback loop.

In order to validate the computational code developed for the present numerical simulation, a two-dimensional open square cavity of length to depth ratio = 1.0 at Mach number M_{inlet} =1.83 at the cavity entrance was investigated in case without control and the solutions were compared with the present experimental results. The comparison shows a fairly good agreement between the present simulated and experimental results. The results also show a good agreement with the experimental and theoretical results of other researchers.

Finally, a condensing flow was produced by an expansion of moist air in a Laval nozzle, and the effect of non-equilibrium condensation on the supersonic internal flows around the cavity is clarified numerically. The results showed that in the case with non-equilibrium condensation for a cavity with length to depth ratio =1.0, amplitudes of oscillation in the cavity became smaller than those without the non-equilibrium condensation. Furthermore, the occurrence of the non-equilibrium condensation reduced the peaks of power spectrum density and the frequency of the flow field oscillation increased in comparison with that of dry air.

CONTENTS

LIST OF TABLES

LIST OF FIGURES

NOMENCLATURE

Latin Symbols

a	speed of sound [m/s]
B	virial coefficient [m^3/kg]
c_p	specific heat at constant pressure [$J/(kg \cdot K)$]
C	various constants [-]
C_μ	turbulent model coefficient [-]
D	cavity depth [m]
$\boldsymbol{E}$	inviscid flux vector
e	internal energy per unit volume [J/m^3]
E_t	total energy per unit volume [J/m^3]
$\boldsymbol{F}$	inviscid flux vector
f	frequency [Hz]
f_μ	viscous damping function [-]
g	condensate mass fraction [-]
$\boldsymbol{H}$	turbulence source term
h	specific enthalpy [J/kg]
I	nucleation rate [$1/(m^3 \cdot s)$]
I_{hom}	nucleation rate by homogeneous condensation [$1/(m^3 \cdot s)$]
J	Jacobian (p.28)
k	turbulent kinetic energy [m^2/s^2]
k	Boltzmann constant) [J/K]
l	plate length [m]
L	cavity length [m]

L latent heat [J/kg]

M Mach number [-]

M molecular weight [kg/kmol]

n mode number [-]

p pressure [Pa]

P_k turbulence production rate [m^2/s^3]

Pr Prandtl number [-]

r droplet radius [m]

r_c critical droplet radius [m]

$\boldsymbol{R}$ viscous flux vector

R eddy viscosity [$Pa \cdot s$]

R radius of wall curvature [m]

$\Re$ gas constants [$J/(kg \cdot K)$]

Re Reynolds number [-]

R_t turbulent Reynolds number [-]

$\boldsymbol{S}$ viscous flux vector

S supersaturation [-]

St Strouhal number [-]

t time [s]

t plate thickness [m]

d depth of cut [m]

T temperature [K]

$\boldsymbol{U}$ Conservative vector

u, v Cartesian velocity components [m/s]

x, y Cartesian coordinates [m]

Greek Symbols

γ	ratio of specific heats [-]
κ	thermal conductivity [$\mathrm{W/(m \cdot K)}$]
μ	dynamic viscosity [$\mathrm{Pa \cdot s}$]
ν	kinematic viscosity [$\mathrm{(N \cdot s)/kg}$]
ρ	density [$\mathrm{kg/m^3}$]
σ	turbulent Schmidt number [-]
σ	surface tension) [N/m]
τ	shear stress [Pa]

Subscripts

hom	homogeneous
k	quantity in k equation
l	laminar
l	liquid
m	mixture
uni	universal
v	vapor
∞	plane surface
f	frozen
nc	without condensation
wc	with condensation
0	stagnation
R	quantity in R equation
t	turbulent

CHAPTER 1
INTRODUCTION

1.1 Motivation

High speed cavity flows can generate intense pressure oscillations that represent an important issue to be solved because of its harmful effects in many aerodynamic applications such as in-flight refueling ports, pressure vents in space shuttle's cargo bay, landing gears, projectiles, automotive and underwater vehicles, internal carriages of stores etc. These intense pressure oscillations may lead to the increase of the aircraft noise and drag, and may also cause equipment and instrumentation failure. Half century have past since Krishnamurty [1], Roshko [2] and later on Rossiter [3] investigated on the mechanism of cavity flow oscillations. Those pioneering studies were followed by numerous investigations addressing flow-induced cavity pressure oscillations and their control but the availability of data is inadequate especially for the supersonic flows.

The basic configuration of a cavity flow is shown in Fig. 1.1. The main features of this flow are the formation of a shear layer, which starts to roll up into large-scale vortical structures due to the Kelvin-Helmholtz instability. Compression waves are generated when these structures impinge on the trailing edge of the cavity. These compression waves propagate upstream to further excite the shear layer and thus a feedback loop is completed. This feedback loop often leads to self-sustained oscillations.

Techniques to suppress cavity-induced oscillations can be broadly classified as passive and active according to the requirement of the external energy input to the flow. Active control can offer better performance for a wide range of flow conditions but it needs additional cost and weight. The passive control techniques do not require external energy and are simple and inexpensive compared to the active ones. Therefore, passive control has been attracted many researchers and engineers in the resent years for its low cost and weight. The focus of this thesis is to determine the effectiveness of passive control to reduce or eliminate the self-sustained oscillations, for instance by using leading edge plate or sub-cavity near the front wall of a square cavity subjected to supersonic flows.

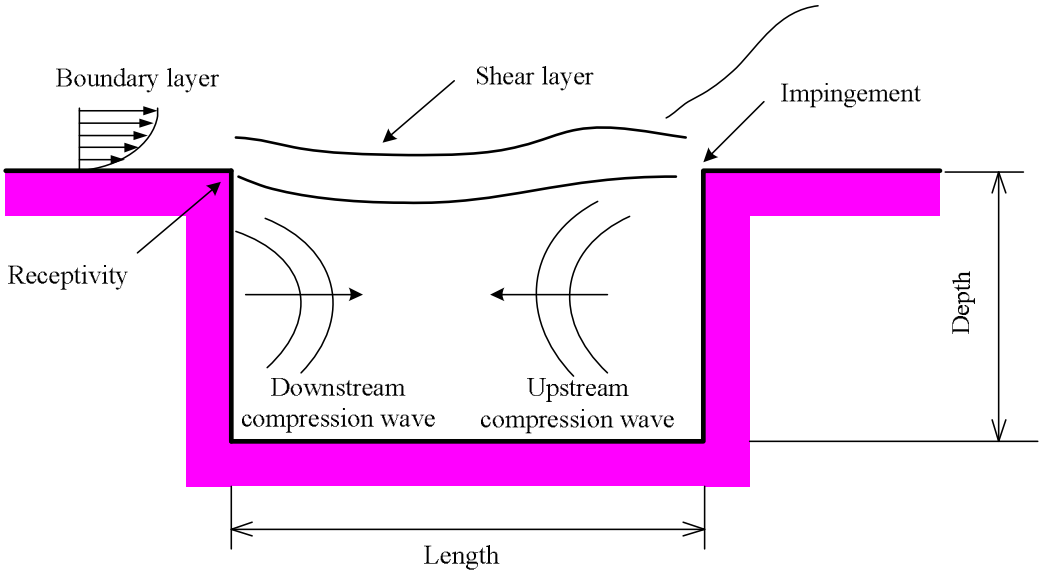

Figure 1.1: Basic cavity configuration.

1.2 Literature review

Numerous passive and active control devices had been tested by the earlier researchers to suppress the cavity-induced acoustic oscillations. Some of the passive control techniques including upstream vortex generator [4], slanted trailing edge [4], passive venting system [5, 6], leading edge sawtooth spoilers [7], passive bleed system [8], static or oscillating fences [9, 10], leading edge ramps [11], pins [12] and rods [13] had been shown to be successful in reducing cavity tones.

Heller and Bliss [4] conducted an experimental and analytical research program that studied several oscillations suppression devices such as slanting the trailing edge, upstream vortex generators or spoilers and some of those devices were able to suppress the oscillations significantly.

Wilcox Jr. [5] studied experimentally the effectiveness of passive venting system for modifying cavity flowfields at supersonic speeds by using a porous floor with a vent chamber underneath the floor. He obtained a large drag decrease for $L/D > 12$. For a cavity with $L/D = 17.5$ and $M_{inlet} = 2.86$, he obtained a steady reduction of drag with the increase of floor area and porosity percentage.

Shaw [7] conducted wind tunnel tests with cavities installed on a model of an aircraft to assess the leading-edge sawtooth suppressors and the slanted trailing edges. He found that the slanted trailing edge was very effective in attenuating cavity tones but the leading-edge spoilers were not fully successful.

Sarno and Franke [9] studied static and oscillating fences and also steady and pulsed injection at both subsonic and supersonic free stream flow velocities to

evaluate the effectiveness in suppressing cavity pressure oscillations. It was found that the static fences at the leading edge were the most effective in suppressing cavity pressure levels.

Ukeiley et al. [10] examined a leading-edge fence together with a cylindrical rod, placed in the oncoming boundary layer. They found that both of these devices were helpful in suppressing pressure loads in cavity flows.

Zhang et al. [11] studied numerically the unsteady flows over a shallow rectangular cavity at Mach 1.5 and 2.5 modifying the leading edge by using compression ramps, expansion surfaces, and mass injection. They reported two types of responses when a compression ramp is introduced at the leading edge of the cavity. A strong flapping motion leads to small changes in the frequency and sound pressure level in the cavity at Mach No. 1.5. At Mach No. 2.5, a weak shear layer instability produces an attenuation in the sound pressure level and the increased distance between the leading edge and the trailing edge helps in reducing the frequency. However, the mean pressure drag coefficient is also increased slightly when an expansion surface is employed at the leading edge of the cavity. They observed a reduction of the sound pressure level in the cavity with the height of the expansion surface.

Smith et al. [12] conducted an experimental test program to characterize the cavity-induced acoustic oscillations with microphone and flow visualization to suppress the oscillations. They used multi steps and pins to reduce the coherence of vortices by geometric changes of the upstream end of the cavity. They obtained reductions of acoustic amplitude by a factor of 5 and eliminated acoustic pressure oscillation in the cavity over the range of Mach numbers tested.

Smith et al. [13] conducted a series of wind tunnel tests to investigate the effectiveness of a passive rod spoiler on acoustic noise reduction. They reported that acoustic reduction was a function of rod diameter, boundary layer thickness, Mach number, shape and location with respect to the cavity leading edge. They also reported that rod spoilers showed potential as an effective passive suppression device of lower weight than conventional vertical or ramp spoilers.

McGrath and Shaw [14] studied cylindrical rods suspending in the approaching boundary layers to determine the effectiveness of control on cavity-induced pressure oscillation. They reported the first evience that the introduction of cylindrical rods in the approaching boundary layer could significantly suppress the cavity-induced pressure oscillation.

Shaw [15] reported two mechanisms of acoustic reduction using rod as a supperssion device. According to Shaw, the rod either displaces the boundary layer

to interrupt the formation of acoustic feedback loop, or the high frequency vortex shedding in the rod wake acts to extract energy from the larger oscillating structures. However, it is inconclusive to identify the suppression mechanism from the results of this study.

Mendoza and Ahuja [16] studied the control of cavity-induced pressure oscillation using steady mass injection through a thin slot located immediately upstream the cavity leading edge, along its span. They reported that mass injection through a single, thin, spanwise, slot positioned just upstream of the cavity leading edge can provide an almost complete suppression of cavity tones. The Mach number range studied was between 0.36 and 1.05. Attenuations in SPL up to 30 dB were achieved. Comparisons of boundary layer velocity profile measurements between upstream of the cavity leading edge and over the cavity with and without air injection showed an increase in the boundary layer thickness. According to them, this thickening of the boundary layer produced those noise reduction.

Hsu and Ahuja [17] conducted an experimental investigation on cavity acoustic oscillation control using a trailing-edge array of Helmholtz resonators. They obtained some suppression at lower Mach numbers. At intermediate Mach numbers, the control device reduced the magnitude of the targeted tone, but new tones appeared at other frequencies. They also found that the total noise reduction increased in linear fashion with the number of activated Helmholtz resonators.

Lamp and Chokani [18] studied numerically using a rotary valve actuator to provide steady and/or oscillatory blowing upstream of the cavity leading edge at a particular pulsing frequency. The cavity aspect ratio and the Mach number were 4.33 and 1.75, respectively. They placed a small jet within the cavity just below the front lip for forcing the shear layer with different amplitudes and frequencies. Their investigation showed that oscillatory blowing can suppress tone amplitudes provided the frequency to force the shear layer is not a harmonic of the cavity resonance.

Zhuang et al. [19] conducted an experimental investigation with the help of shadowgraph visualization, unsteady surface pressure measurements and particle image velocimetry and used supersonic microjets at the leading edge to suppress flow unsteadiness within the cavity. The reported how an oblique shock is formed at Mach number 2 that deflects the shear layer and alters its trajectory and the resulting impingement region. They also reported that the activation of microjets help to the attenuations of amplitudes of cavity tones up to 20 dB and reductions in the overall noise levels was more than 9 dB with a minimal mass flux. However, higher levels of mass flux produced no additional reductions.

The experimental studies of Clark [20] examined several turbulence reduction

techniques and various bay geometry features. He found that a 50 percent porosity leading edge fence served to reduce the pressure level better than other devices such as tangential blowing. Clark also found that there was small variation in his results over the limited Reynolds number and transonic Mach-number ranges studied.

The experimental studies of Kegerise et al. [21] and Cattafesta et al. [22] have used techniques to view the density variations of the various modes along with signal-processing techniques to show the evidence of mode switching between various Rossiter modes.

Jeng and Payne [23] conducted numerical experiments to study the flowfield and suppression of pressure oscillation in open cavity at supersonic flow. They found the controlling was most effective when the rear wall of the cavity was replaced with a porous wall.

Rizzetta and Visbal [24] performed large-eddy simulations of supersonic cavity flowfields including active flow control through pulsed mass injection at a very high frequency. They were able to suppress the resonant acoustic oscillatory modes.

Mongeau et al. [25] determined open-loop transfer functions for low-speed flow past a Helmholtz resonator at several different flow velocities. Their approach was to force the actuator at a range of frequencies, measure the response from the sensor, and then determine an empirical transfer function from the spectra. They used active spoiler driven via a moving coil loudspeaker and obtained a significant attenuation with small actuation effort.

Shaw and Northcraft [26] employed pulsed blowing system and a straight forward optimization algorithm to suppress the broadband noise levels and tones.

Vakili and Gauthier [27] studied steady normal mass injection through variable-density porous plates upstream of the cavity leading edge at Mach 1.8. They obtained significant suppression of oscillation with steady mass injection.

Stanek et al. [28] studied many different high frequency devices such as power resonance tube, cylindrical rod, passive resonance tube. The powered resonance tubes demonstrated significant tonal and broadband reduction and cylindrical rod produced significant suppression results for supersonic cavity flow. By comparing both low frequency and several high frequency suppression devices, they concluded that excitation of high frequency disturbances causes an acceleration of the turbulent energy cascade.

Cattafesta et al. [29] used piezoelectric flaps mounted at the leading edge of the cavity to suppress low-speed cavity oscillations. They obtained suppression of cavity tone at the first mode. However, the system involves moving parts with the risk of fatigue.

Baysal et al. [30] investigated computationally the effectiveness of rear face ramp and spoiler to suppress the cavity acoustics. They reported that those passive suppression devices are effective in reducing the sound pressure level.

Franke and Carr [31] conducted experimental investigations on a number of geometrically modified cavities such as vertical baffle, stores, spoilers and double cavity configurations for reducing flow-induced pressure oscillations. Their water table experiments showed that stores within the cavity were effective in reducing the oscillations when the stores touched the shear layer. Effectiveness was diminished when the store was positioned deeper in the cavity. A vertical baffle with approximately 45 percent open area positioned just upstream of the rear wall was also effective in suppressing the oscillations. However, the effectiveness was diminished when the baffle was placed near the center of the cavity. Double cavity configurations exhibited some interesting results that oscillations occurred within the cavities in phase and suppressing the oscillations in one cavity had no effect on the oscillations in the other cavity.

Dix and Butler [32] conducted series of experiments to determine the effect of cavity geometry and examine a variety of acoustic suppression devices. Their study showed that leading-edge spoilers are most effective in subsonic and transonic flows. However, the effectiveness of leading-edge spoilers were diminished in supersonic flows. A recent comprehensive review of several types of flow control devices in a cavity flow environment is given by Cattafesta et. al. [33]. Some representative control methods found in the literature are summarized in Table 1.

1.3 Objectives of research

As stated earlier, there have been very few studies that have studied the control of cavity-induced pressure oscillations subjected to supersonic free stream flows. The objectives of the present numerical investigation is to study passive control methods of reducing cavity-induced pressure oscillations in supersonic flow by modifying the geometry of the cavity near the front wall of a square cavity with a sub-cavity, porous surface and spherical surface. Experiments will be conducted in order to verify the validity of calculation results.

Again, many studies on the condensation occurring in the case of the rapid expansion of moist air or steam in a supersonic nozzle have been performed experimentally and numerically by other researchers and the characteristics of condensation have been nearly clarified. However, the effect of non-equilibrium condensation on the supersonic internal flows around the cavity has not yet been clarified satisfactorily. Therefore, another objective is to study the the effect of non-equilibrium

Table 1.1: Selected active and passive cavity flow control methods

Type	Control device	Effects	Study
Active control	Active spoiler with a loudspeaker	Significant attenuation achieved with small actuation effort	Mongeau et al.[25]
	Pulsed fluidic injection	Suppression of tones demonstrated but new tones appear at excitation frequency	Shaw and Northcraft [26]
	Perforated plate	Significant attenuation with steady mass injection	Vakili and Gauthier [27]
	Power resonance tubes	Suppression of flow-induced resonance	Stanek et al.[28]
	Piezoelectric flap actuator	Suppression of tone at the first mode	Cattafesta et al.[29]
Passive control	Ramps	Small reduction in SPL	Zhang et al.[11]
	Spoilers	Reduction of SPL	Baysal et al. [30]
	Fences	Suppression of dynamic pressure load	Ukeiley et al. [10]
	Stores	Effective in reducing the oscillations when the sores touch the shear layer	Franke et al. [31]
	Rods	Suppression of acoustic noise	Smith et al. [13]
	Porous plate	Suppression of cavity-induced pressure oscillations	Setoguchi et al. [34]
	Leading edge plate, sub-cavity	Suppression of pressure oscillations	Alam et al. [35]
	Spherical wall	Suppression of pressure oscillations	Matsuo et al. [36]

condensation numerically in order to clarify the effect of non-equilibrium condensation on the supersonic internal flows around the cavity. The objectives of the present study can be summarised as follows:

1. to study numerically the effect of passive control devices on cavity-induced pressure oscillations in supersonic flow by using leading edge plates, sub-cavity, porous surface and spherical surface.

2. to conduct experiments in order to verify the validity of calculation results.

3. to study the effect of non-equilibrium condensation numerically in order to clarify its effect on the supersonic internal flows around the cavity.

1.4 Outline of the dissertation

A survey of the literature associated with the research depicted in this dissertation is presented in Chapter 1. The physics of cavity flow, condensation phenomena and related theories are described in Chapters 2 and 3, respectively.

Numerical method used in this research is described in Chapter 4, which contains a description of the numerical scheme employed and also a description of the turbulence models used for the study. Chapter 5 presents the experimental setup and procedure.

In Chapter 6, the effects of leading edge plate and sub-cavity on the flowfield oscillations of square cavity (Cavity with aspect ratio = 1) are presented. The numerical results of cavity with different length and thickness of flat plates fitted at the leading edge of a square cavity subjected to two-dimensional supersonic flow are also presented in this chapter. Experimental investigation that conducted in order to verify the code developed for the numerical simulations is described in this chapter. Numerical results of rectangular cavities (Cavities with aspect ratio = 2 and 3) with and without leading edge plate are also presented in Chapter 6. Comparisons between experimental and numerical results are also discussed in this chapter.

Chapter 7 presents numerical results showing the reductions of cavity-induced pressure oscillations using a porous surface near the front wall of a square cavity. Numerical results of rectangular cavities (Cavities with aspect ratio = 2 and 3) with and without leading edge plate are also presented in Chapter 7. In Chapter 8, effects of spherical surface on the flowfield oscillations are presented.

Chapter 9 explains the effect of non-equilibrium condensation on the supersonic internal flows around the cavity.

Chapter 10 presents the conclusions of this thesis, and recommendations for future work. One of the possible applications of the proposed control methods is given in Appendix A. It presents the study of a passive control method for a supersonic flow at Mach number 1.83 at the entrance of a straight channel connected to an axi-symmetric nozzle. This is followed by bibliography.

CHAPTER 2
PHYSICS OF CAVITY FLOW

2.1 Cavity flow regimes and self-sustaining oscillations

Although the geometry of cavity is simple, flow over a cavity leads to a complex flow problem. The main areas of interest concerning cavity flow are the free stream flow, incoming boundary layer, shear layer, and the flow inside the cavity, all displayed in Fig. 1.1.

Generally, there are three categories of cavity flowfields such as open, closed and transitional depending primarily on the cavity length-to-depth ratio (L/D) [27]. The flowfield is termed as open when the cavity length-to-depth ratio is less than 8 and closed when length-to-depth ratio is greater than 13. Transitional cavity is within the intermediate region of L/D. Open cavities contain shear layer that separates from the upstream lip and reattaches downstream. Closed cavities are characterized by a shear layer that reattaches at the cavity floor, contain two large recirculation regions. The flow phenomenon associated with closed cavities is far more complicated because of the various interactions between the pressure waves and shear layer and shed vortices. The flow may behave as either an open cavity or a closed cavity flow in case of a transitional cavity. Cavity can also be classified as shallow or deep depending on length to depth ratio. If the cavity length to depth ratio is sufficiently large, longitudinal standing waves may exist and the cavity is termed as shallow cavity. On the contrary, if length to depth ratio is sufficiently small, transverse waves may exist and the cavity is termed as deep cavity. According to Heller et al. [37] shallow cavity behavior tends to occur for $(L/D) > 1$, while deep cavity behavior usually occurs for $(L/D) < 1$. However, the cavity flowfields depends not only on the length-to-depth ratio but also on the flow Mach number and the boundary-layer thickness at the leading edge of the cavity [38].

Usually there exists high dynamic pressure loads on the floor of the cavity in case of open cavity flow [39]. These high dynamic pressure loads are the result of vortex shedding, which is caused by unsteady flow in the shear layer [40]. The velocity of flow is supersonic above the shear layer and subsonic inside the cavity. These difference of velocities causes to form Kelvin-Helmholtz (K-H) instability which initiates a discrete spanwise vortex sheet at the leading edge of the cavity. As the vortex convects downstream, it grows and evolves until it reaches the trailing

edge of the cavity whereupon it interacts with the downstream wall of the cavity. According to Nishioka et al. [59], the generation of acoustic wave occurs when the shear layer instability wave impinges on the cavity trailing edge. This pressure wave impinges on the cavity leading edge to disturb the shear layer and stimulates the formation of another K-H vortex and the self-sustaining oscillations. According to Rockwell and Naudascher [41], this self-sustaining oscillations can be classified into the following types:

2.1.1 Fluid dynamic oscillations

According to Rockwell and Naudascher [41], fluid-dynamic oscillations are attributable to instability of the cavity shear layer and are enhanced through a feedback mechanism. They reported that fluid dynamic oscillations can occur if the ratio of the cavity length to the acoustic wave length is very small. If the free surface waves are absent in case of the liquids, fluid dynamic oscillations can also occur. They also reported that fluid dynamic oscillation have some common features like jet-edge type oscillation containing impingement of a free jet upon edge [42, 43] because of the primary mechanism for excitation of this type of oscillation is the increase of unstable disturbances in the cavity shear layer [44, 45, 46] and the oscillation is strongly developed by the existence of the downstream edge of the cavity.

2.1.2 Fluid-elastic oscillations

Fluid-elastic oscillations are primarily controlled by the elastic displacements of a solid boundary as reported by Rockwell and Naudascher. They also reported that the excitation is termed as fluid-elastic, if one or more walls of a cavity undergoes displacement and the displacement is great enough to exert feedback control on the shear layer perturbations during the cavity oscillations.

2.1.3 Fluid-resonant oscillations

According to Rockwell and Naudascher, fluid-resonant oscillations are governed by resonance conditions associated with compressibility or free-surface wave phenomena. The resonant cavity falls in the same category of other fluid-resonant phenomena, such as the screech tone generated by an under expanded supersonic jet [47]. The frequency of the cavity resonance is dominated by the cavity geometry and freestream velocity. A non-dimensional measurement of the frequency of the oscillations is the Strouhal number, defined as [41]:

$$St = \frac{fL}{U} \tag{2.1}$$

where St is the Strouhal number, f is the frequency, L is the length of the cavity, and U is the freestream velocity. To determine the Strouhal number, and subsequently the oscillation frequency (using known geometry and velocity), the Rossiter formula is used. Originally the Rossiter formula [3] was defined as:

$$St = \frac{n - C_1}{M + \frac{1}{C_2}} \tag{2.2}$$

where, n is the mode of the frequency present ($n = 1, 2, 3$), and C_1 and C_2 are constants which have been experimentally determined to be 0.25 and 0.57 respectively [48]. The values for n are often referred to as Rossiter modes. The Rossiter formula was subsequently modified by Heller et. al. to improve accuracy at higher levels of compressibility by assuming the cavity speed of sound is equal to the freestream speed of sound [37]. The preferred form of the Rossiter formula applied to compressible flow is the modified version defined as [41]:

$$St = \frac{fL}{U} = \frac{n - C_1}{\zeta + \frac{1}{C_2}} \tag{2.3}$$

where C_1, C_2 and n are as defined previously and ζ is a function of Mach number defined as:

$$\zeta = \frac{M}{\left(1 + \frac{\gamma - 1}{2} M^2\right)^{1/2}} \tag{2.4}$$

Based on given conditions, the expected frequency of the cavity resonance can be compared to a measured power spectral density (PSD) calculations for accuracy. The PSD provides the magnitude of the resonance (in dB) at specific frequencies. In other words, power spectral density is a measure of how the power in a signal depends on frequency. The higher the power spectral density is at any given frequency, the greater the pressure fluctuations at the point where the pressure is measured, usually from a fast response pressure transducer.

Murray and Elliott [48] investigated compressible shear layer over a cavity for L/D=3 utilizing Schlieren photography and planer laser imaging to study cavity flow for freestream conditions ranging from Mach 1.8 to Mach 3.5. Using the planer laser sheet lighting images, they clearly illustrated the decreased coherence of spanwise flow structures as the freestream Mach number was increased from 1.8 to 3.5.

They also report the convective velocity of the dominant structures in the shear layer vary laterally across the shear layer and the variation in convective velocity with Mach number was best represented by 0.57 times the freestream velocity.

Zhang and Edwards [49] reported that for a given cavity dimension, a cavity of a given L/D produces a higher level of fluctuation for a Mach 1.5 freestream than for a Mach 2.5 freestream. They investigated a variety of length-to-depth ratios and found that a transition from a relatively weak transverse oscillation to a relatively strong longitudinal oscillation occurs as L/D is increased from 1 to 3. Their data showed the standard deviation of the pressure normalized by the dynamic pressure of the freestream is a factor of three-to-four times higher for a Mach 1.5 freestream than for a Mach 2.5 freestream between $L/D = 3$ and $L/D = 5$. However, they do report the Mach 2.5 freestream leads to dominant modes.

Unalmis et al. [50] have reported results of a study of Mach 5 flow over a cavity for L/D=3 and L/D=7 using fast-response pressure transducers and laser sheet lighting. Interestingly, no evidence for coherent structures, typically induced by cavity acoustics at lower Mach numbers, was observed. Further, they reported substantially less coupling between the cavity pressure fluctuations and the shear-layer fluid dynamics as compared to similar flows with lower freestream Mach numbers. Lastly, they report that shock impingements on the trailing edge of the cavity are aperiodic for their conditions studied.

In a study of a cavity with L/D ranging from 4 to 7 and Mach numbers ranging from 0.8 to 3.0, Heller et al. [37] used a variable density wind tunnel to show the fluctuation level is very sensitive to the state of the incoming boundary layer in highly compressible flow environments. They measured a normalized spectral peak nearly 30 dB higher for a laminar boundary layer, compared to a turbulent boundary layer, for a Mach 3 freestream. This was not the case for lower Mach number values where the state of the incoming boundary layer had little, if any, affect on the pressure spectra. The transition from a laminar to turbulent layer is a function of the Reynolds number. The Reynolds number (Re) is defined as [51]:

$$Re = \frac{Vd}{\nu} \tag{2.5}$$

where V is the freestream velocity, d is the characteristic distance and ν is the kinematic viscosity. The critical Reynolds number for flow over a plate is 3.2×10^5, with lower values being laminar and greater values being turbulent [51]. The characteristic distance most frequently used in cavity flow experiments is the direction of the flow between the upstream edges of the test section and the cavity.

2.2 Theories for unsteady cavity oscillations

This chapter discusses different theories and mechanisms of unsteady flow phenomenon associated with a subsonic/ supersonic two-dimensional rectangular cavity. Because of the highly unsteady flow phenomenon associated with cavities, they are easier to visualize using numerical methods as opposed to experimental analysis. Computational methods are able to generate time histories of the entire flow field with relatively less computational effort, which enabling the better understanding of the physical mechanisms causing the cavity oscillations.

Researchers seem to be in some agreement that an oscillating shear layer exists and that the shear layer drives the primary and secondary vortices residing in the cavity. The pressure oscillations exist which cause the shear layer to shed. Coherent shed vortices, unsteady shock and pressure waves, and interaction between the shed vortex and the vortex that resides inside the cavity are present. Flow field characteristic appear to depend primarily upon the geometry of the cavity, inlet Mach number and the thickness of the boundary layer.

Apart from computing the unsteady cavity flow field, a good amount of effort has been directed in developing suppression devices to damp the oscillation of the cavity. Periara et al. measured the time averaged velocity characteristics of different cavity trailing edge geometries (sharp, nose shaped and round) using laser Doppler anemometry. Jeng [52] computed the effect of porous walls at front bulkhead and rear bulkhead to suppress the cavity oscillations. All this research focuses on understanding the effect of various active/passive flow control phenomenon.

Zhang and Edwards [49, 53, 54] have studied in detail various aspects of unsteady supersonic flow over a cavity. A Reiman solver with $k-\omega$ turbulence model was used for their studies. Inlet boundary condition consisted of boundary layer profile obtained from experiment. Part of their work involved capturing major feature of the cavity using Adaptive Mesh Refinement (AMR). They obtained results for length to depth ratio (L/D) for the cavity varying from 1 to 5. They found the unsteady motion to be random or regular based on the L/D ratio of the cavity. At short lengths (L/D =1-3) the measured pressure fluctuation was highly regular and repetitive. For larger value of $L/D > 3$ they found the measured pressure fluctuation became increasingly irregular. Though the oscillations were dominated by a single frequency, other harmonics of frequency started to appear with increase in L/D ratio of the cavity. Also they reported mode switching with laminar boundary layer with same boundary conditions as the earlier case. The mode switch is caused by shear layer instability and is attributed to vortex motion inside the cavity.

Tam et al. [55] have also performed extensive experimental and computational

analysis aimed at understanding the unsteady physical mechanism of the cavity flow oscillations. They used double thin layer Navier-Stokes (DTLNS) equations for their simulations. The upstream profile was determined from flat plate computations from which the proper profile was chosen by finding the x-location with same momentum boundary layer thickness. A complete description of the mechanism can be found in the section on unsteady oscillation mechanism.

Reynolds averaged Navier-Stokes equations with an algebraic turbulence model have been used in most analysis. More advanced model such as one- [56] and two- [49] equation model have also been attempted, although with no better result. The general results indicate that a wide variety of solutions can be obtained with various turbulence models, but that the large scale features are similar for all the models. Good results are typically obtained for time averaged properties like surface pressure and shear stress. However the unsteady properties like sound pressure levels and cavity resonance frequencies are not computed consistently.

Although a large amount of research effort has been directed toward understanding the cavity flow phenomenon, the parametric variation of these results with inlet parameters has not been reported. Zhang and Edward report that there at certain length and time scale cavity oscillations may be amplified by feedback from the shear layer and vice versa be damped at certain other frequencies.

In order to explain the unsteady flow physics of the cavity various researchers have suggested mechanisms for the cavity oscillations. Notable among them are efforts by Rossiter [3], Heller and Bliss [4], Rockwell and Naudascher [57], Tam et al. [58] and Nishioka et al. [59, 60].

2.2.1 Rossiter's empirical formula

Rossiter derived an empirical formula (Eq.2.2) for cavity resonance frequencies using dimensional analysis and empiricism. This formula predicts the dominant frequency and has been verified by various researchers. Rossiter's model was derived using edge tone analogy and the assumption that acoustic radiation is due to shed vortices impinging on the aft cavity wall. His experiments visualized the shed vortices and the pressure waves external to the cavity. His work laid foundation for more comprehensive theories regarding cavity resonance put forth by Heller and Bliss and Rockwell and Naudascher. Equation 2.2 was later modified by Heller et al. to account for the recovery factor measured to be close to unity rather then zero assumed by Rossiter. Thus, Rossiter's formula was improved for the higher Mach number range by assuming that the cavity sound speed is equal to the free stream stagnation sound speed. The modified Rossiter's formula becomes

$$St = \frac{fL}{U} = \frac{n - C_1}{\left[\frac{M}{\left(1+\frac{\gamma-1}{2}M^2\right)^{1/2}} + \frac{1}{C_2} \right]} \tag{2.6}$$

where C_1, C_2 and n are as defined previously.

2.2.2 Heller-Bliss empirical formula and wave interaction mechanism

The mechanism proposed by Heller and Bliss [4] and cited by several other researchers, defines the shear layer oscillation mechanism on the basis of steady compression waves. The upstream traveling compression wave reaches the front wall of the cavity and reflects. The resulting wave pattern in cavity causes unsteadiness in the shear layer. In turn, the shear layer motion is responsible for rear wall mass addition and removal that initially generated the cavity internal wave structure. Figure 2.1 shows the process of feedback loop in the cavity.

1. The pressure wave from previous trailing edge disturbance reaches the front wall of the cavity and reflects. Another wave, which has already reflected of the front wall, approaches the aft wall of the cavity. At the same time the shear layer is deflected above the aft wall and the fluid leaves the cavity.

2. A new compression wave begins to for at the aft wall as the flow impinges on the trailing edge causing the fluid to enter the cavity. The compression wave reflected from the front wall travels downstream.

3. The shear layer which is now below the trailing edge of the aft wall, form an upstream traveling compression wave. The reflected wave from the front wall continues to move downstream in phase with the shear layer displacement.

4. The upstream and downstream compression interacts near the cavity center.

5. After interaction the waves continue to move in their respective directions. The external part of the upstream traveling wave moves into the supersonic flow, thus causing it to be more tipped then the external flow Mach angle. The downstream wave moves in the same direction as the external flow and travels at supersonic speed.

6. The shear layer is now at the trailing edge. The wave generated at the trailing edge approaches the front wall of the cavity, and the downstream traveling wave approaches the aft wall of the cavity. The oscillation cycle then repeats.

Heller and Bliss using water table visualization technique by Shapiro [61], reported the pressure fluctuation in the cavity. Tam et al. [58] used simulated

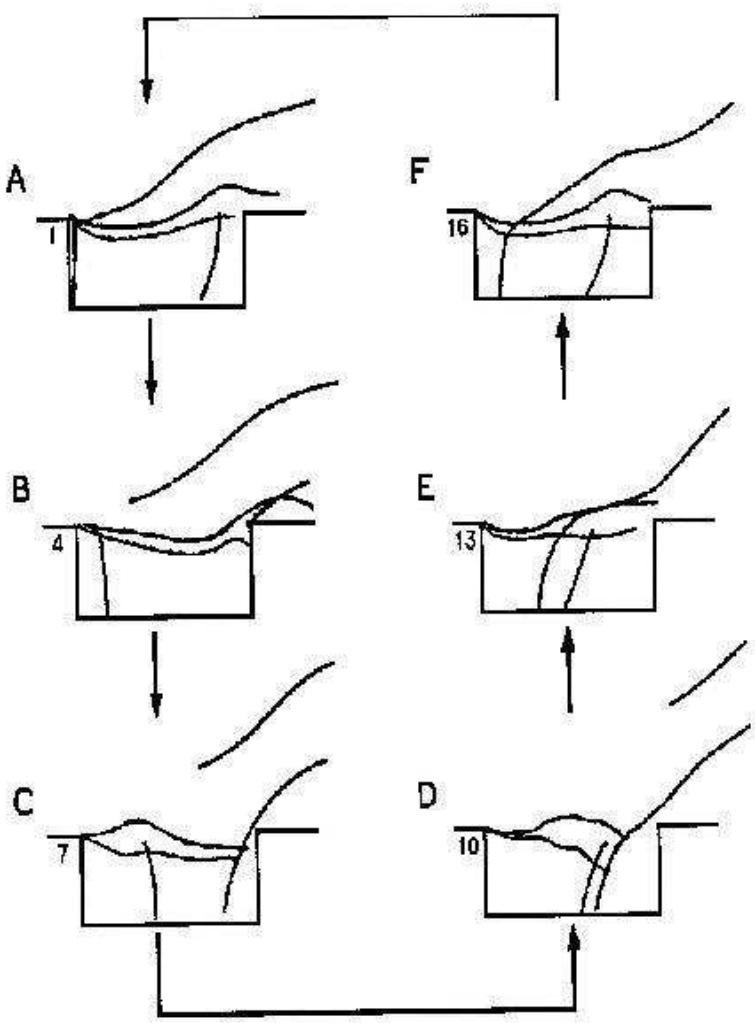

Figure 2.1: Heller and Bliss cycle [4].

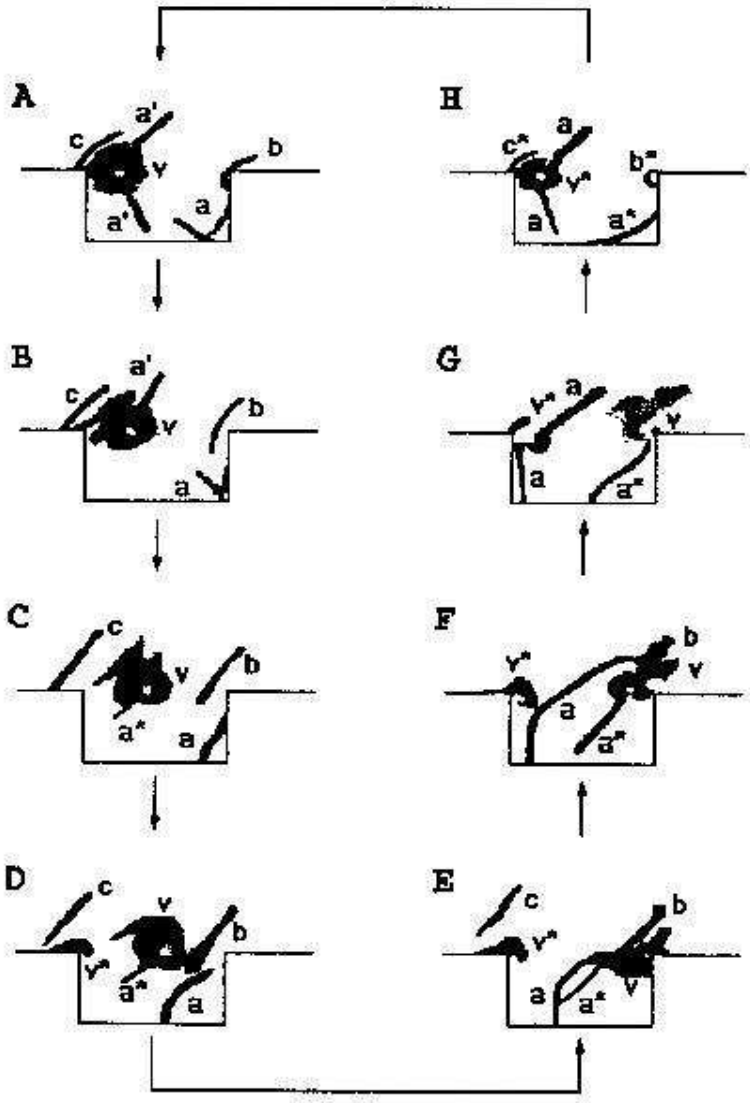

Figure 2.2: Schlieren pictures, Reference - Tam, et al.[58]

Schlieren pictures to explain the cyclic behavior. They reported important differences from the Heller and Bliss cycle. Their cycle is presented in Fig. 2.2. In particular,

1. Compression wave formed at the aft corner starts not from the previous cycle wave but from the wave just formed below the shed vortex.

2. The downstream traveling compression wave that has reflected off the front wall dissipates near the center of the cavity and does not strike the aft wall.

3. The upstream traveling compression wave does not have a component outside the cavity until it interacts with the downstream traveling compression wave.

4. Although the shed vortex and the vortex impingement are observed little

evidence exists to suggest that the torn vortex is responsible for the pressure oscillations. Further it seems to acts as a forcing function thus fixing the period of oscillation.

2.2.3 Vortex interaction mechanism

Rockwell and Naudascher [57] provided an explanation of the cavity resonance cycle, which stipulates that the shear layer oscillation is driven primarily by transient vortex motions within the cavity. Both water channel visualizations and laser Doppler anemometry were used to study the nature of this feedback mechanism. The flow visualization was achieved using hydrogen bubble technique in the water channel. It should be noted that this visualization technique is entirely different from the water-table visualization used by Heller and Bliss [4]. A water channel is an compressible flow visualization technique, whereas a water table visualization is a simulation of compressible flow fields. In addition, these two apparatus provide different flow features. For example a water table is used to see the pressure waves but not the shed vortices, and vice versa is true for water channel. In this Rockwell and Naudascher were able to detect the shed vortices that occurred with thin neither the shear layer nor the pressure waves. They proposed that the vortices which for with in the oscillation shear layer sometimes impinge upon the aft wall and produce upstream propagating disturbances within the cavity. These fluctuations travel forward and eventually displace the shear layer at the leading edge. This produces and external excitation of the shear layer that initiates and locks in the shedding of another vortex and closes the feedback loop show in Fig. 2.3.

2.2.4 Nishioka's empirical formula

Nishioka et al.[59] provided a detail explanation of self-sustaining oscillations in supersonic flow over rectangular cavities. They examined the generation and propagation processes of compression waves to clarify the feedback mechanism sustaining the oscillation. Figure 2.4 shows the process of feedback loop in the cavity.

At time $t = 154.2$ sec an upstream compression wave a, which was previously generated at the trailing edge, approaches the front wall with its lower portion already reflecting from the cavity floor, and at time $t = 157.5$ sec it is also reflecting from the front wall. At $t = 157.5$ sec, a new compression wave b is being generated close to the trailing edge. This wave b, identifying itself with a λ shaped wave from at $t = 160.7$ sec, accompanies a compression wave c. This wave c is propagating toward the bottom floor with a speed faster than wave b, and reflects from the floor between $t = 163.9$ sec and $t = 165.5$ sec. The whole wave pattern at $t = 165.5$

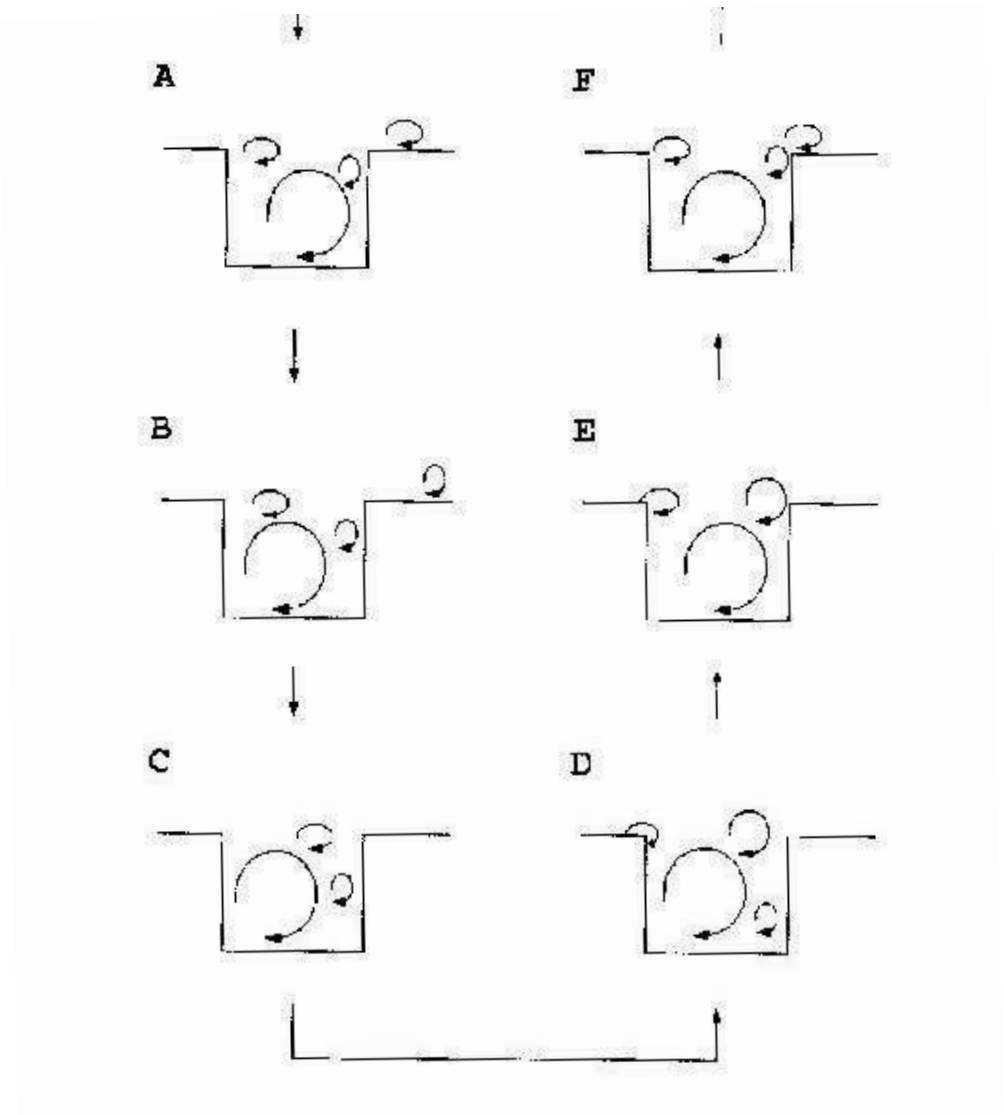

Figure 2.3: Vortex Interaction Mechanism [57]

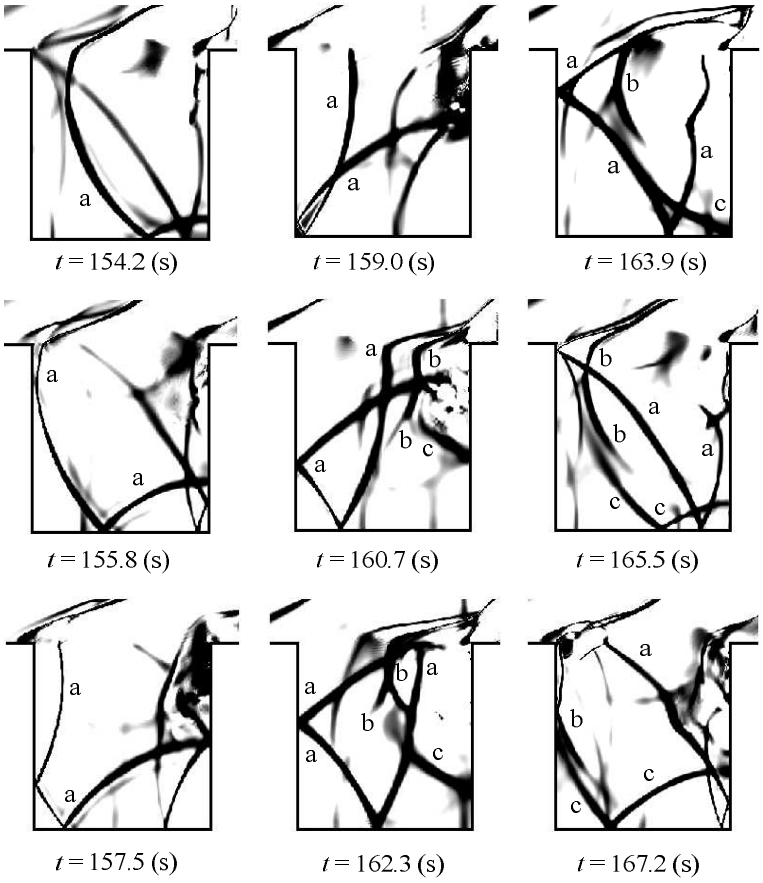

Figure 2.4: Compression waves vilualized by conrour maps of div $\boldsymbol{u}$ [59]

sec is essentially the same as that at time $t = 154.2$ sec, indicating that the flow is periodic with a period of 11.3.

They also proposed and derived a formula for the prediction of oscillation frequency, which expresses the resonance condition between the key phenomena such as generation, propagation and receptivity processes of compression waves governing the feedback mechanism. The formula as proposed by Nishioka et al.[60] is

$$St = \frac{fL}{U_\infty} = \frac{n}{\left[\beta M_\infty \left(1 + \frac{\gamma-1}{2} M_\infty^2\right)^{-1/2} + \frac{1}{K}\right]} \qquad (2.7)$$

$$n = 1,2,3, \ldots$$

with

$$\beta = (1 + 4D^2/L^2)^{1/2}, \quad K = U_c/U_\infty$$

2.3 Stabilization techniques for cavity oscillations

Flow control devices are either one of two types, passive or active, and are used to suppress the strong pressure fluctuations present in cavity flows. Passive approaches include the use of spoilers, cylindrical rods and stationary fences etc.[13, 28, 39]. Passive devices are designed to be extended into the incoming boundary layer to disrupt the formation of a coherent spanwise shear layer and prevent the formation of cavity resonance phenomena.

Active approaches include the use of oscillating fences [62], upstream blowing [63, 64], and acoustic resonators [28, 65]. All have been utilized to disrupt the evolution of well-organized spanwise vortical structures from the leading edge of the cavity. Oscillating fences are similar in design to stationary fences except they have a forcing function designed to oscillate the fence at a desired frequency. The desired oscillation frequency forces the shear layer at a frequency different from the cavity resonant frequency [9]. Upstream blowing is the injection of air through a jet, usually immediately upstream of the leading edge of the cavity. The jets can operate continuously or they can be pulsed, although experimental results have shown that continuous injection is more effective than pulsed injection [63]. Acoustic resonators can be low or high frequency relative to the predicted Rossiter modes with the newest research in high frequency areas. Experiments have shown high frequency resonators are able to reduce the resonance over all frequencies, not just specific frequencies as is the case with low frequency resonators [28].

CHAPTER 3
CONDENSATION PHENOMENA AND THEORY

3.1 Introduction

High speed flows with condensation may cause additional losses and development of instabilities which have direct impact on safety and efficiency of many technical applications. Condensation is the formation of liquid droplets from the vapor of a substance. It is well known that, depending on the pressure, a substance below its critical temperature can exists in either liquid or gaseous phase. This liquid or gaseous phase of a substance is referred to as a vapour. When this vapour undergoes expansion, condensation occurs and form liquid droplets. This phenomenon can be observed in nature in the process of creating clouds when some of water vapour present in the rising atmospheric air parcel turns into liquid water droplets as the air parcel expands and cools. The condensation phenomenon also observed in many technical and industrial applications e.g. in aircraft tip vortices and in industrial flows like steam turbines etc. Condensation may cause remarkable changes in the flow pattern with alteration of pressure and temperature significantly. This may also cause to develop additional shocks in the flowfield rendering the steady flow unsteady. The physics of condensation and theories pertaining to homogeneous nucleation are given in the subsequent sections.

3.2 Physics of condensation

Figure 3.1 shows the condensation precess in a schematic $p - v$ and $T - s$ diagram, respectively. The curve for the thermodynamical region of coexistence of vapour and liquid divides the plane into two regions. For pressures higher than the coexistence pressure the substance under consideration (water) exists in liquid phase and for the lower pressures the substance will be present as water vapour while in equilibrium. During the expansion of this condensable vapour in a supersonic nozzle, the thermodynamic state in the flow may approach the coexistence region. Let us consider a condensable vapour is expanding isentropically from a reservoir state at point $a(p_{01},\ T_{01})$ to a saturation state at point b (Fig.3.1) whose pressure and temperature are p_s and T_s, respectively. If the colling process is very slow, i.e., if the flow speed is sufficiently low, phase transition of vapours from the gaseous to the

liquid phase by condensation sets in and the expansion proceeds along the saturated isotrope *be* representing equilibrium condensation. For rapid expansions of vapour, the coexistence region is passed without the fluid attaining equilibrium. We consider an unsaturated water-vapor air mixture enters the nozzle as shown in Fig.3.2. Fall of temperature and expansion take place isentropically. Saturation is reached near the throat. The mixture becomes saturated and condensation nuclei are formed due to the nonexistence of condensation surface. If the expansion is very quick then the water vapour will not immediately condense under equilibrium conditions. This is the case as the characteristic time of the gas dynamic flow is much smaller than the time needed to form the first onsets of the new liquid phase. A state of high supersaturation is established that indicates a metastable non-equilibrium state of the vapour phase. The water-vapour expands further, driving the air-water-vapour mixture well away from equilibrium. In case the degree of supersaturation, $S > 1$ the fluid is said to be supersaturated. Degree of supersaturation is defined as the ratio of actual vapor pressure and the saturated vapour pressure. In the absence of foreign particles, the actual phase transition is preceded by homogeneous nucleation where the condensation nuclei form in the vapour phase itself. Formation of small liquid clusters, nuclei, at high supersaturation is the first stage of the condensation process that begins to stablish the equilibrium again. The supersaturated vapour condenses as a second step until equilibrium is reached and the precess can be regarded as the process of droplet growth. With much amount of liquid already present, the rest of the condensation process due to droplet growth takes place very close to thermodynamic equilibrium. An effect resulting from condensation is the release of latent heat during the condensation process. The latent heat $L(T)$ is given by a function of temperature [66].

$$L(T) = L_0 + L_1 T \tag{3.1}$$

$$\begin{aligned} L_0 &= 3105913.39 \qquad (\mathrm{J/kg}) \\ L_1 &= -2212.97 \times 10^{-2} \qquad (\mathrm{J/kg \cdot K}) \end{aligned}$$

The release of latent heat during the condensation process has a great influence on the flow pattern. If the amount of latent heat released is below some critical value then it causes a local increase of pressure, temperature and density only. For excessive heat release which exceeds this critical amount, the flow becomes thermally choked with aditional steady shocks appear in the nucleation zone. In this case different modes of self-excited oscillations is observed that alter the flow pattern completely.

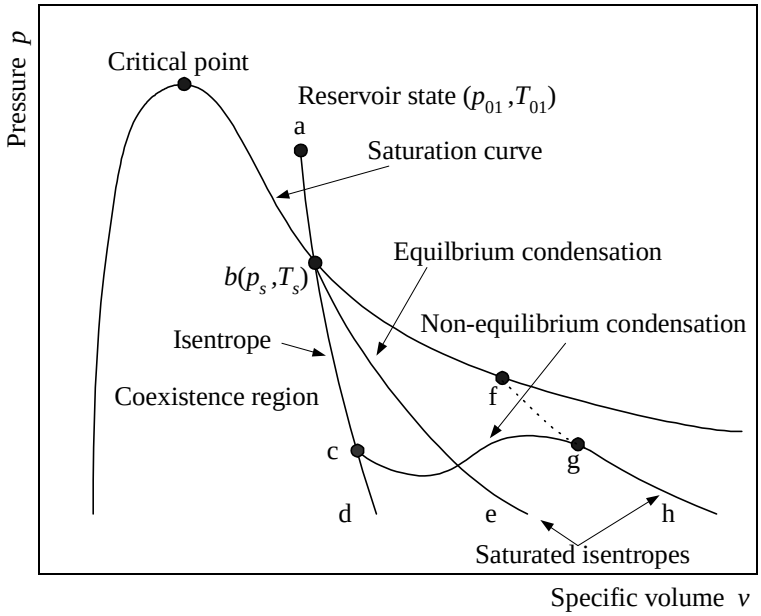

(a) p-v diagram

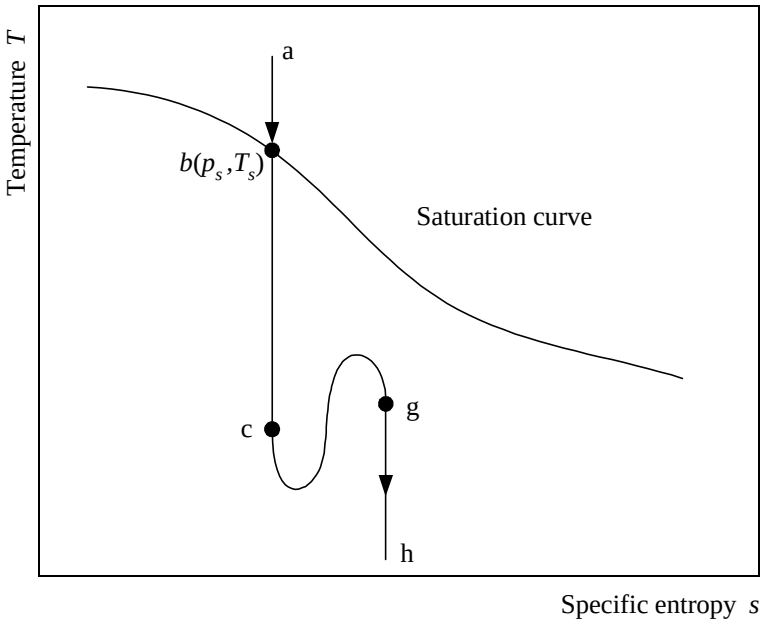

(b) T-s diagram

Figure 3.1: Sketch of the condensation process in a schematic p-v and T-s diagram

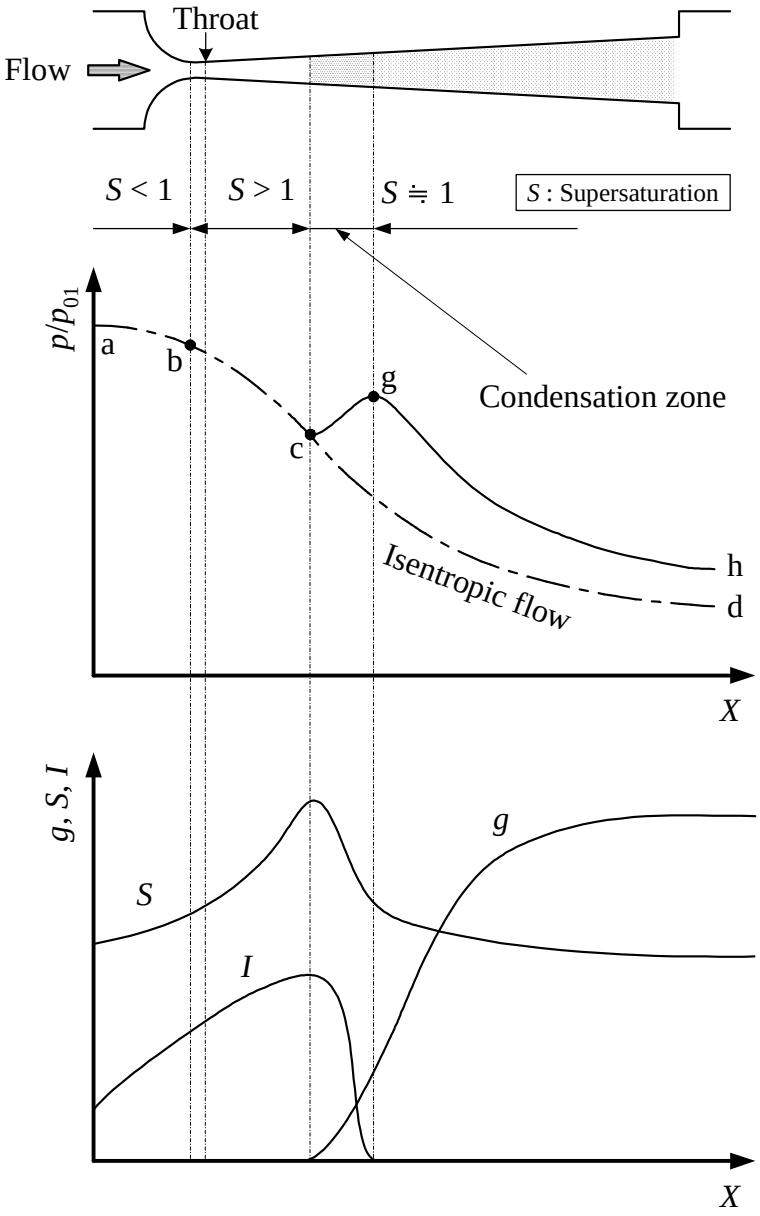

Figure 3.2: Sketch of the condensation process in a supersonic nozzle

3.3 Thermodynamic properties and conservation laws

We consider a mixture of a inert gas and a condensable vapor (water vapor), both are initially in the gaseous phase. Objective of this section is to characterise the thermo-fluid dynamic state of this mixture. The following assumptions were made

(1) both velocity slip and temperature difference do not exist between condensate droplets and inert gas.

(2) the mixture is thermally and calorically perfect

(3) the effects of condensate droplets on pressure are neglected.

(4) all particles are assumed to have smooth and spherical shape

(5) all condensation nuclei are assumed to be chemically inert.

The static pressure of mixture, under the hypothesis of an incompressible liquid phase, is simply the sum of the partial pressure of the gas components according to Dalton's law of partial pressure

$$p = p_a + p_v \tag{3.2}$$

Under the hypothesis of perfect gases, which is a reasonable assumption for the vapour and inert gas pressures considered in this thesis, it results

$$p_a = \frac{m_a}{V}\frac{\Re_{\text{uni}}}{M_a}T \qquad p_v = \frac{m_v}{V}\frac{\Re_{\text{uni}}}{M_v}T$$

Thus the equation of state for the whole mixture becomes

$$p = \left(\frac{m_a/V}{M_a} + \frac{m_v/V}{M_v}\right)\Re_{\text{uni}}T \tag{3.3}$$

here $\Re_{\text{uni}}$ is universal gas constant.

If we denote molecular weight of gaseous mixture by M_m and take $m = m_a + m_v$, the equation of state becomes

$$p = \frac{m}{V}\frac{\Re_{\text{uni}}}{M_m}T = \left(\frac{m_a}{V} + \frac{m_v}{V}\right)\frac{\Re_{\text{uni}}}{M_m}T \tag{3.4}$$

From Eq.3.2 and Eq.3.3, we have

$$\left(\frac{m_a}{V} + \frac{m_v}{V}\right)\frac{1}{M_m} = \frac{m_a/V}{M_a} + \frac{m_v/V}{M_v}$$

$$(m_a + m_v)\frac{1}{M_m} = \frac{m_a}{M_a} + \frac{m_v}{M_v}$$

$$\frac{1}{M_m} = \frac{m_a}{m_a + m_v}\frac{1}{M_a} + \frac{m_v}{m_a + m_v}\frac{1}{M_v} \tag{3.5}$$

Now the pressure p of gaseous mixture can be calculated by the following way

$$\frac{1}{M_m} = (1 - \frac{m_v}{m_a + m_v})\frac{1}{M_a} + \frac{m_v}{m_a + v}\frac{1}{M_v}$$

$$\frac{1}{M_m} = (1 - \omega)\frac{1}{M_a} + \omega\frac{1}{M_v}$$

where ω is the specific humidity defined by

$$\omega = \frac{m_v}{m_v + m_a} \tag{3.6}$$

Now introducing the above expression for M_m in Eq.3.3, the pressure p of gaseous mixture takes the following form

$$p = \rho_m \left((1 - \omega)\frac{1}{M_a} + \omega\frac{1}{M_v} \right) \Re_{\text{uni}} T \tag{3.7}$$

This is an equation of state for the gaseous mixture.

In addition to the above expressions, Mach number is also used in this research which is defined as the ratio of the actual velocity u at a given point to the velocity of sound a in the same gas at the conditions existing at this point. These are known as local conditions. Therefore, Mach number, M can be defined mathematically as

$$M = \frac{u}{a} \tag{3.8}$$

The velocity of sound can be calculated by the following way

$$a = \left(\gamma \frac{p}{\rho_m} \right)^{1/2} = \left(\frac{c_{p01}}{c_{p01} - \Re} \frac{p}{\rho_m} \right)^{1/2} = \left(\frac{c_{p01}}{c_{p01} - \frac{\Re_{\text{uni}}}{M_m}} \frac{p}{\rho_m} \right)^{1/2} \tag{3.9}$$

where, the isobaric specific heat, c_p and specific gas constant, $\Re$ of the mixture are defined as

$$c_p = c_{p01} \tag{3.10}$$

$$\Re = \Re_{\text{uni}}/M_m \tag{3.11}$$

The total mass of mixture m, present in a control volume V, is given by

$$m = m_a + m_v + m_l \tag{3.12}$$

where the subscripts a, v, l indicate the inert carrier gas, the vapour, and the liquid phase, respectively. The liquid mass fraction g is simply

$$g = \frac{m_l}{m} = \frac{m_l}{m_a + m_v + m_l} \tag{3.13}$$

Considering $m_v + m_l = m_{v01}$, we have

$$\frac{m_v + m_l}{m} = \frac{m_{v01}}{m} = \omega_{01} \tag{3.14}$$

Using Eq.3.4 and 3.12, we can write

$$\frac{1}{M_m} = \frac{m - m_{v01}}{m - m_l}\frac{1}{M_a} + \frac{m_{v01} - m_l}{m - m_l}\frac{1}{M_v}$$
$$\frac{1}{M_m} = \frac{1 - \omega_{01}}{1 - g}\frac{1}{M_a} + \frac{\omega_{01} - g}{1 - g}\frac{1}{M_v} \tag{3.15}$$

Now considering the mass of liquid droplet, m_l the Eq(3.4) becomes

$$p = \left(\frac{m - m_l}{V}\right)\frac{\Re_{\text{uni}}}{M_m}T = \left(\rho_m - \frac{m_l}{V}\right)\frac{\Re_{\text{uni}}}{M_m}T$$
$$= \rho_m\left(1 - \frac{m_l}{V\rho_m}\right)\frac{\Re_{\text{uni}}}{M_m}T = \rho_m\left(1 - \frac{m_l}{m}\right)\frac{\Re_{\text{uni}}}{M_m}T \tag{3.16}$$

Introducing the term liquid mass fraction, g in Eq(3.16), the expression for the pressure becomes

$$p = \rho_m(1 - g)\frac{\Re_{\text{uni}}}{M_m}T \tag{3.17}$$

Using the relation for M_m from Eq.3.4, the equation of state of gaseous mixture that includes the liquid drop takes the form

$$p = \left(\frac{1 - \omega_{01}}{M_a} + \frac{\omega_{01} - g}{M_v}\right)\rho_m\Re_{\text{uni}}T \tag{3.18}$$

Now the speed of sound, a_f and the Mach number, M_f can be calculated by the following way

$$a_f = \left(-\frac{\partial h/\partial p}{\partial h/\partial p - 1/\rho}\right)^{1/2} = \left(\frac{c_{p01}}{c_{p01} - (1 - g)\frac{\Re_{\text{uni}}}{M_m}}\frac{p}{\rho_m}\right)^{1/2} \tag{3.19}$$

$$M_f = \frac{u}{a_f} \tag{3.20}$$

The isobaric specific heat of gaseous mixture, c_{p01} is shown in the next formula

$$c_{p01} = \frac{m_a}{m}c_{pa01} + \frac{m_v}{m}c_{pv01}$$

using the term specific humidity, ω_{01}, the above expression takes the form

$$c_{p01} = (1 - \omega_{01})c_{pa01} + \omega_{01}c_{pv01} \tag{3.21}$$

In the similar way, the mass, co-efficient of viscosity and Prandtl number of gaseous mixture can be written as

$$m_{01} = (1 - \omega_{01})m_{a01} + \omega_{01}m_{v01} \tag{3.22}$$

$$\mu_{01} = (1 - \omega_{01})\mu_{a01} + \omega_{01}\mu_{v01} \tag{3.23}$$

$$Pr_{01} = (1 - \omega_{01})Pr_{a01} + \omega_{01}Pr_{v01} \tag{3.24}$$

3.4 Homogeneous condensation

Homogeneous condensation is already defined in the previous section. Different equations pertaining to homogeneous condensation are given below:

The condensate mass fraction g is expressed by a rate equation [67], given below

$$\frac{dg}{dt} = \frac{4\pi}{3} \cdot \rho_l \cdot r_c(t)^3 \cdot \frac{I(t)}{\rho_m(t)} + \int_{-\infty}^{t} 4\pi \cdot \rho_l \cdot \frac{I(\tau)}{\rho_m(\tau)} \cdot \frac{\partial r(t,\tau)}{\partial t} \cdot r(t,\tau)^2 d\tau \tag{3.25}$$

g : condensate mass fraction [$-$]

t : time [s]

ρ_l : density of liquid phase [kg/m^3]

$r_c(t)$: critical cluster radius [m]

$I(t)$: nucleation rate [1/(s $\cdot$ m^3)]

$\rho_m(t)$: density of gaseous mixture [kg/m^3]

$r(t,\tau)$: droplet radius [m]

The homogeneous condensation phenomena is modeled by the following two equations [68]

$$\frac{\partial(\rho_m \cdot g_{hom})}{\partial t} + \frac{\partial(\rho_m \cdot g_{hom} \cdot u)}{\partial x} + \frac{\partial(\rho_m \cdot g_{hom} \cdot v)}{\partial y} = \frac{4\pi}{3} \cdot \rho_l \cdot \left({r_{c,hom}}^3 \cdot I_{hom} + 3\rho_m \cdot n_{hom} \cdot {r_{hom}}^2 \cdot \frac{dr_{hom}}{dt} \right) \tag{3.26}$$

$$\frac{\partial(\rho_m \cdot n_{hom})}{\partial t} + \frac{\partial(\rho_m \cdot n_{hom} \cdot u)}{\partial x} + \frac{\partial(\rho_m \cdot n_{hom} \cdot v)}{\partial y} = I_{hom} \tag{3.27}$$

Each parameter of the above formulas are defined below [66]. In regard to the nucleation theory, the formula of Frenkel [69] which is one of the most typical type

on the basis of classical condensation theory, was used.

(a) Nucleation rate I_{hom} [$1/(\mathrm{s}\cdot\mathrm{m}^3)$]

$$I_{hom} = \frac{1}{\rho_l}\sqrt{\frac{2m_v\cdot\sigma_\infty}{\pi}}\left(\frac{p_v}{k\cdot T}\right)^2 \exp\left\{\frac{-4\pi\cdot {r_{c,hom}}^2\cdot\sigma_\infty}{3k\cdot T}\right\} \tag{3.28}$$

(b) Liquid droplet mean radius r_{hom} [m]

$$r_{hom} = \left(\frac{3}{4\pi}\cdot\frac{g_{hom}}{\rho_l\cdot n_{hom}}\right)^{\frac{1}{3}} \tag{3.29}$$

(c) Critical radius of the nuclei $r_{c,hom}$ [m]

$$r_{c,hom} = \frac{2\sigma_\infty}{\rho_l\cdot R_v\cdot T\cdot\ln\dfrac{p_v}{p_{s,\infty}} + (\rho_l\cdot B(T)-1)(p_v-p_{s,\infty})} \tag{3.30}$$

(d) Virial coefficient $B(T)$ [m^3/kg]

$$B(T) = b_0 + \frac{b_1}{T}\cdot\exp\frac{b_2}{b_3+T^2} \tag{3.31}$$

$$b_0 = 1.991502303\times10^3$$
$$b_1 = -2.210044139$$
$$b_2 = 3.0303704299\times10^5$$
$$b_3 = 4.398632810\times10^4$$

(e) Liquid droplet growth rate $\dfrac{dr_{hom}}{dt}$ [m/s]

$$\frac{dr_{hom}}{dt} = \frac{p_v - p_{s,r}}{\rho_l\sqrt{2\pi\cdot R_v\cdot T}} \tag{3.32}$$

(f) Saturation vapor pressure of condensate droplet with a radius r, $p_{s,r}$ [Pa]

$$p_{s,r} = p_{s,\infty} \cdot \exp \frac{2\sigma_\infty}{\rho_l \cdot R_v \cdot T \cdot r_{hom}} \tag{3.33}$$

(g) Flat film equilibrium vapor pressure $p_{s,\infty}$ [Pa]

$$p_{s,\infty} = \exp(A_9 + A_{10}T + A_{11}T^2 + B_1 \ln(T) + \frac{C_0}{T}) \tag{3.34}$$

$$\begin{aligned} A_9 &= 21.215 \\ A_{10} &= -2.7246 \times 10^{-2} \\ A_{11} &= 1.6853 \times 10^{-5} \\ B_1 &= 2.4576 \\ C_0 &= -6094.4642 \end{aligned}$$

(h) The surface tension in an infinite flat-film surface σ_∞ [N/m]

$$\sigma_\infty = \begin{cases} \{76.1 + 0.155 \times (273.15 - T)\} \times 10^{-3} & (T \geq 249.39 \text{ [K]}) \\ \{(1.1313 - 3.7091 \times 10^{-3} \times T) \times 10^{-4} - 5.6464\} \times 10^{-6} & \\ & (T < 249.39 \text{ [K]}) \end{cases} \tag{3.35}$$

(i) The density of liquid phase ρ_l [kg/m^3]

$$\rho_l(T) = \begin{cases} (A_0 + A_1 t + A_2 t^2 + A_3 t^3 + A_4 t^4 + A_5 t^5)/(1 + B_0 t) & (T \geq 0[^\circ C]) \\ (A_6 + A_7 t + A_8 t^2) & (T < 0[^\circ C]) \end{cases} \tag{3.36}$$

where t is the temperature and the coefficients are given by

$$\begin{aligned} A_0 &= 999.8396 & A_5 &= -393.2952 \times 10^{-12} \\ A_1 &= 18.224944 & A_6 &= 999.84 \\ A_2 &= -7.92221 \times 10^{-3} & A_7 &= 0.086 \\ A_3 &= -55.44846 \times 10^{-6} & A_8 &= -0.0108 \\ A_4 &= 149.7562 \times 10^{-9} & B_0 &= 18.159725 \times 10^{-3} \end{aligned}$$

(j) Other symbols

g_{hom} : Condensate mass fraction [−]

n_{hom} : The number of droplets per unit mass of moist air [1/kg]

u : Cartesian velocity components in x direction [m/s]

v : Cartesian velocity components in y direction [m/s]

m_v : mass per molecule of vapour [kg]

p_v : Vapor pressure [Pa]

k : Boltzmann constant [J/K]

T : Temperature [K]

R_v : Gas constant of vapor [J/kg · K]

CHAPTER 4
COMPUTATIONAL METHOD

This chapter deals with the basic equations that are used in the present numerical investigation. The equations are the two-dimensional unsteady compressible Navier-Stokes equations coupled with turbulence kinetic energy and eddy viscosity equations. This chapter also presents the turbulence model used in this simulation in detail. The equations which are employed as governing equations in this numerical study are given in the following sections.

4.1 Equations of motion

We assume that the flow is two-dimensional, compressible and unsteady, and hence is described by Navier-Stokes equations. For modelling the turbulence, we used a modified $k - R$ model [77, 78, 79] in computations. Therefore, the governing equations are the unsteady compressible Navier-Stokes equations coupled with turbulence kinetic energy and eddy viscosity equations. These equations are non-dimensionalized with reference values (a_o, L, ρ_o, μ_o and ν_0) at the inlet conditions upstream of the nozzle and can be written in two-dimensional Cartesian coordinate system (x, y) as

$$\frac{\partial \boldsymbol{U}}{\partial t} + \frac{\partial \boldsymbol{E}}{\partial x} + \frac{\partial \boldsymbol{F}}{\partial y} = \frac{1}{Re}\left(\frac{\partial \boldsymbol{R}}{\partial x} + \frac{\partial \boldsymbol{S}}{\partial y}\right) + \boldsymbol{H} \tag{4.1}$$

where

$$\boldsymbol{U} = \begin{bmatrix} \rho \\ \rho u \\ \rho v \\ E_t \\ \rho k \\ \rho R \end{bmatrix}, \qquad \boldsymbol{E} = \begin{bmatrix} \rho u \\ \rho u^2 + p \\ \rho uv \\ u(E_t + p) \\ \rho uk \\ \rho uR \end{bmatrix}, \qquad \boldsymbol{F} = \begin{bmatrix} \rho v \\ \rho uv \\ \rho v^2 + p \\ v(E_t + p) \\ \rho vk \\ \rho vR \end{bmatrix}$$

$$\boldsymbol{R} = \begin{bmatrix} 0 \\ \tau_{xx} \\ \tau_{xy} \\ \alpha \\ \left(\mu_l + \frac{\mu_t}{\sigma_k}\right)\frac{\partial k}{\partial x} \\ \left(\mu_l + \frac{\mu_t}{\sigma_R}\right)\frac{\partial R}{\partial x} \end{bmatrix}, \qquad \boldsymbol{S} = \begin{bmatrix} 0 \\ \tau_{yx} \\ \tau_{xy} \\ \beta \\ \left(\mu_l + \frac{\mu_t}{\sigma_k}\right)\frac{\partial k}{\partial y} \\ \left(\mu_l + \frac{\mu_t}{\sigma_R}\right)\frac{\partial R}{\partial y} \end{bmatrix}$$

and

$$\boldsymbol{H} = \begin{bmatrix} 0 \\ 0 \\ 0 \\ 0 \\ {P_k}' - \frac{\left(\rho k\right)^2}{\rho R} \\ (2 - C_{R1})\frac{R}{k}{P_k}' - (2 - C_{R2})\rho k - \frac{\rho C_\mu}{\sigma_R}\left[\left(\frac{\partial R}{\partial x}\right)^2 + \left(\frac{\partial R}{\partial y}\right)^2\right] \end{bmatrix}$$

where $\boldsymbol{U}$ is the conservative vector, $\boldsymbol{E}$ and $\boldsymbol{F}$ are the inviscid flux vectors and $\boldsymbol{R}$ and $\boldsymbol{S}$ are the viscous flux vectors. $\boldsymbol{H}$ is the turbulence source term. k and R are the turbulence kinetic energy and eddy viscosity, respectively. $\tau_{xx}, \tau_{xy}, \tau_{yx}$ and τ_{yy} are components of the viscous shear stress. μ_l and μ_t are the laminar and the turbulent viscosities, respectively. The expressions for the total energy E_t, ratio of specific heats at constant pressure in stagnation condition C_{p0}, pressure p, α and β take the following forms

$$E_t = \rho C_{p0} T + \frac{1}{2}\rho(u^2 + v^2)$$

$$C_{p0} = \frac{\gamma_0}{\gamma_0 - 1} R$$

$$p = (\gamma_0 - 1)\left[E_t - \frac{1}{2}\rho(u^2 + v^2)\right]$$

$$\alpha = u\tau_{xx} + v\tau_{yx} + k\frac{\partial T}{\partial x}, \qquad \beta = u\tau_{xy} + v\tau_{yy} + k\frac{\partial T}{\partial y}$$

where γ_0 is the ratio of specific heats at stagnation condition. The equations for

the turbulence production and limiter function are given in section 3.3.2.

The governing equations used in the simulation in case of cavity with non-equilibrium condensation were the unsteady compressible Navier-Stokes equations and a rate of liquid-phase production [67] in a two-dimensional coordinate system. The governing equation systems that are non-dimensionalized with reference values at the inlet conditions upstream of the nozzle are given as follows

$$\frac{\partial \boldsymbol{U}}{\partial t} + \frac{\partial \boldsymbol{E}}{\partial x} + \frac{\partial \boldsymbol{F}}{\partial y} = \frac{1}{Re}\left(\frac{\partial \boldsymbol{R}}{\partial x} + \frac{\partial \boldsymbol{S}}{\partial y}\right) + \boldsymbol{Q} \tag{4.2}$$

where

$$\boldsymbol{U} = \begin{bmatrix} \rho_m \\ \rho_m u \\ \rho_m v \\ E_t \\ \rho_m g \\ \rho_m D_1 \\ \rho_m D_2 \\ \rho_m D_3 \end{bmatrix}, \qquad \boldsymbol{E} = \begin{bmatrix} \rho_m u \\ \rho_m u^2 + p \\ \rho_m uv \\ u(E_t + p) \\ \rho_m ug \\ \rho_m uD_1 \\ \rho_m uD_2 \\ \rho_m uD_3 \end{bmatrix}, \qquad \boldsymbol{F} = \begin{bmatrix} \rho_m v \\ \rho_m uv \\ \rho_m v^2 + p \\ v(E_t + p) \\ \rho_m vg \\ \rho_m vD_1 \\ \rho_m vD_2 \\ \rho_m vD_3 \end{bmatrix}$$

$$\boldsymbol{R} = \begin{bmatrix} 0 \\ \tau_{xx} \\ \tau_{xy} \\ \alpha \\ 0 \\ 0 \\ 0 \\ 0 \end{bmatrix}, \qquad \boldsymbol{S} = \begin{bmatrix} 0 \\ \tau_{yx} \\ \tau_{xy} \\ \beta \\ 0 \\ 0 \\ 0 \\ 0 \end{bmatrix}, \qquad \boldsymbol{Q} = \begin{bmatrix} 0 \\ 0 \\ 0 \\ 0 \\ \rho_m \dot{g} \\ \rho_m \dot{D}_1 \\ \rho_m \dot{D}_2 \\ \rho_m \dot{D}_3 \end{bmatrix}$$

where $\boldsymbol{U}$ is the conservative vector, $\boldsymbol{E}$ and $\boldsymbol{F}$ are the inviscid flux vectors and $\boldsymbol{R}$ and $\boldsymbol{S}$ are the viscous flux vectors. $\boldsymbol{Q}$ is the condensation source term. $\tau_{xx}, \tau_{xy}, \tau_{yx}$

and τ_{yy} are components of the viscous shear stress. The expressions for the total energy E_t, pressure p, α and β are given below

$$E_t = \rho_m C_{p0} T + \frac{1}{2}\rho_m(u^2 + v^2) - \rho_m g L$$

$$p = G\left[E_t - \frac{1}{2}\rho_m(u^2 + v^2) + \rho_m g L\right]$$

$$G = \left(1 - g \cdot \frac{M_m}{M_v}\right) \Big/ \left(\frac{1}{\gamma - 1} + g \cdot \frac{M_m}{M_v}\right)$$

$$\alpha = u\tau_{xx} + v\tau_{yx} + k\frac{\partial T}{\partial x}, \quad \beta = u\tau_{xy} + v\tau_{yy} + k\frac{\partial T}{\partial y}$$

The condensate mass fraction $\dot{g}$ is given by a rate equation [67], expressed by the following

$$\dot{g} = \frac{dg}{dt} = \frac{\rho_l}{\rho_m}\left(\frac{4\pi}{3}{r_c}^3 I + \rho_m D_1 \frac{dr}{dt}\right) \tag{4.3}$$

In Eq.5.38, $\dot{D_1}, \dot{D_2}$ and $\dot{D_3}$ are given as

$$\dot{D_1} = \frac{dD_1}{dt} = \frac{4\pi {r_c}^2 I}{\rho_m} + D_2 \frac{dr}{dt}$$

$$\dot{D_2} = \frac{dD_2}{dt} = \frac{8\pi r_c I}{\rho_m} + D_3 \frac{dr}{dt}$$

$$\dot{D_3} = \frac{dD_3}{dt} = \frac{8\pi I}{\rho_m}$$

The governing equation systems that are non-dimensionalized with reference values at the inlet conditions upstream of the nozzle are mapped from the physical plane into a computational plane by a general transform. To close the governing equations, a modified $k-R$ model[77, 78, 79] is employed in computations. A third-order TVD (Total Variation Diminishing) finite difference scheme with MUSCL[73] is used to discretize the spatial derivatives and a second order-central difference scheme for the viscous terms, and a second-order fractional step is employed for time integration.

4.2 TVD schemes

TVD stands for Total Variation Diminishing. The idea of the TVD Scheme was first introduced by Harten [71].

Let us consider the 1D Euler equations in a conservative form

$$\frac{\partial u}{\partial t} + \frac{\partial F}{\partial x} = 0 \quad F = F(u)$$

The total variation (TV) for any physically realisable solution can be written by the following equation

$$TV = \int \left| \frac{\partial u}{\partial x} \right| dx$$

In term of numerical solution of

$$\frac{\partial u}{\partial t} + \frac{\partial F}{\partial x} = 0$$

where $\frac{\partial u}{\partial x}$ can be discretised by $\frac{u_{j+1}-u_j}{\Delta x}$, then, the total variation is given by

$$TV = \sum_j |u_{j+1} - u_j|$$

A numerical method is said to be total variation diminishing (TVD) if it does not increase the total variation of the solution, i.e.,

$$TV\left(n^{n+1}\right) \leq TV\left(n^n\right)$$

The TVD schemes are very popular in the area of CFD for computing the phenomena of shock waves without presenting the spurious oscillations. However, only first order linear systems are TVD and preserve monotonicity [72]. Monotone schemes are effective in computing fluid dynamic problems because they do not select non-physical solutions. Higher order classical upwind and symmetric schemes are not TVD and have the following drawbacks [73]: (1) they produce spurious oscillations whenever the solution is not smooth, (2) they may develop nonlinear instabilities in the presence of discontinuities, and (3) the scheme may provide non-physical solutions.

In order to avoid those undesirable results, but retaining the monotone behavior, various high resolution, non-linear techniques have been developed. These high resolution, non-linear techniques often use limiters in order to make the solutions total variation diminishing (TVD). The techniques that make the higher order schemes TVD can be group into two general approaches. These are (1) the MUSCL (Monotonic Upstream Schemes for Conservation Lows) approach, and (2) the non-MUSCL approach. The MUSCL technique originally developed by van Leer is a suitable technique for obtaining a higher order accurate TVD scheme. The idea of MUSCL approach is to replace the piecewise constant approximation of Godunov's

scheme by reconstructed states, derived from cell-averaged states obtained from the previous time-step. The reconstructed right and left states with slope limited are obtained for each cell. These reconstructed states are used to calculate fluxes at the cell boundaries. These fluxes at the cell boundaries are used as input to the approximate Riemann solver. Later on, average results are obtained from the Riemann solver solutions. Finally, these average are used to advance the solution in time.

4.3 Models for the turbulence

Although there is an increasing confidence in CFD community to solve the Navier Stokes equations on modern computers, that confidence is limited to laminar flows only. But, most flows of practical engineering interest are turbulent, and the turbulent mixing of the flow then usually dominates the behaviour of the fluid. Although there have been some solutions of the Navier Stokes equations directly for turbulent flows (a process known as DNS for direct numerical simulation), these computations are not useful for engineering analysis. They require extensive computer resources, are applicable only to simple geometries, and do not directly provide the average quantities of interest in engineering design. Therefore, instead of direct simulation, CFD applications dealing with turbulent flow use models. These models range from simple algebraic models to those which require the solution of one or more partial differential equations.

4.3.1 Eddy-viscosity model

The most frequent used turbulence models by CFD community are the Eddy-Viscosity- Models (EVMs). The concept behind the eddy-viscosity models are that the unknown Reynolds stresses, a consequence from the averaging procedure, are modelled using flow parameters and an eddy-viscosity. The pioneering eddy-viscosity model is the $k-\epsilon$ model of Jones and Launder [74]. This $k-\epsilon$ model which appeared in 1972 has been followed by numerous eddy-viscosity models, most of them based on the k-equation and an additional transport equation, such as the $k-\omega$ [75], the $k-\tau$ [76] and $k-R$ [77, 78, 79] models. There also exist three and four equations models, which use the two-equation model concept as a basis. The latter class includes models such as the model of Durbin [81] and the model of Suga et al. [82]. The improvement of eddy-viscosity model, especially their near-wall accuracy has been possible now with the emerging Direct Numerical Simulations (DNSs). The first accurate DNS was made by Kim et al. [80] although at a low Reynolds number and for a simple fully developed channel flow test case. Now a

days, DNS's are made at both high Reynolds numbers, and of more complex flows, enabling accurate and advanced eddy-viscosity models to come out.

4.3.2 Goldberg's $k-R$ model

A modified version of the Baldwin-Barth $k-R$ two-equation turbulence model proposed by Goldberg [77] is used in the present numerical investigation. In this model, Goldberg used the near-wall function based on the ratio of the large eddy and the Kolmogorov time scales. This model is applicable to both wall-bounded and free shear flows and does not require explicit knowledge of local distance to walls. This is also applicable to both structured and unstructured computational frameworks for flow predictions involving complex geometries. The details about the turbulence model used in the present numerical simulation are given in the following sections.

4.3.2.1 The transport equation

The transport equation in orthogonal coordinate system can be written as

$$\frac{\partial \boldsymbol{U}}{\partial t}+\frac{\partial \boldsymbol{E}}{\partial \xi}+\frac{\partial \boldsymbol{F}}{\partial \eta}=\frac{\partial \boldsymbol{R}}{\partial \xi}+\frac{\partial \boldsymbol{S}}{\partial \eta}+\boldsymbol{H}$$

$$\boldsymbol{U}=\begin{pmatrix}\rho k\\ \rho\mathcal{R}\end{pmatrix},\quad \boldsymbol{E}=\begin{pmatrix}\rho k u\\ \rho\mathcal{R}u\end{pmatrix},\quad \boldsymbol{F}=\begin{pmatrix}\rho k v\\ \rho\mathcal{R}v\end{pmatrix}$$

$$\boldsymbol{R}=\begin{pmatrix}(\mu_l+\frac{\mu_t}{\sigma_k})\frac{\partial k}{\partial x}\\ (\mu_l+\frac{\mu_t}{\sigma_R})\frac{\partial \mathcal{R}}{\partial x}\end{pmatrix},\quad \boldsymbol{S}=\begin{pmatrix}(\mu_l+\frac{\mu_t}{\sigma_k})\frac{\partial k}{\partial y}\\ (\mu_l+\frac{\mu_t}{\sigma_R})\frac{\partial \mathcal{R}}{\partial y}\end{pmatrix}$$

$$\boldsymbol{H}=\begin{pmatrix}P_k-\frac{\rho k^2}{\mathcal{R}}\\ (2-C_{R1})\frac{\mathcal{R}}{k}P_k-(2-C_{R2})\rho k-\rho\frac{C_\mu}{\sigma_R}\{(\frac{\partial \mathcal{R}}{\partial x})^2+(\frac{\partial \mathcal{R}}{\partial y})^2\}\end{pmatrix}$$

where $\sigma_k, \sigma_R, C_{R1}, C_{R2}, C_\mu$ are constant and have the following values

$$\sigma_k=1.0,\quad \sigma_R=1.080,\quad C_{R1}=1.44,\quad C_{R2}=1.92,\quad C_\mu=0.09$$

and the near wall damping function f_μ is given as

$$f_\mu=\frac{\tanh(\alpha' R_t)}{\tanh(\beta' R_t)}$$

where

$$\alpha'=0.005,\quad \beta'=\frac{C_\mu^{3/4}}{k}$$

$$k^2=\sigma_R\sqrt{C_\mu}(C_{R2}-C_{R1})$$

P_k is the turbulent production modeled in terms of the Boussinesq concept

$$P_k = [\mu_t(\frac{\partial u_i}{\partial x_j} + \frac{\partial u_j}{\partial x_i} - \frac{2}{3}\frac{\partial u_k}{\partial x_k}\delta_{ij}) - \frac{2}{3}\rho k\delta_{ij}]\frac{\partial u_i}{\partial x_j}$$

In two-dimensional form

$$P_k = \mu_t[2(u_x^2 + v_y^2) + (u_y + v_x)^2 - \frac{2}{3}(u_x + v_y)^2] - \frac{2}{3}\rho k(u_x + v_y)$$

The eddy viscosity μ_t and turbulent Reynolds number R_t are given as

$$\mu_t \equiv \rho\nu_t = \rho C_\mu f_\mu \mathcal{R}, \quad R_t \equiv \frac{\mathcal{R}}{\nu_l} = \frac{\rho}{\mu_l}\mathcal{R}$$

Now the transport equation in generalised coordinate system can be written as

$$\frac{\partial \hat{\boldsymbol{U}}}{\partial t} + \frac{\partial \hat{\boldsymbol{E}}}{\partial \xi} + \frac{\partial \hat{\boldsymbol{F}}}{\partial \eta} = \frac{\partial \hat{\boldsymbol{R}}}{\partial \xi} + \frac{\partial \hat{\boldsymbol{S}}}{\partial \eta} + \hat{\boldsymbol{H}}$$

$$\hat{\boldsymbol{U}} = \frac{1}{J}\begin{pmatrix} \rho k \\ \rho\mathcal{R} \end{pmatrix}, \qquad \hat{\boldsymbol{E}} = \frac{1}{J}\begin{pmatrix} \rho kU \\ \rho\mathcal{R}U \end{pmatrix}, \qquad \hat{\boldsymbol{F}} = \frac{1}{J}\begin{pmatrix} \rho kV \\ \rho\mathcal{R}V \end{pmatrix}$$

$$\hat{\boldsymbol{R}} = \frac{1}{J}\begin{pmatrix} (\mu_l + \frac{\mu_t}{\sigma_k})(\xi_x k_x + \xi_y k_y) \\ (\mu_l + \frac{\mu_t}{\sigma_R})(\xi_x \mathcal{R}_x + \xi_y \mathcal{R}_y) \end{pmatrix}, \qquad \hat{\boldsymbol{S}} = \frac{1}{J}\begin{pmatrix} (\mu_l + \frac{\mu_t}{\sigma_k})(\eta_x k_x + \eta_y k_y) \\ (\mu_l + \frac{\mu_t}{\sigma_\mathcal{R}})(\eta_x \mathcal{R}_x + \eta_y \mathcal{R}_y) \end{pmatrix}$$

$$\hat{\boldsymbol{H}} = \frac{1}{J}\begin{pmatrix} P_k - \frac{\rho k^2}{\mathcal{R}} \\ (2 - C_{R1})\frac{\mathcal{R}}{k}P_k - (2 - C_{R2})\rho k - \rho\frac{C_\mu}{\sigma_R}\{(\frac{\partial \mathcal{R}}{\partial x})^2 + (\frac{\partial \mathcal{R}}{\partial y})^2\} \end{pmatrix}$$

The the transport equations are non-dimensionalized making use of the following parameters

$$u^* = u/a_o, \qquad v^* = v/a_o, \qquad x^* = x/L, \qquad y^* = y/L$$

$$t^* = t/(L/a_o), \qquad \rho^* = \rho/\rho_o, \qquad \mu_i^* = \mu_i/\mu_o \quad (i = l, t)$$

$$k^* = \frac{k}{a_0^2}, \qquad \mathcal{R}^* = \frac{\mathcal{R}}{\nu_0}$$

In addition, Reynolds number and Mach number become as follows.

$$Re_0 = \frac{\rho_0 a_0 L}{\mu_0}, \qquad M_0 = \frac{a_0}{a_0} = 1$$

$$\frac{\partial(\rho k)}{\partial t}+\frac{\partial(\rho kU)}{\partial \xi}+\frac{\partial(\rho kV)}{\partial \eta}=\frac{\partial A}{\partial \xi}+\frac{\partial B}{\partial \eta}+(P_k-\frac{\rho k^2}{\mathcal{R}})$$

First, dimensionless conversion is done for A, B and P_k

$$A=(\mu_l^*\mu_0+\frac{\mu_t^*\mu_0}{\sigma_k})(\xi_x^*\frac{L}{L}k_x^*\frac{a_0^2}{L}+\xi_y^*\frac{L}{L}k_y^*\frac{a_0^2}{L})=(\mu_l^*+\frac{\mu_t^*}{\sigma_k})(\xi_x^*k_x^*+\xi_y^*k_y^*)\frac{\mu_0a_0^2}{L}=A^*\frac{\mu_0a_0^2}{L}$$

$$B=(\mu_l^*\mu_0+\frac{\mu_t^*\mu_0}{\sigma_k})(\eta_x^*\frac{L}{L}k_x^*\frac{a_0^2}{L}+\eta_y^*\frac{L}{L}k_y^*\frac{a_0^2}{L})=(\mu_l^*+\frac{\mu_t^*}{\sigma_k})(\eta_x^*k_x^*+\eta_y^*k_y^*)\frac{\mu_0a_0^2}{L}=B^*\frac{\mu_0a_0^2}{L}$$

$$\begin{aligned}P_k&=\mu_t^*\mu_0[2\{(u_x^*)^2+(v_y^*)^2\}\frac{a_0^2}{L^2}+(u_y^*+v_x^*)^2\frac{a_0^2}{L^2}-\frac{2}{3}(u_x^*+v_y^*)^2\frac{a_0^2}{L^2}]-\frac{2}{3}\rho^*\rho_0k^*a_0^2(u_x^*+v_y^*)\frac{a_0}{L}\\&=\frac{\mu_0a_0^2}{L^2}\mu_t^*[2\{(u_x^*)^2+(v_y^*)^2\}+(u_y^*+v_x^*)^2-\frac{2}{3}(u_x^*+v_y^*)^2]-\frac{2}{3}\rho^*k^*(u_x^*+v_y^*)\frac{\rho_0a_0^3}{L}\end{aligned}$$

$$P_k=\frac{\rho_0a_0^3}{L}\Big(\frac{\mu_0}{\rho_0a_0L}\mu_t^*[2\{(u_x^*)^2+(v_y^*)^2\}+(u_y^*+v_x^*)^2-\frac{2}{3}(u_x^*+v_y^*)^2]-\frac{2}{3}\rho^*k^*(u_x^*+v_y^*)\Big)$$

Introducing Reynolds number and Mach number as defined by the following expressions

$$Re_0=\frac{\rho_0a_0L}{\mu_0},\qquad M_0=1$$

we have

$$P_k=\frac{\rho_0a_0^3}{L}\Big((\frac{M_0}{Re_0})\mu_t^*[2\{(u_x^*)^2+(v_y^*)^2\}+(u_y^*+v_x^*)^2-\frac{2}{3}(u_x^*+v_y^*)^2]-\frac{2}{3}\rho^*k^*(u_x^*+v_y^*)\Big)=\frac{\rho_0a_0^3}{L}P_k^*$$

Now the whole equation takes the following dimensionless form

$$\begin{aligned}&\frac{\partial(\rho^*\rho_0k^*a_0^2)}{\partial(t^*L/a_0)}+\frac{\partial(\rho^*\rho_0k^*a_0^2U^*a_0)}{\partial(\xi^*L)}+\frac{\partial(\rho^*\rho_0k^*a_0^2V^*a_0)}{\partial(\eta^*L)}\\&\quad=\frac{\partial A^*}{\partial(\xi^*L)}\frac{\mu_0a_0^2}{L}+\frac{\partial B^*}{\partial(\eta^*L)}\frac{\mu_0a_0^2}{L}+(P_k^*\frac{\rho_0a_0^3}{L}-\frac{\rho^*\rho_0\epsilon^*(k^*a_0^2)^2}{(\mathcal{R}^*\nu_\prime)})\\&\frac{\partial(\rho^*k^*)}{\partial t^*}(\frac{\rho_0a_0^3}{L})+\frac{\partial(\rho^*k^*U^*)}{\partial\xi^*}(\frac{\rho_0a_0^3}{L})+\frac{\partial(\rho^*k^*V^*)}{\partial\eta^*}(\frac{\rho_0a_0^3}{L})\\&\quad=\frac{\partial A^*}{\partial\xi^*}(\frac{\mu_0a_0^2}{L^2})+\frac{\partial B^*}{\partial\eta^*}(\frac{\mu_0a_0^2}{L^2})+(P_k^*(\frac{\rho_0a_0^3}{L})-\frac{\rho^*(k^*)^2}{\mathcal{R}^*}(\frac{\rho_0a_0^4}{\mu_0}))\\&\frac{\partial(\rho^*k^*)}{\partial t^*}+\frac{\partial(\rho^*k^*U^*)}{\partial\xi^*}+\frac{\partial(\rho^*k^*V^*)}{\partial\eta^*}=\frac{\partial A^*}{\partial\xi^*}(\frac{\mu_0}{\rho_0a_0L})+\frac{\partial B^*}{\partial\eta^*}(\frac{\mu_0}{\rho_0a_0L})+(P_k^*-\frac{\rho^*(k^*)^2}{\mathcal{R}^*}(\frac{\rho_0a_0L}{\mu_0}))\\&\frac{\partial(\rho^*k^*)}{\partial t^*}+\frac{\partial(\rho^*k^*U^*)}{\partial\xi^*}+\frac{\partial(\rho^*k^*V^*)}{\partial\eta^*}=(\frac{\partial A^*}{\partial\xi^*}+\frac{\partial B^*}{\partial\eta^*})(\frac{M_0}{Re_0})+(P_k^*-\frac{\rho^*(k^*)^2}{\mathcal{R}^*}Re_0))\end{aligned}$$

$$\frac{\partial(\rho\mathcal{R})}{\partial t}+\frac{\partial(\rho\mathcal{R}U)}{\partial\xi}+\frac{\partial(\rho\mathcal{R}V)}{\partial\eta}$$

$$= \frac{\partial A}{\partial \xi} + \frac{\partial B}{\partial \eta} + ((2 - C_{R1})\frac{\mathcal{R}}{k}P_k - (2 - C_{R2})\rho k - \rho\frac{C_\mu}{\sigma_R}\{(\frac{\partial \mathcal{R}}{\partial x})^2 + (\frac{\partial \mathcal{R}}{\partial y})^2\})$$

The dimensionless conversion of A and B are done following the same approach as described earlier.

$$A = (\mu_l^*\mu_0 + \frac{\mu_t^*\mu_0}{\sigma_R})(\xi_x^*\frac{L}{L}\mathcal{R}_x^*\frac{\nu_0}{L} + \xi_y^*\frac{L}{L}\mathcal{R}_y^*\frac{\nu_0}{L}) = (\mu_l^* + \frac{\mu_t^*}{\sigma_R})(\xi_x^*\mathcal{R}_x^* + \xi_y^*\mathcal{R}_y^*)\frac{\mu_0\nu_0}{L} = A^*\frac{\mu_0\nu_0}{L}$$

$$B = (\mu_l^*\mu_0 + \frac{\mu_t^*\mu_0}{\sigma_R})(\eta_x^*\frac{L}{L}\mathcal{R}_x^*\frac{\nu_0}{L} + \eta_y^*\frac{L}{L}\mathcal{R}_y^*\frac{\nu_0}{L}) = (\mu_l^* + \frac{\mu_t^*}{\sigma_R})(\eta_x^*\mathcal{R}_x^* + \eta_y^*\mathcal{R}_y^*)\frac{\mu_0\nu_0}{L} = B^*\frac{\mu_0\nu_0}{L}$$

Using the above expression

$$H = (2 - C_{R1})\frac{\mathcal{R}}{k}P_k - (2 - C_{R2})\rho k - \rho\frac{C_\mu}{\sigma_R}\{(\frac{\partial \mathcal{R}}{\partial x})^2 + (\frac{\partial \mathcal{R}}{\partial y})^2\}$$

$$= (2-C_{R1})\frac{(\mathcal{R}^*\nu_0)}{(k^*a_0^2)}(\frac{\rho_0 a_0^3}{L})P_k^* - (2-C_{R2})\rho^*\rho_0 k^* a_0^2 - \rho^*\rho_0\frac{C_\mu}{\sigma_R}\{(\frac{\partial(\mathcal{R}^*\nu_0)}{\partial(x^*L)})^2 + (\frac{\partial(\mathcal{R}^*\nu_0)}{\partial(y^*L)})^2\}$$

$$= (2 - C_{R1})\frac{\mathcal{R}^*}{k^*}P_k^*(\frac{\rho_0\nu_0 a_0}{L}) - (2 - C_{R2})\rho^* k^*(\rho_0 a_0^2) - \rho^*\frac{C_\mu}{\sigma_R}\{(\frac{\partial \mathcal{R}^*}{\partial x^*})^2 + (\frac{\partial \mathcal{R}^*}{\partial y^*})^2\}(\frac{\rho_0\nu_0^2}{L^2})$$

$$= (\frac{\rho_0\nu_0 a_0}{L})\Big((2-C_{R1})\frac{\mathcal{R}^*}{k^*}P_k^* - (2-C_{R2})\rho^* k^*(\frac{La_0}{\nu_0}) - \rho^*\frac{C_\mu}{\sigma_R}\{(\frac{\partial \mathcal{R}^*}{\partial x^*})^2 + (\frac{\partial \mathcal{R}^*}{\partial y^*})^2\}(\frac{\nu_0}{La_0})\Big)$$

$$H = (\frac{\rho_0\nu_0 a_0}{L})\Big((2-C_{R1})\frac{\mathcal{R}^*}{k^*}P_k^* - (2-C_{R2})\rho^* k^* Re_0 - \rho^*\frac{C_\mu}{\sigma_R}\{(\frac{\partial \mathcal{R}^*}{\partial x^*})^2 + (\frac{\partial \mathcal{R}^*}{\partial y^*})^2\}\frac{1}{Re_0}\Big)$$

$$H = (\frac{\rho_0\nu_0 a_0}{L})H^*$$

Using the relationship of A^*, B^*, H^*, the whole equation in non-dimensionalized form can be written as

$$\frac{\partial(\rho^*\rho_0\mathcal{R}^*\nu_0)}{\partial(t^*(L/a_0))} + \frac{\partial(\rho^*\rho_0\mathcal{R}^*\nu_0 U^* a_0)}{\partial(\xi^* L)} + \frac{\partial(\rho^*\rho_0\mathcal{R}^*\nu_0 V^* a_0)}{\partial(\eta^* L)}$$
$$= \frac{\partial A^*}{\partial(\xi^* L)}(\frac{\mu_0\nu_0}{L}) + \frac{\partial B^*}{\partial(\eta^* L)}(\frac{\mu_0\nu_0}{L}) + (\frac{\rho_0\nu_0 a_0}{L})H^*$$

$$\frac{\partial(\rho^*\mathcal{R}^*)}{\partial t^*}(\frac{\rho_0\nu_0 a_0}{L}) + \frac{\partial(\rho^*\mathcal{R}^* U^*)}{\partial \xi^*}(\frac{\rho_0\nu_0 a_0}{L}) + \frac{\partial(\rho^*\mathcal{R}^* V^*)}{\partial \eta^*}(\frac{\rho_0\nu_0 a_0}{L})$$
$$= \frac{\partial A^*}{\partial \xi^*}(\frac{\mu_0\nu_0}{L^2}) + \frac{\partial B^*}{\partial \eta^*}(\frac{\mu_0\nu_0}{L^2}) + (\frac{\rho_0\nu_0 a_0}{L})H^*$$

$$\frac{\partial(\rho^*\mathcal{R}^*)}{\partial t^*} + \frac{\partial(\rho^*\mathcal{R}^* U^*)}{\partial \xi^*} + \frac{\partial(\rho^*\mathcal{R}^* V^*)}{\partial \eta^*} = \frac{\partial A^*}{\partial \xi^*}(\frac{\mu_0}{\rho_0 a_0 L}) + \frac{\partial B^*}{\partial \eta^*}(\frac{\mu_0}{\rho_0 a_0 L}) + H^*$$

Again, introducing the Reynolds number and Mach number, where

$$Re_0 = \frac{\rho_0 a_0 L}{\mu_0}, \qquad M_0 = 1$$

the equation takes the form

$$\frac{\partial(\rho^*\mathcal{R}^*)}{\partial t^*}+\frac{\partial(\rho^*\mathcal{R}^*U^*)}{\partial \xi^*}+\frac{\partial(\rho^*\mathcal{R}^*V^*)}{\partial \eta^*}=(\frac{M_0}{Re_0})(\frac{\partial A^*}{\partial \xi^*}+\frac{\partial B^*}{\partial \eta^*})+H^*$$

The non-dimensionalized turbulent coefficient of viscosity and formula of turbulent Reynolds number take the following form

$$\mu_t^*=\frac{\mu_t}{\mu_0}=\frac{\rho C_\mu f_\mu \mathcal{R}}{\mu_0}=\frac{\rho^*\rho_0 C_\mu f_\mu \mathcal{R}^*\nu_\prime}{\mu_0}=\rho^* C_\mu f_\mu \mathcal{R}^*$$

$$R_t=\frac{\rho}{\mu_l}\mathcal{R}=\frac{\rho^*\rho_0}{\mu^*\mu_0}\mathcal{R}^*\nu_0=\frac{\rho^*}{{\mu_l}^*}\mathcal{R}^*$$

The symbol $*$ in the above expressions is used for dimensionless quantity. It is omitted from the following expressions.

$$\frac{\partial \hat{\boldsymbol{U}}}{\partial t}+\frac{\partial \hat{\boldsymbol{E}}}{\partial \xi}+\frac{\partial \hat{\boldsymbol{F}}}{\partial \eta}=\frac{1}{Re_0}(\frac{\partial \hat{\boldsymbol{R}}}{\partial \xi}+\frac{\partial \hat{\boldsymbol{S}}}{\partial \eta})+\hat{\boldsymbol{H}}$$

$$\hat{\boldsymbol{U}}=\frac{1}{J}\begin{pmatrix}\rho k\\ \rho\mathcal{R}\end{pmatrix},\qquad \hat{\boldsymbol{E}}=\frac{1}{J}\begin{pmatrix}\rho kU\\ \rho\mathcal{R}U\end{pmatrix},\qquad \hat{\boldsymbol{F}}=\frac{1}{J}\begin{pmatrix}\rho kV\\ \rho\mathcal{R}V\end{pmatrix}$$

$$\hat{\boldsymbol{R}}=\frac{1}{J}\begin{pmatrix}(\mu_l+\frac{\mu_t}{\sigma_k})(\xi_x k_x+\xi_y k_y)\\ (\mu_l+\frac{\mu_t}{\sigma_R})(\xi_x\mathcal{R}_x+\xi_y\mathcal{R}_y)\end{pmatrix},\quad \hat{\boldsymbol{S}}=\frac{1}{J}\begin{pmatrix}(\mu_l+\frac{\mu_t}{\sigma_k})(\eta_x k_x+\eta_y k_y)\\ (\mu_l+\frac{\mu_t}{\sigma_R})(\eta_x\mathcal{R}_x+\eta_y\mathcal{R}_y)\end{pmatrix}$$

$$\hat{\boldsymbol{H}}=\frac{1}{J}\begin{pmatrix}P_k-\frac{\rho k^2}{\mathcal{R}}Re_0\\ (2-C_{R1})\frac{\mathcal{R}}{k}P_k-(2-C_{R2})\rho k Re_0-\rho\frac{C_\mu}{\sigma_R Re_0}\{(\frac{\partial\mathcal{R}}{\partial x})^2+(\frac{\partial\mathcal{R}}{\partial y})^2\}\end{pmatrix}$$

$$P_k=(\frac{M_0}{Re_0})\mu_t[2(u_x^2+v_y^2)+(u_y+v_x)^2-\frac{2}{3}(u_x+v_y)^2]-\frac{2}{3}\rho k(u_x+v_y)$$

$$\mu_t=\rho C_\mu f_\mu\mathcal{R},\qquad R_t=\frac{\rho}{\mu_l}\mathcal{R}$$

Therefore, the non-dimensionalized unsteady compressible Navier-Stokes equations coupled with turbulence kinetic energy and eddy viscosity equations of $k-\mathcal{R}$ model can be written as

$$\frac{\partial \hat{\boldsymbol{U}}}{\partial t}+\frac{\partial \hat{\boldsymbol{E}}}{\partial \xi}+\frac{\partial \hat{\boldsymbol{F}}}{\partial \eta}=\frac{1}{Re_0}(\frac{\partial \hat{\boldsymbol{R}}}{\partial \xi}+\frac{\partial \hat{\boldsymbol{S}}}{\partial \eta})+\hat{\boldsymbol{H}}$$

where

$$\hat{\boldsymbol{U}} = \frac{1}{J}\begin{pmatrix} \rho \\ \rho u \\ \rho v \\ E_t \\ \rho k \\ \rho \mathcal{R} \end{pmatrix}, \qquad \hat{\boldsymbol{E}} = \frac{1}{J}\begin{pmatrix} \rho U \\ \rho u U + \xi_x p \\ \rho v U + \xi_y p \\ U(E_t + p) \\ \rho k U \\ \rho \mathcal{R} U \end{pmatrix}, \qquad \hat{\boldsymbol{F}} = \frac{1}{J}\begin{pmatrix} \rho V \\ \rho u V + \eta_x p \\ \rho v V + \eta_y p \\ V(E_t + p) \\ \rho k V \\ \rho \mathcal{R} V \end{pmatrix}$$

$$\hat{\boldsymbol{R}} = \frac{1}{J}\begin{pmatrix} 0 \\ \xi_x \tau_{xx} + \xi_y \tau_{yx} \\ \xi_x \tau_{xy} + \xi_y \tau_{yy} \\ \xi_x \alpha + \xi_y \beta \\ (\mu_l + \frac{\mu_t}{\sigma_k})(\xi_x k_x + \xi_y k_y) \\ (\mu_l + \frac{\mu_t}{\sigma_R})(\xi_x \mathcal{R}_x + \xi_y \mathcal{R}_y) \end{pmatrix}, \quad \hat{\boldsymbol{S}} = \frac{1}{J}\begin{pmatrix} 0 \\ \eta_x \tau_{xx} + \eta_y \tau_{yx} \\ \eta_x \tau_{xy} + \eta_y \tau_{yy} \\ \eta_x \alpha + \eta_y \beta \\ (\mu_l + \frac{\mu_t}{\sigma_k})(\eta_x k_x + \eta_y k_y) \\ (\mu_l + \frac{\mu_t}{\sigma_R})(\eta_x \mathcal{R}_x + \eta_y \mathcal{R}_y) \end{pmatrix}$$

$$\hat{\boldsymbol{H}} = \frac{1}{J}\begin{pmatrix} 0 \\ 0 \\ 0 \\ 0 \\ P_k - \frac{\rho k^2}{\mathcal{R}} Re_0 \\ (2 - C_{R1})\frac{\mathcal{R}}{k} P_k - (2 - C_{R2})\rho k Re_0 - \rho \frac{C_\mu}{\sigma_R Re_0}\{(\frac{\partial \mathcal{R}}{\partial x})^2 + (\frac{\partial \mathcal{R}}{\partial y})^2\} \end{pmatrix}$$

$$\alpha = \tau_{xx} u + \tau_{xy} v + \frac{\mu}{(\gamma - 1) Pr}\frac{\partial T}{\partial x}, \quad \beta = \tau_{yx} u + \tau_{yy} v + \frac{\mu}{(\gamma - 1) Pr}\frac{\partial T}{\partial y}$$

$$U = \xi_x u + \xi_y v, \quad V = \eta_x u + \eta_y v$$

The components of the stress tensors are

$$\tau_{xx} = \frac{2}{3}\mu(2\frac{\partial u}{\partial x} - \frac{\partial v}{\partial y}) - \frac{2}{3}\rho k, \quad \tau_{xy} = \mu(\frac{\partial u}{\partial y} + \frac{\partial v}{\partial x}), \quad \tau_{yy} = \frac{2}{3}\mu(2\frac{\partial v}{\partial y} - \frac{\partial u}{\partial x}) - \frac{2}{3}\rho k$$

$$\mu = \mu_l + \mu_t$$

$$\frac{\mu}{Pr} = \frac{\mu_l}{Pr_l} + \frac{\mu_t}{Pr_t}$$

$$P_k = (\frac{M_0}{Re_0})\mu_t[2(u_x^2 + v_y^2) + (u_y + v_x)^2 - \frac{2}{3}(u_x + v_y)^2] - \frac{2}{3}\rho k(u_x + v_y)$$

The limiter function to suppress the instability is

$$P_k = \min[P_k, C_2 C_b \rho \epsilon R_e / C_1]$$

$$C_2 = 1.92 \times [1 - 0.3\exp(-R_t^2)], \quad C_b = (\text{limiting Parameter}) > 1, \quad C_1 = 1.44$$

$$\mu_t = \rho C_\mu f_\mu \mathcal{R}, \qquad f_\mu = \frac{\tanh(\alpha' R_t)}{\tanh(\beta' R_t)}, \qquad R_t = \frac{\rho}{\mu_l}\mathcal{R}$$

Constants of the model are as follows

$$\sigma_k = 1.0, \quad \sigma_R = 1.080, \quad C_{R1} = 1.44, \quad C_{R2} = 1.92, \quad C_\mu = 0.09$$

$$\alpha' = 0.005, \quad \beta' = \frac{C_\mu^{3/4}}{k}$$

$$k^2 = \sigma_R \sqrt{C_\mu}(C_{R2} - C_{R1})$$

4.3.2.2 Jacobian matrix (by Pulliam and Chausse)

Pulliam and Chaussee [83] introduced a diagonalized form of Jacobian matrix. When an implicit algorithm is applied to a system of partial differential equations, one obtains block-matrix vector equations that are complicated and time consuming to solve. Here they proposed a method for uncoupling the solution process, through a diagonalization of the block-matrix structure. The resulting algorithm reduces computational costs by requiring only scalar tridiagonal or pentadiagonal systems instead of block tridiagonal systems.

According to Pulliam and Chausse, the Jacobian matrix for $\hat{\boldsymbol{A}} = \partial\hat{\boldsymbol{E}}/\partial\hat{\boldsymbol{Q}}$ and $\hat{\boldsymbol{B}} = \partial\hat{\boldsymbol{F}}/\partial\hat{\boldsymbol{Q}}$ are

$$\hat{\boldsymbol{A}}\text{or}\hat{\boldsymbol{B}} = \begin{pmatrix} 0 & k_x & k_y & 0 & 0 & 0 \\ -u\theta + k_x\phi^2 & \theta - (G-1)k_x u & k_y u - G k_x v & k_x G & 0 & 0 \\ -v\theta + k_y\phi^2 & k_x v - G k_y u & \theta - (G-1)k_y v & k_y G & 0 & 0 \\ \theta[2\phi^2 - \gamma\frac{E_t}{\rho}] & k_x[\gamma\frac{E_t}{\rho} - \phi^2] - Gu\theta & k_y[\gamma\frac{E_t}{\rho} - \phi^2] - Gv\theta & \gamma\theta & 0 & 0 \\ -k\theta & k_x k & k_y k & 0 & \theta & 0 \\ -\mathcal{R}\theta & k_x\mathcal{R} & k_y\mathcal{R} & 0 & 0 & \theta \end{pmatrix}$$

where

$$\theta = k_x u + k_y v, \quad \phi^2 = \frac{1}{2}G(u^2 + v^2), \quad G = \gamma - 1$$

with $k = \xi$ for $\hat{\boldsymbol{A}}$ and $k = \eta$ for $\hat{\boldsymbol{B}}$.

In order to make the expressions of eigen value and the eigen vector simple, the following variables are introduced

$$\alpha = \frac{\rho}{\sqrt{2}a}, \qquad \beta = \frac{1}{\sqrt{2}\rho a}, \qquad \tilde{k}_x = \frac{k_x}{\sqrt{k_x^2 + k_y^2}}, \qquad \tilde{k}_y = \frac{k_y}{\sqrt{k_x^2 + k_y^2}}$$

$$\tilde{\theta} = \tilde{k}_x u + \tilde{k}_y v \quad (\boldsymbol{A} : k = \xi, \boldsymbol{B} : k = \eta)$$

The similarity transformations to diagonalize the Jacobian matrices $\hat{\boldsymbol{A}}$ and $\hat{\boldsymbol{B}}$ are

$$\boldsymbol{A} = \boldsymbol{R}_\xi \hat{\boldsymbol{\Lambda}}_\xi \boldsymbol{R}_\xi^{-1}, \qquad \boldsymbol{B} = \boldsymbol{R}_\eta \hat{\boldsymbol{\Lambda}}_\eta \boldsymbol{R}_\eta^{-1}$$

where

$$\hat{\boldsymbol{\Lambda}}_\xi = D[U, U, U + a\sqrt{\xi_x^2 + \xi_y^2}, U - a\sqrt{\xi_x^2 + \xi_y^2}, U, U]$$

$$= \begin{pmatrix} U & 0 & 0 & 0 & 0 & 0 \\ 0 & U & 0 & 0 & 0 & 0 \\ 0 & 0 & U + a\sqrt{\xi_x^2 + \xi_y^2} & 0 & 0 & 0 \\ 0 & 0 & 0 & U - a\sqrt{\xi_x^2 + \xi_y^2} & 0 & 0 \\ 0 & 0 & 0 & 0 & U & 0 \\ 0 & 0 & 0 & 0 & 0 & U \end{pmatrix}$$

,

$$\hat{\boldsymbol{\Lambda}}_\eta = D[V, V, V + a\sqrt{\eta_x^2 + \eta_y^2}, V - a\sqrt{\eta_x^2 + \eta_y^2}, V, V]$$

$$= \begin{pmatrix} V & 0 & 0 & 0 & 0 & 0 \\ 0 & V & 0 & 0 & 0 & 0 \\ 0 & 0 & V + a\sqrt{\eta_x^2 + \eta_y^2} & 0 & 0 & 0 \\ 0 & 0 & 0 & V - a\sqrt{\eta_x^2 + \eta_y^2} & 0 & 0 \\ 0 & 0 & 0 & 0 & V & 0 \\ 0 & 0 & 0 & 0 & 0 & V \end{pmatrix}$$

with

$$a^2 = \gamma \frac{p}{\rho}$$

and

$$p = (\gamma - 1)\rho e = (\gamma - 1)\{E_t - \frac{1}{2}\rho(u^2 + v^2) - \rho k\}$$

Again the matrices for $\boldsymbol{R}_k$ and $\boldsymbol{R}_k^{-1} = \boldsymbol{L}_k$ take the following form

$$\boldsymbol{R}_k = \begin{pmatrix} 1 & 0 & \alpha & \alpha & 0 & 0 \\ u & \tilde{k}_y \rho & \alpha(u + \tilde{k}_x a) & \alpha(u - \tilde{k}_x a) & 0 & 0 \\ v & -\tilde{k}_x \rho & \alpha(v + \tilde{k}_y a) & \alpha(v - \tilde{k}_y a) & 0 & 0 \\ \frac{\phi^2}{G} & \rho(\tilde{k}_y u - \tilde{k}_x v) & \alpha(\frac{\phi^2 + a^2}{G} + a\tilde{\theta}) & \alpha(\frac{\phi^2 + a^2}{G} - a\tilde{\theta}) & 0 & 0 \\ k & 0 & k\alpha & k\alpha & \rho & 0 \\ \mathcal{R} & 0 & \mathcal{R}\alpha & \mathcal{R}\alpha & 0 & \rho \end{pmatrix}$$

,

$$\boldsymbol{L}_k = \begin{pmatrix} 1-\phi^2 a^{-2} & Ga^{-2}u & Ga^{-2}v & -Ga^{-2} & 0 & 0 \\ -\rho^{-1}(\tilde{k}_y u - \tilde{k}_x v) & \tilde{k}_y \rho^{-1} & -\tilde{k}_x \rho^{-1} & 0 & 0 & 0 \\ \beta(\phi^2 - a\tilde{\theta}) & \beta(\tilde{k}_x a - Gu) & \beta(\tilde{k}_y a - Gv) & \beta G & 0 & 0 \\ \beta(\phi^2 + a\tilde{\theta}) & -\beta(\tilde{k}_x a + Gu) & -\beta(k_y a + Gv) & \beta G & 0 & 0 \\ -\frac{k}{\rho} & 0 & 0 & 0 & 1/\rho & 0 \\ -\frac{\mathcal{R}}{\rho} & 0 & 0 & 0 & 0 & 1/\rho \end{pmatrix}$$

The initial and boundary condition of this model are given below

Solid wall

$$k = \mathcal{R} = 0$$

Axis of symmetry

$$\frac{\partial k}{\partial y} = 0, \quad \frac{\partial \mathcal{R}}{\partial y} = 0$$

Boundary and initial condition

$$k = 1.0 \times 10^{-6}, \quad \mathcal{R}_0 = \mathcal{O}(10^{-5}) \ll 1$$

4.4 Time splitting method

The primary concern for the numerical analysis in obtaining computational solutions is accuracy. The next concern is efficiency. The aim of splitting methods is to split the solution of a large and complicated system into a less few complicated systems [85]. The problem of solving large and complicated system may arise when one apply fully implicit methods to multi-dimentional problems. In numerical models, the time step needed to stably integrate the high-frequency modes are sometimes smaller than the time step needed for stable and accurate integration of the low-frequency modes. A usual method to improve computational efficiency is to employ explicit numerical schemes that integrate the high-frequency modes using a small time step while integrating the lower-frequency modes using a larger time step [86]. These methods are often called splitting methods, and several different splitting methodologies based on explicit integration schemes exist. The time splitting method employed in the present numerical investigation is described below.

Here we divided a multidimensional equation into the equation of one dimension, applying one dimensional difference method and calculating the solution of original equation as a superposition of individual solutions. We have

$$\boldsymbol{U}_t + \boldsymbol{E}_x + \boldsymbol{F}_y = 0 \tag{4.4}$$

One dimensional equations in x and y directions are

$$\boldsymbol{U}_t + \boldsymbol{E}_x = 0 \tag{4.5}$$

$$\boldsymbol{U}_t + \boldsymbol{F}_y = 0 \tag{4.6}$$

The solutions are

$$\boldsymbol{U}^{n+1} = L_x(\Delta t)\boldsymbol{U}^n \tag{4.7}$$

and

$$L_y(\Delta t)L_x(\Delta t)\boldsymbol{U}^n \equiv L_y(\Delta t)\{L_x(\Delta t)\boldsymbol{U}^n\} \tag{4.8}$$

Secondary precision can be obtained as follows

$$S_2 = L_x\left(\frac{1}{2}\Delta t\right)L_y(\Delta t)L_x\left(\frac{1}{2}\Delta t\right) \tag{4.9}$$

With time splitting, stable condition of each operator becomes stable condition of entire scheme S. Introducing $m = \Delta x/\Delta y \gg 1$ we have

$$S_4 = L_x\left(\frac{1}{2}\Delta t\right)L_y\left(\frac{\Delta t}{m}\right)\cdots L_y\left(\frac{\Delta t}{m}\right)L_x\left(\frac{1}{2}\Delta t\right) \tag{4.10}$$

and

$$\boldsymbol{U}^{n+1} = \left\{L_y\left(\frac{\Delta t}{2m}\right)\right\}^m L_x(\Delta t)\left\{L_y\left(\frac{\Delta t}{2m}\right)\right\}^m \boldsymbol{U}^n \tag{4.11}$$

Here $m = 1$ is used in the present computation.

The number of iterations or time steps to perform in a given run is defined in terms of cycles and iterations per cycle. An iteration advances the solution one time step. A cycle consists of a solution pass over all the zones. The first requirement of any method is that its numerical domain includes the actual physical domain. This requirement determines a condition necessary for convergence, the Courant-Friedrich-Lowy (CFL) condition, which relates the maximum allowable time step size to mesh spacing and local flow properties [84]. For steady flow problems, the time step is represented by the CFL number. For unsteady flow problems, the time step in seconds is specified directly.

$$\Delta t = \frac{1}{2}\mathrm{CFL}\min\left(\frac{\Delta x_{i+1/2}}{|u_{i+1/2} - a_{i+1/2}|}, \frac{\Delta x_{i+1/2}}{|u_{i+1/2} + a_{i+1/2}|}\right) \tag{4.12}$$

and

$$\Delta t = \mathrm{CFL}\min\left(\frac{\Delta x_{i+1/2}}{|u_{i+1/2} - a_{i+1/2}|}, \frac{\Delta x_{i+1/2}}{|u_{i+1/2} + a_{i+1/2}|}\right) \tag{4.13}$$

CHAPTER 5
EXPERIMENTAL SETUP AND PROCEDURE

5.1 Supersonic flow facility

Experiments were conducted using a supersonic indraft wind tunnel [70] where dry air at atmospheric pressure was drawn into a vacuum tank, was used in the present experiment. The test facility consists of supersonic wind tunnel, air storing tank, the test section and the vacuum tank as shown in Fig.5.1. Test section is a height of 60 mm, a length of 553 mm and a width of 38 mm (Fig.5.2). In order to visualize the flow clearly and take Schlieren photograph, two side walls of the test section was made by a transparent medium. A converging/diverging nozzle that has been designed for a Mach number of $M = 1.83$, the inlet Mach number of the test section. Figure 5.3 shows the detail of the converging/diverging nozzle with a cavity. The reservoir pressure and temperature are the same as computational ones.

5.2 Pressure measurement system

In order to measure the variations of static pressure, the pressure transducer model EPIH-112-15P-/Z0 of Entran was connected to a personal computer through a DC amplifier (AM32 of Unipulse). According to the manufacturer specifications, the resonant frequency of the sensor is 400 kHz. The SNR (signal to noise ratio) of the pressure transducer is estimated as 30 dB. For conditioning the signals, cables were shielded and sensor was properly grounded. The reservoir pressure and temperature are the same as computational ones.

5.3 Schlieren optical system

Due to the high density gradients associated with supersonic flow and resulting shock activity, pictures of the shock structure were taken using the schlieren photographic technique. A diagram of the particular schlieren setup used in this study can be found below in Fig. 5.4. The arrangement of optical system, arrangement of the digital camera are shown in Fig.5.4. The still picture and animated picture were taken by the digital camera (Lens exchange, single-lens reflex type digital camera of Fuji Pic. Ltd.) and the PHOTRON high-speed video camera of model FASTCAM-ultra-UV3/IR3, respectively.

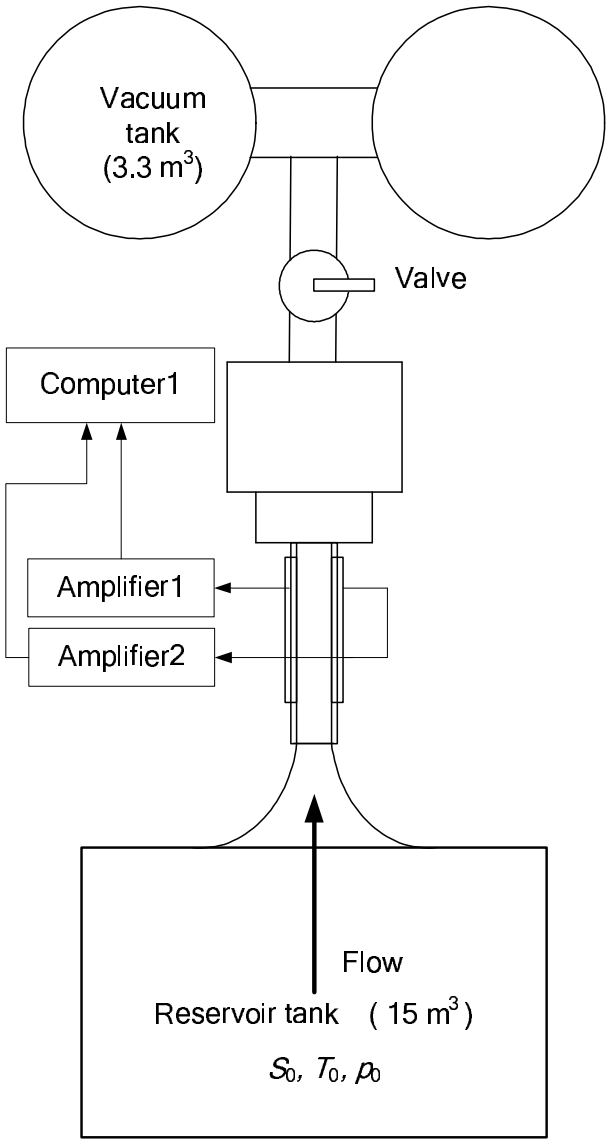

Figure 5.1: Schematic view of experimental apparatus.

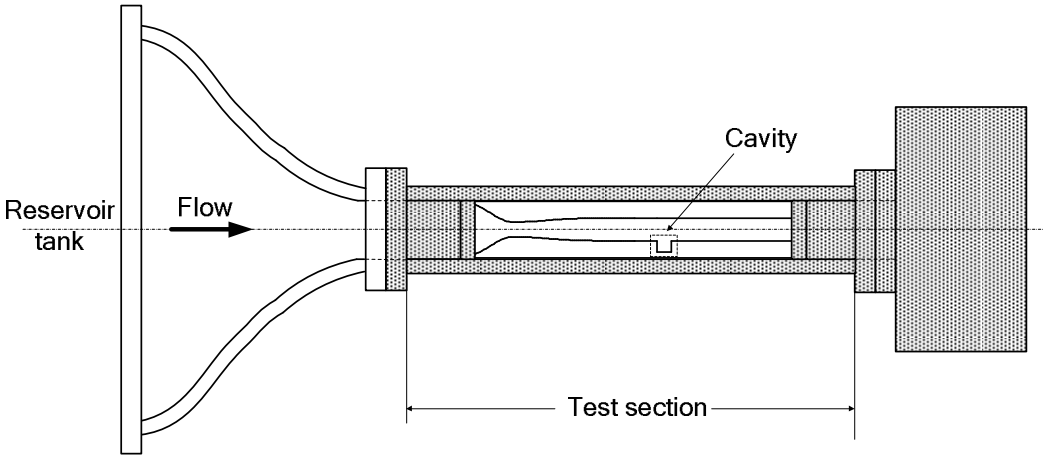

Figure 5.2: Test section.

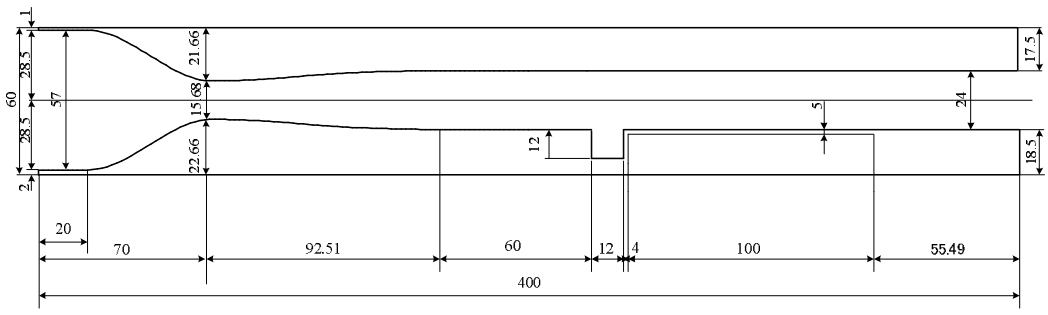

Figure 5.3: Converging/diverging nozzle with a cavity in detail.

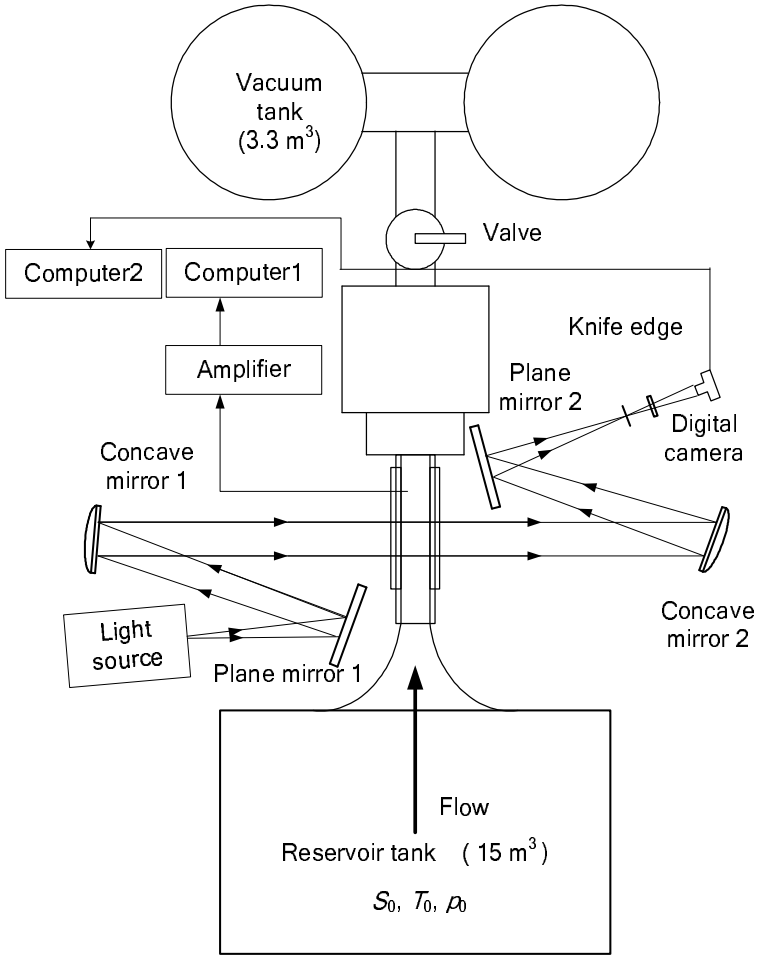

Figure 5.4: Schematic view of experimental apparatus showing the arrangement of Schlieren photography.

CHAPTER 6
EFFECT OF LEADING EDGE PLATE AND SUB-CAVITY ON CAVITY-INDUCED PRESSURE OSCILLATIONS

6.1 Conditions of numerical simulations

Figure 6.1 shows the grids and computational domain of the cavity. The height of the main flow section above the cavity is 24 mm. The origin O in $x-y$ coordinate is located at the leading edge of the cavity.

A cavity with aspect ratio $L/D = 1.0$ has been adopted for the present computational study. According to Sakamoto et al. [87] the structure of flowfield for a cavity with length to depth ratio $L/D = 1.0$ is two dimensional. Therefore, two dimensional simulations of square cavity with length to depth ratio $L/D = 1.0$ were performed to evaluate the proposed devices as suppressors of cavity-induced pressure oscillations. The depth D and the length L of the cavity are the same and equal to 12 mm. The ratios of the length l of the flat plate to the depth of the cavity D are $l/D = 0$, -0.125, -0.1875 and -0.25, and the ratios of the lip thickness t to the depth of the baseline cavity D are $t/D = 0.05$, 0.10, 0.15, 0.20, 0.25 and 0.30. The ratios of the depth of sub-cavity d to the depth of the baseline cavity D are $d/D = 0.25$, 0.30, 0.35, 0.45, 0.65, 0.70 and 0.75 in the simulations. Since the static pressure distributions are the highest along the wall of aft bulkhead [23] in comparison with that of other walls (e.g., forward bulkhead and floor) in the cavity, location of pressure measurement has been selected at $(x, y) = (L, -0.25D)$ in the present simulation. S1 in this figure denotes the measuring position of static pressure. The number of grids is 200×80 in the region of the nozzle and 50×60 in the cavity.

In the present study, dry air is used as a working gas and assumed to be thermally and calorically perfect. Pressure p_0 in the reservoir is 101.3 kPa. The inlet Mach number M_{inlet} at the entrance of the cavity is 1.83. The Reynolds number is 2.1×10^5. On the solid walls, the no-slip conditions and no heat transfers were applied as the boundary conditions. Fixed conditions were set for the inflow boundary. Zero order extrapolation was used at the outflow boundary.

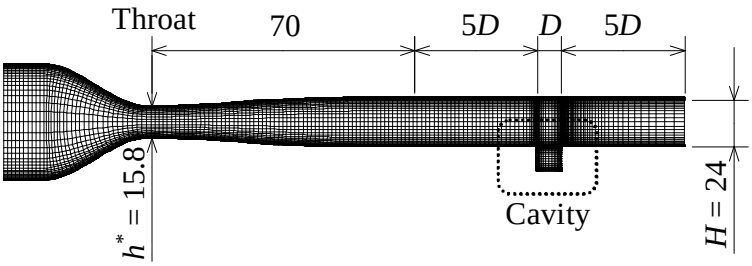

(a) Computational grids (Unit : mm)

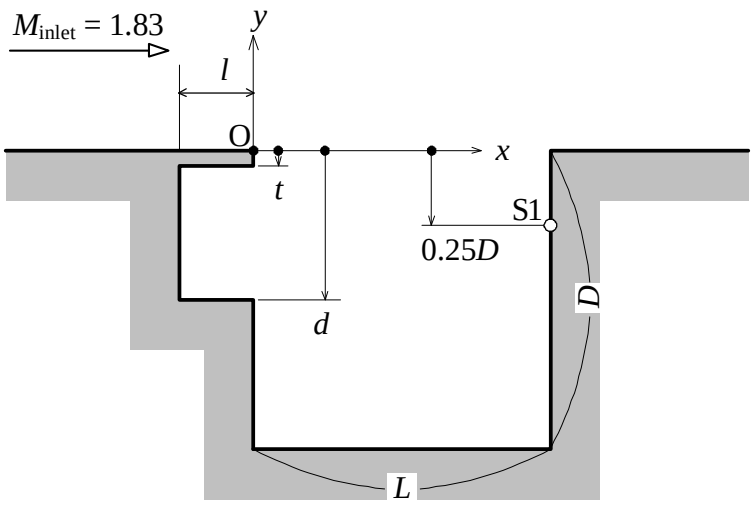

(b) Details of cavity configuration

Figure 6.1: Computational domain

6.2 Analysis of simulation data

6.2.1 Cavity without control

Figure 6.2(a) shows the time history of static pressure at the position S1 inside the cavity for case with a cavity (length to depth ratio = 1) without control. There exist large amplitudes of oscillations at the position S1 as shown in Fig.6.2(a). Distribution of power spectrum density obtained from the static pressure history is shown in Fig.6.2(b). There is a dominant frequency at 17.5 kHz in case of cavity without control.

Figure 6.3 shows contour maps of density during one period of flowfield oscillation for the cavity without control. Here, f represents the dominant frequency, which is equal to 17.5 kHz (see Fig.6.2(b)). It was observed that a compression wave (CW) from the trailing edge of the cavity moves upstream as time proceeds. The compression wave in Fig.6.3(i) converts into an upstream traveling compression waves (CW' shown in Fig.6.3(a)). The upstream compression waves impinge on the cavity leading edge and disturb the shear layer (Fig.6.3 (g)). This disturbance regenerates instability waves in the shear layer. While the shear layer reattaches at the rear wall of the cavity, generation of compression waves (CW) occurs due to the impingement of instability waves on the wall as shown in Fig.6.3(a). These compression waves propagate upstream within the cavity and further disturb the shear layer. The shear layer is continuously modified due to these subsequent disturbances and finally resonance occurs when frequency and the phase of the acoustic waves match with those of the shear layer instability waves.

Figure 6.4 shows a sequence of representative instantaneous streamline contours resulting from the cavity without control. There is a very good inclination to develop a single, large vortex in the cavity accompanied by some small vortices in the corner [2]. Furthermore, the shedding of vortices from the leading edge corner [31, 88] is also observed in the cavity without control such that the vortices at the leading edge corner (Figs. 6.4(a) and 6.4(b)) are shedding on the subsequent events (Figs. 6.4(c) through 6.4(f)) increases the instability of shear layer. Figures 6.4(g) through 6.4(i) show the development of another small vortex at the leading edge corner of the cavity.

6.2.2 Effect of leading edge plate on flowfield oscillations

Observations were made with the introduction of the leading edge flat plate. Figure 6.5 show the time histories of the static pressure at the position S1 inside the cavity with control. A substantial reduction of the amplitudes was obtained when

a flat plate is introduced in the cavity (when l/D = -0.25, t/D = 0.05 and d/D = 1.0) as in Fig.6.5(a). Distribution of power spectrum density at the same position obtained from the static pressure histories is shown in Fig.6.5(b). There is no peak frequency for case with control as shown in the Fig.6.5(b) (when l/D = -0.25, t/D = 0.05 and d/D = 1.0), whereas there is a dominant frequency at 17.5 kHz in case of cavity without control (Fig.6.2(b)). It is widely believed that the feedback loop is the reason of cavity resonance that leads to increase high pressure oscillations in the cavity. Therefore, the formation of feedback loops and consequently the occurrence of resonance are considered to be the reason of intense pressure oscillations observed in the cavity. The significant reductions of cavity pressure oscillations that obtained by the present control device (Fig.6.5) can be explained from the fact that the upstream compression waves that impinges on the leading edge wall below the flat plate cannot disturb the shear layer immediately after the reflection. The reflected compression waves which are now below the flat plate and traveling toward downstream direction, gradually become weaker as they travel and are to be dissipated according to Tam et al. [58]. Furthermore, Quinn [88] and Franke and Carr [31] showed that vortices were shed as the upstream traveling compression waves reflected from the trailing edge wall of the cavity. Therefore, interaction of the reflected compression waves with the shear layer and the shedding of vortices immediately after the reflection will not be possible in the present investigation due to the obstruction imposed by the flat plate. Furthermore, after the reflection, the gradually dissipating compression waves, while propagating toward the downstream direction, cannot excite the shear layer strongly enough to form instability waves and the formation of feedback loop is discouraged.

6.2.3 Effect of length of leading edge plate on flowfield oscillations

Figure 6.6 shows amplitudes of oscillations with different lengths of the plate at the position S1 in the cavity. The amplitude of the oscillations reduces substantially with an increase of the length of flat plate. Distributions of power spectrum density (see Fig.6.7) shows that there are some peak frequencies when the length of the plate was relatively small (at l/D = -0.125 and l/D = -0.1875) and there is no peak frequency at a relatively large length of the plate (at l/D = -0.25). The reason of these results are due to the fact that the reflected compression waves which are below the flat plate have to travel more to the downstream direction in order to interact with the shear layer and become much weaker gradually with an increase of the length of the plate. Consequently, those weaker compression waves can not disturb the shear layer strongly enough to regenerate the instability waves. The

best performance was obtained in case of l/D = -0.25 as shown in Figs.6.6(a) and 6.7(a).

6.2.4 Effect of thickness of leading edge plate on flowfield oscillations

The effect of the plate thickness t on the flow field oscillations are shown in Fig.6.8. It shows the time histories of the static pressure at the position S1 on the trailing edge of the cavity when the thickness of the plate varies. Figures 6.8(e) and 6.8(f) show very large amplitude of oscillations with larger thickness of the plate in comparison to those of Figs.6.8(a) through 6.8(d) with smaller plate thickness. Distributions of power spectrum density (Fig.6.9) also show that there is no peak frequency at a relatively small thickness of the plate and there are some strong peak frequencies at a relatively large thickness of the plate. The possibility of scattering of the upstream traveling compression waves becomes high as the thickness of the plate increases and these scattering effects help to regenerate further excitation of the shear layer and complete the feedback loop. Those investigations agreed well with that reported by several researchers [89, 90, 91]. Ponton and Seiner [89] showed that increasing nozzle-lip thickness helped to increase maximum screech acoustic amplitudes in upstream direction. Raman [90] described that the reflected and scattered upstream traveling acoustic waves by the larger nozzle-lip lead to a higher sound pressure level at the nozzle-lip. Jorgenson and Loh [91] showed numerically that the thick nozzle-lip exhibited a large amount of flow entrainment, leading to a counter rotating vortex upstream of the nozzle-lip. The upstream traveling compression waves were split by the rotating entrainment vortex. A large reduction of amplitudes of oscillations was obtained with the reduction of plate thickness. Maximum reduction of the oscillations was obtained with the plate of t/D = 0.05 as shown in Fig.6.8(a).

6.2.5 Effect of sub-cavity on flowfield oscillations

The results showed that the introduction of the sub-cavity together with the flat plate on the cavity front wall helped in controlling the oscillations in a favorable way such that oscillations were reduced with an increase of the depth of sub-cavity. Figure 6.10 shows the time histories of the static pressure at the position S1 on the trailing edge of the cavity of l/D = -0.25, t/D = 0.05 with the variation of the depth d of sub-cavity at the front wall. As seen from Figs.6.10(a) through 6.10(e), amplitudes of oscillations are larger than those in Figs.6.10(f) and 6.10(g). Distributions of power spectrum density (see Fig.6.11) also show that there is no peak frequency at a relatively higher depth of sub-cavity as in Figs.6.11(f) and

6.11(g) and there are some peak frequencies at a relatively smaller depth of sub-cavity as shown in Figs.6.11(a) through 6.11(e).

These observations can be explained by the fact that a sub-cavity at the front wall acts as an additional cavity with L/d >2 for the case shown in Figs.6.10(a) through 6.10(e). In addition to the reflections of upcoming compression waves on the cavity leading edge wall, reflections will also be occurred at the bottom face of the upper cavity. Those secondary reflections will reach the shear layer to excite it and consequently increase the amplitude of oscillations. Increasing the depth of sub-cavity will reduce the aspect ratio of the upper cavity and the possibility of disturbances of shear layer by the secondary reflections will be reduced. According to Tam and Block [92], for cavities with aspect ratio L/D >2, the secondary reflections of compression waves from the bottom wall of the cavity will reach the shear layer and excite it. They also described that the reflections of the upcoming compression waves from the bottom wall has an insignificant effect on the shear layer instability for a cavity with L/D <2. The result of the present simulation agrees well with that reported by Tam and Block.

Figure 6.12 shows typical density contours for the cavity without control. There exist no upstream compression waves or the reflected waves as shown in Figs. 6.12(a) through 6.12(d). As it is explained earlier that the reflected compression waves cannot disturb the shear layer strongly enough to increase the instability due to the leading edge plate. Furthermore, the instability of shear layer is not strong enough to produce compression waves. Therefore, there exists a stable shear layer in the cavity with control.

Figure 6.13 shows the streamlines of flowfield with control (l/D = -0.25, t/D = 0.05 and d/D = 0.75). There exists a large, single and stable vortex in the main cavity. Figure 6.13 also shows that in the sub-cavity there is developing another large vortex which is obstructed by the leading edge plate. Therefore, shedding of small vortices which disturbs the shear layer is discouraged here in the cavity with control and there exists a stable shear layer.

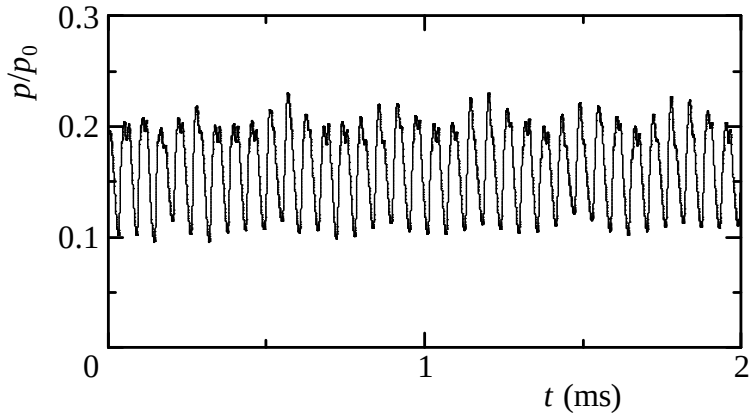

(a) Time history of static pressure

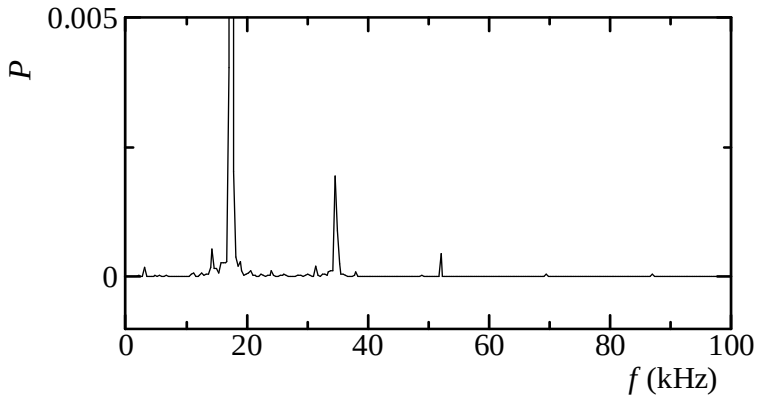

(b) Distribution of power spectrum density

Figure 6.2: Time history of static pressure and distribution of power spectrum density (without control)

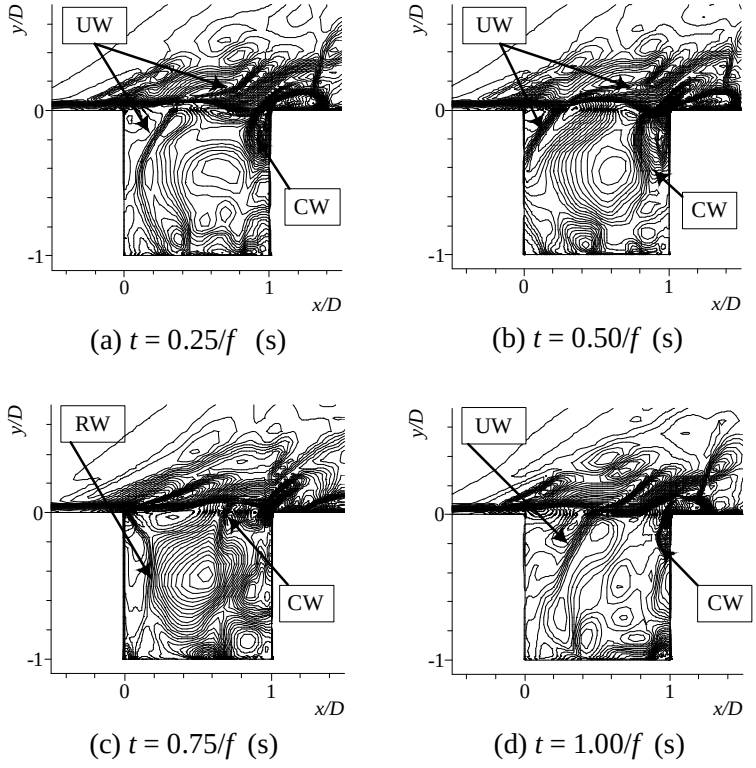

Figure 6.3: Contour maps of density (without control).

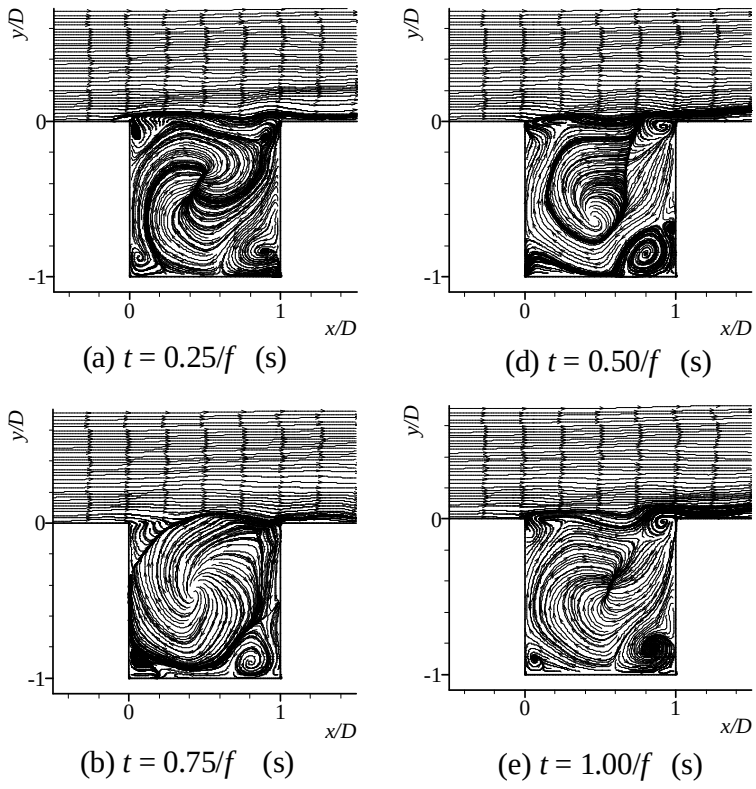

Figure 6.4: Streamline (without control).

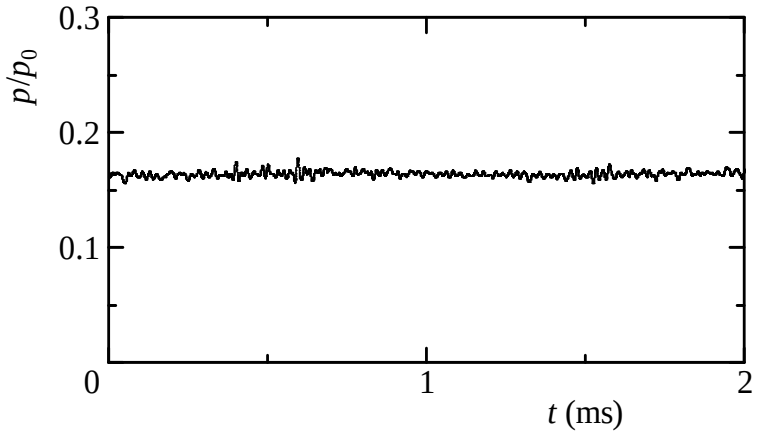

(a) Time history of static pressure

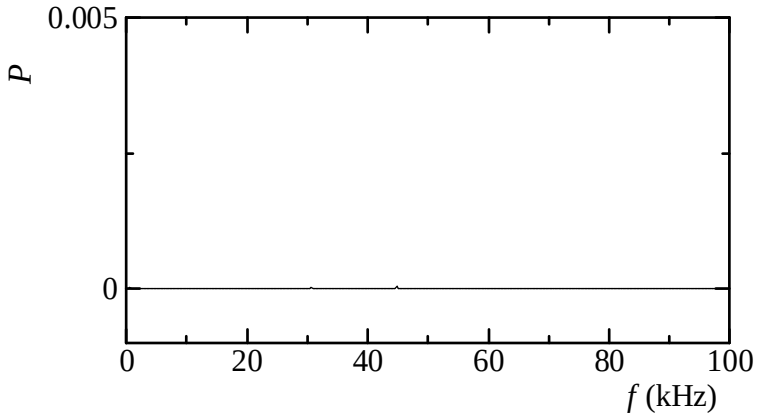

(b) Distribution of power spectrum density

Figure 6.5: Time history of static pressure and distribution of power spectrum density (with control)

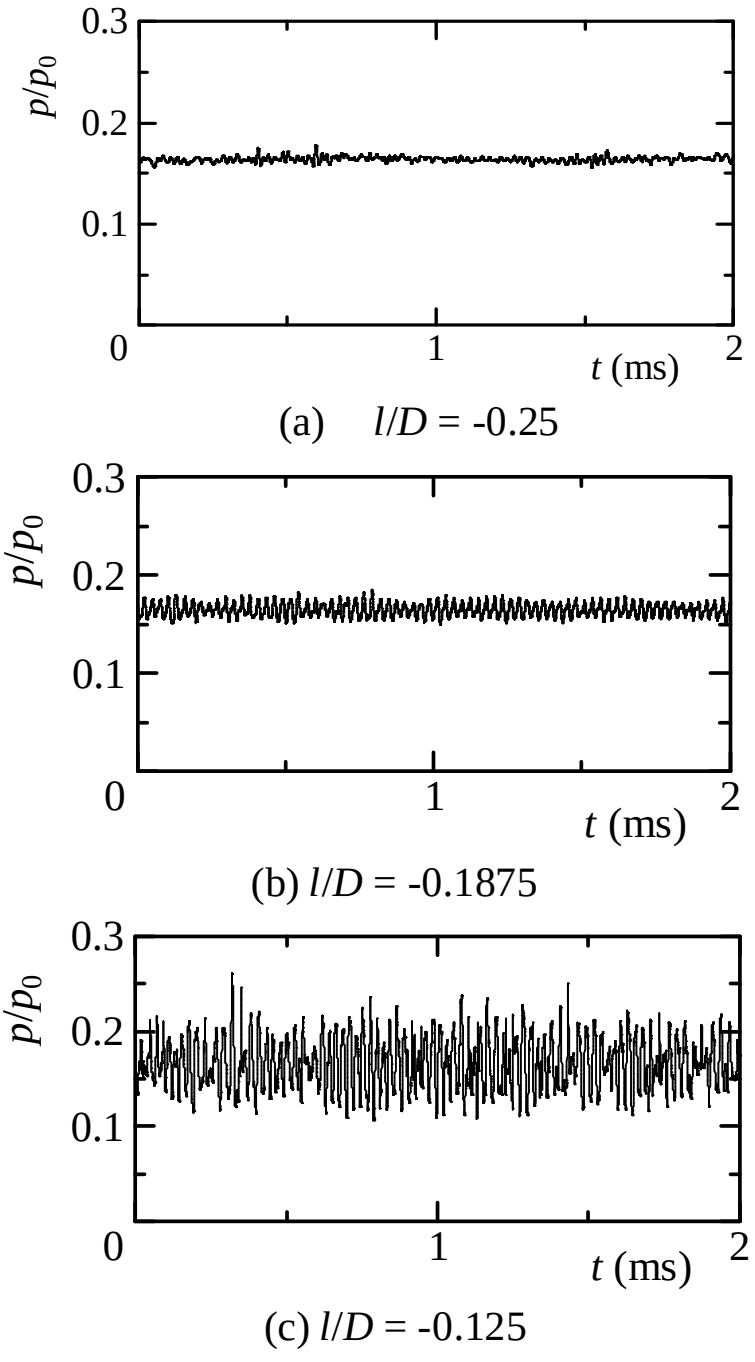

Figure 6.6: Time histories of static pressure ($t/D = 0.05$, $d/D = 1.0$).

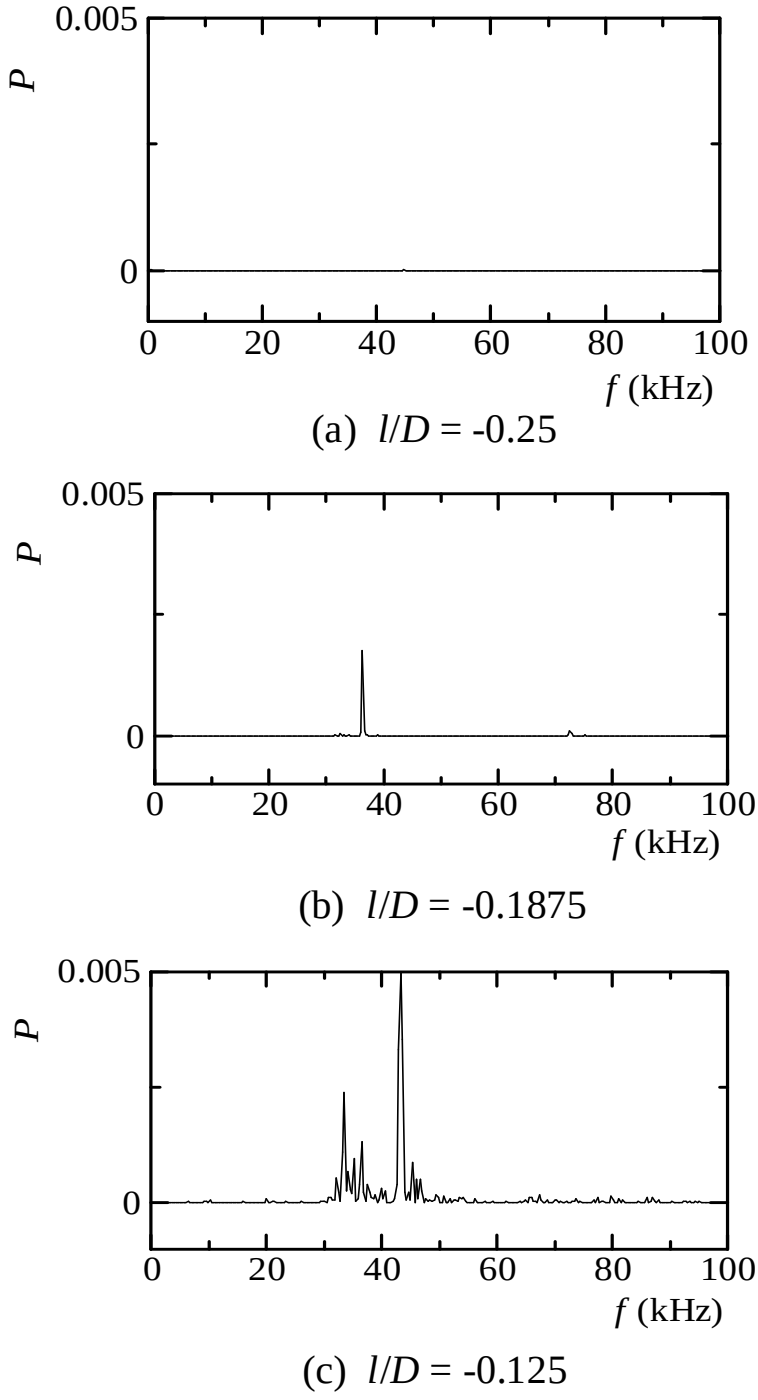

Figure 6.7: Distributions of power spectrum density ($t/D = 0.05$, $d/D = 1.0$).

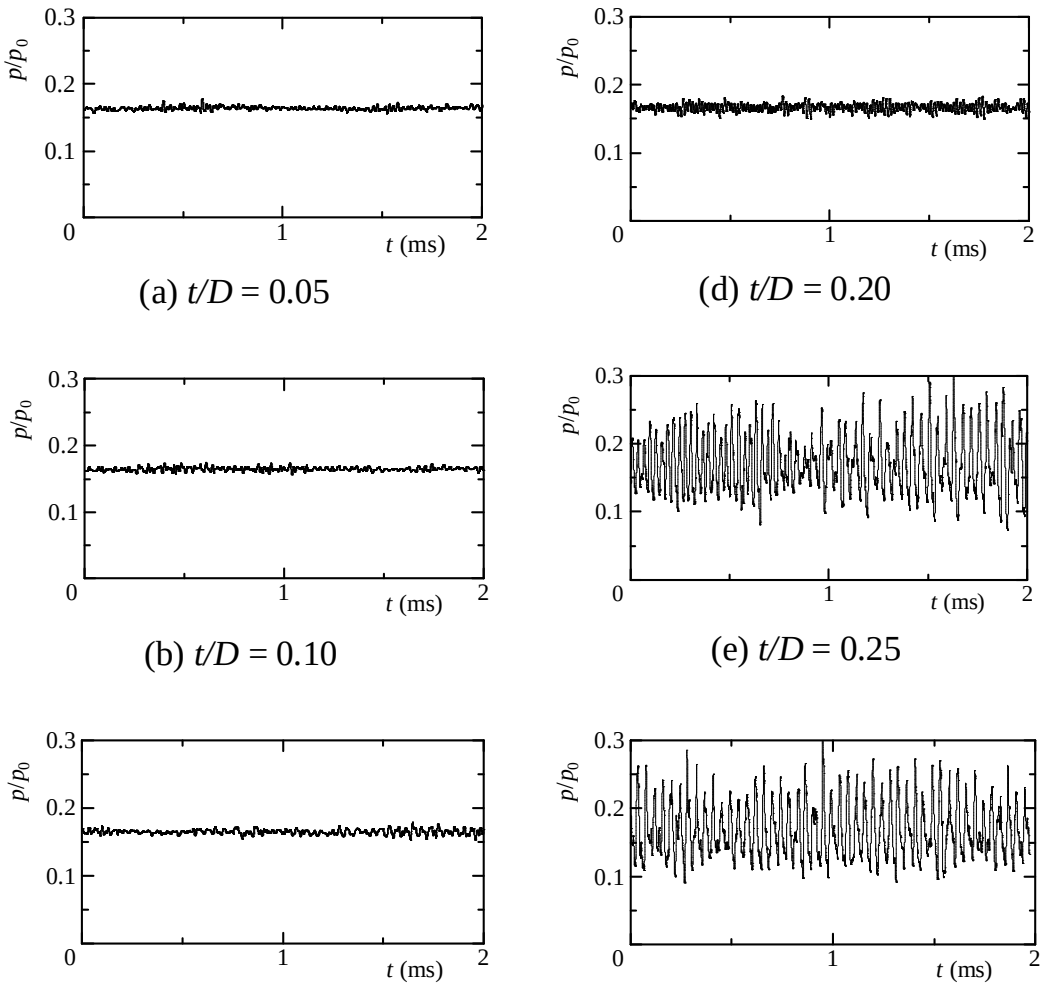

Figure 6.8: Time histories of static pressure (l/D = -0.25, d/D = 1.0).

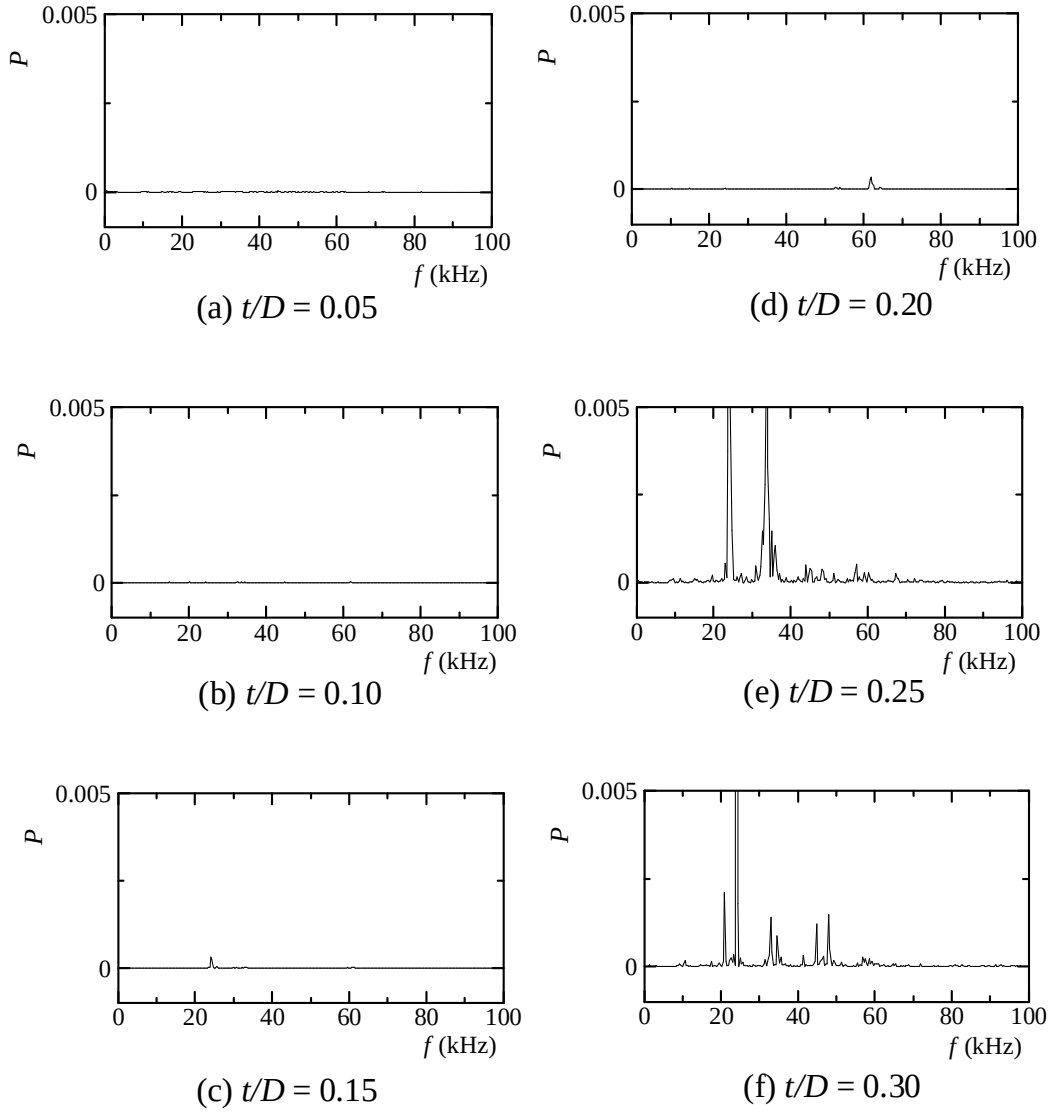

Figure 6.9: Distributions of power spectrum density (l/D = -0.25, d/D = 1.0).

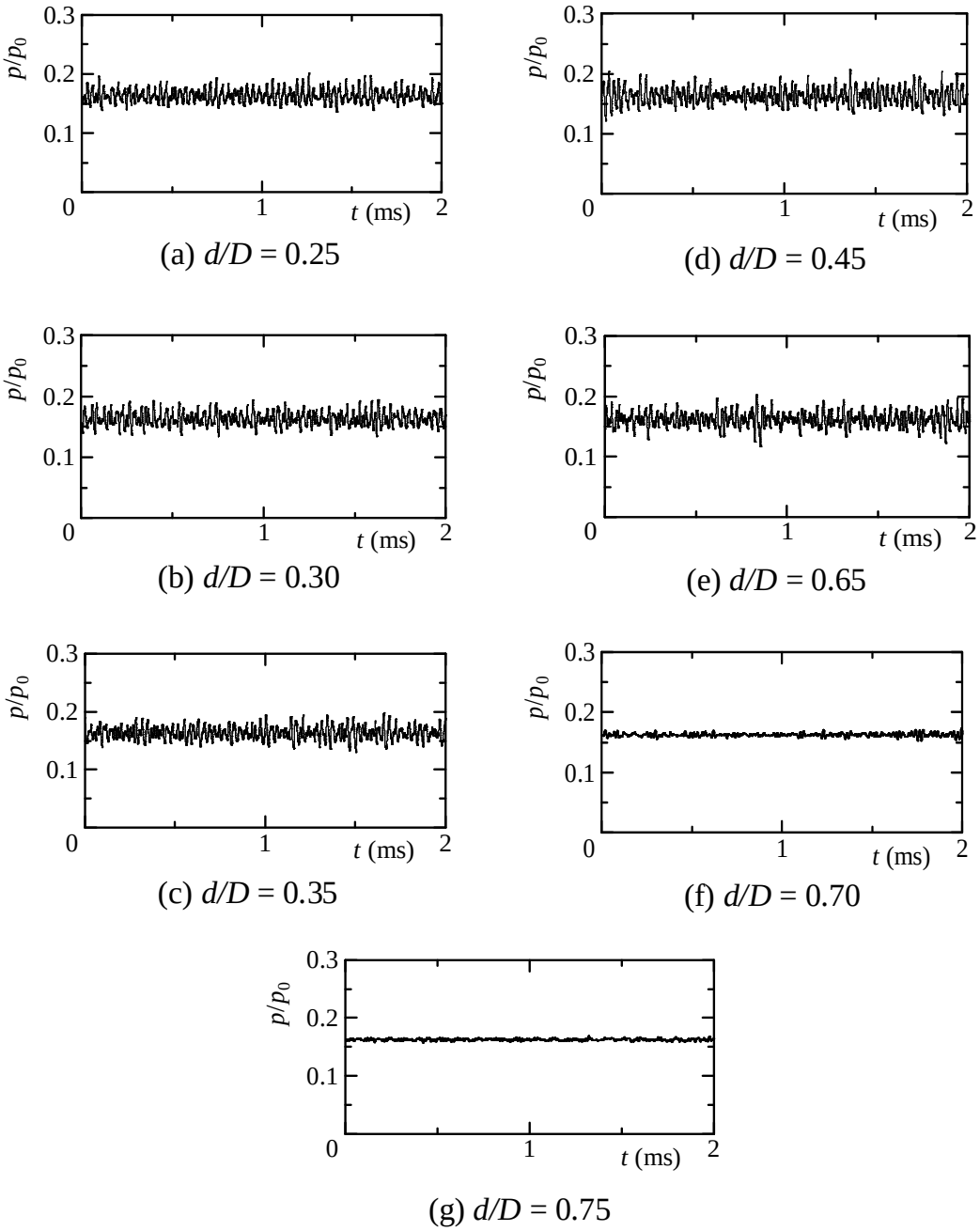

Figure 6.10: Time histories of static pressure (l/D = -0.25, $t/D = 0.05$).

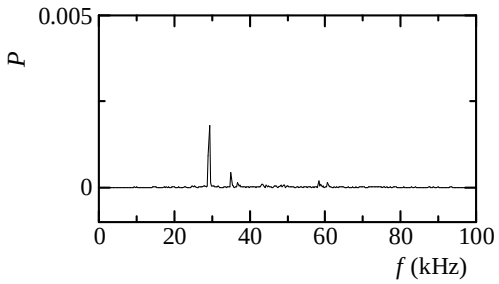

(a) *d/D* = 0.25

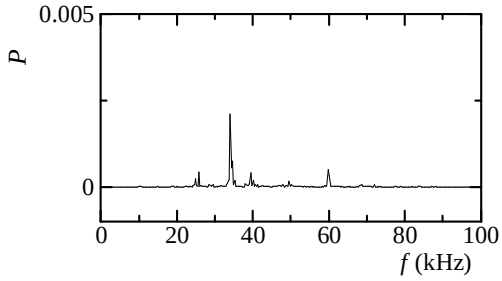

(d) *d/D* = 0.45

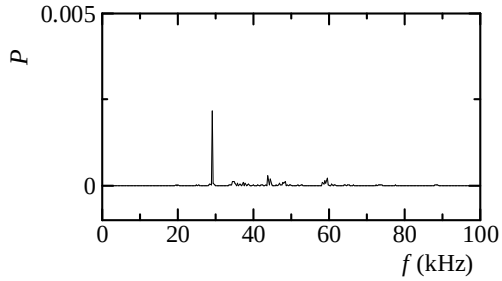

(b) *d/D* = 0.30

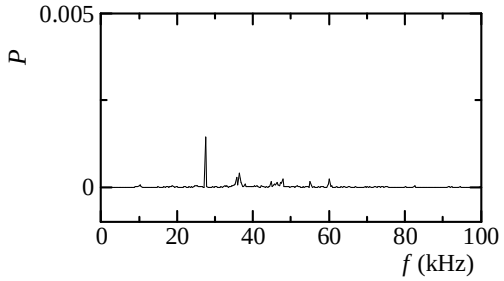

(e) *d/D* = 0.65

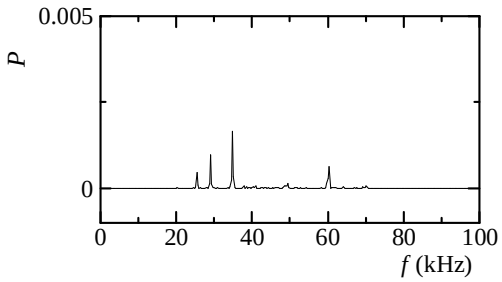

(c) *d/D* = 0.35

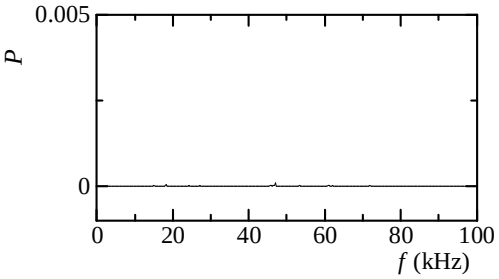

(f) *d/D* = 0.70

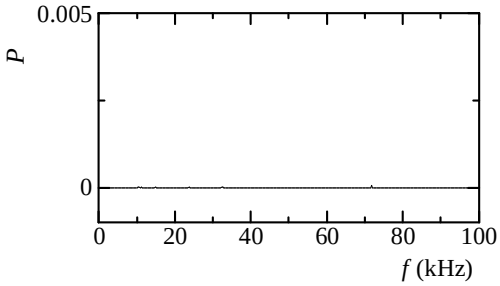

(g) *d/D* = 0.75

Figure 6.11: Distributions of power spectrum density (l/D = -0.25, t/D = 0.05).

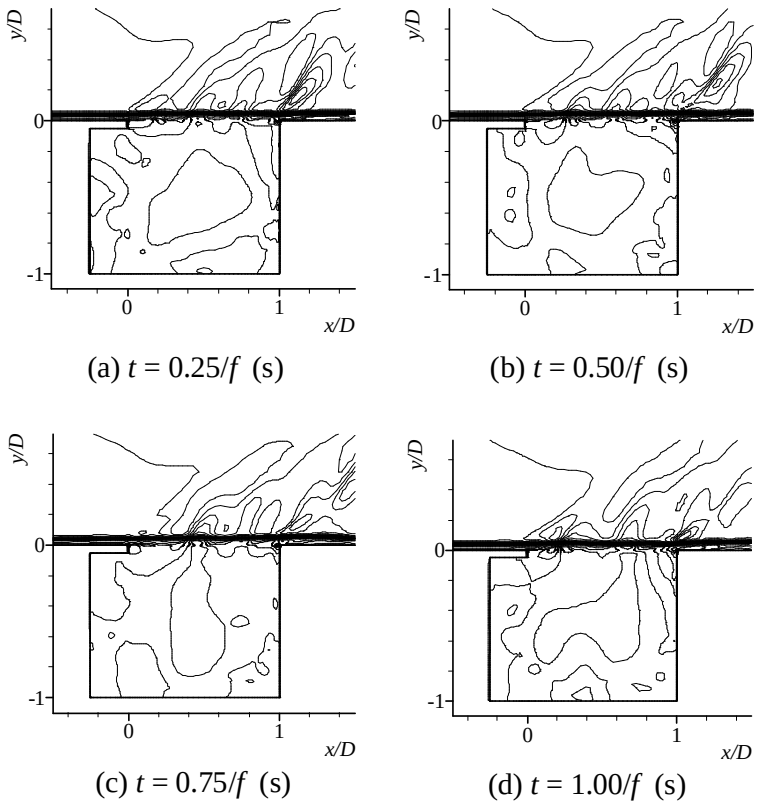

Figure 6.12: Contour maps of density (with control).

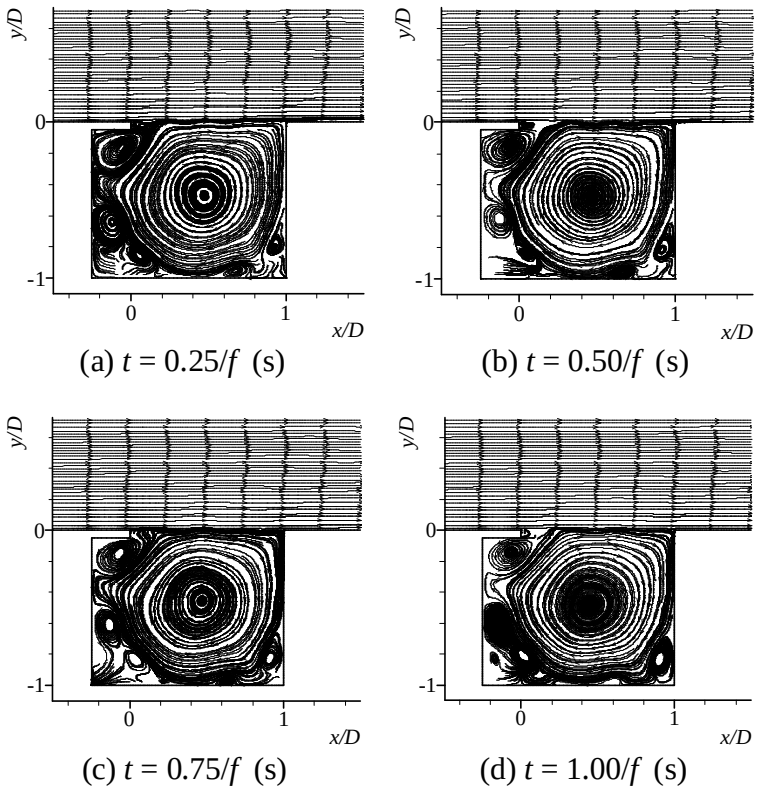

Figure 6.13: Streamline (with control).

6.3 Effect of two leading edge plates on flowfield oscillations

The proposed control devices consist of two flat plates attached near front wall of the cavity as shown in Fig.6.14. The height of the main flow section at the entrance of the cavity H is 24 mm. The depth and length of the cavity are the same (i.e., $D = W$ =12 mm). S1 in this figure denotes the measuring position of static pressure. The length of the upper horizontal plate and the depth of the vertical plate are $D/4$ and T, respectively. The length of the vertical plate was varied but the length of the horizontal plate was kept constant during the simulations. Since the plate with length l/D = -0.25 and thickness $t/D = 0.05$ is very effctive in reducing the oscillations (Figs.7.8(a) and 7.9(a)), the length and thickness of the horizontal plate are taken as l/D = -0.25 and $t/D = 0.05$, respectively. The thickness of the vertical plate is also chosen as $t/D = 0.05$ in the present simulations. The ratios of the depth of vertical plate T to the depth of the baseline cavity D are T/D = 0.25, 0.50, 0.60, 0.65 and 0.70 in the simulations. The region between the vertical plate and the cavity leading edge is defined as the sub cavity in this paper. The

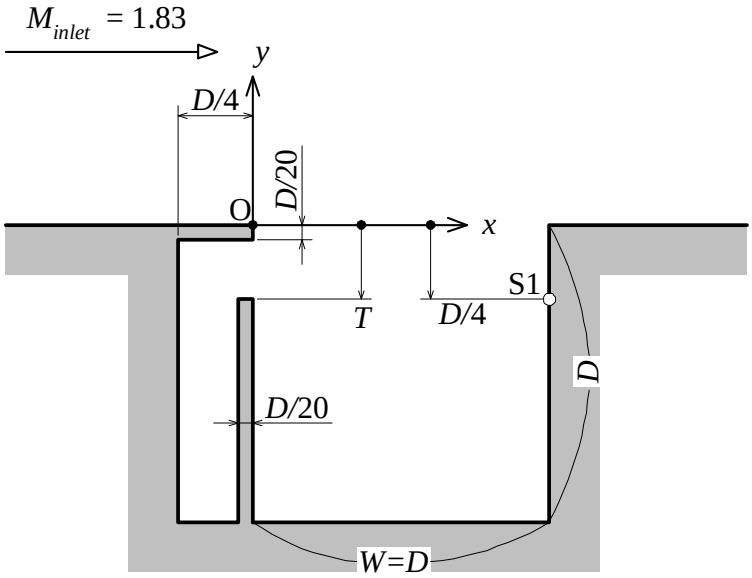

Figure 6.14: Details of cavity with two leading edge plates

number of grids is 300 × 80 in the region of the nozzle and 50 × 60 in the cavity. The origin in $x - y$ coordinate is located at the cavity leading edge. Dry air is used as a working gas and assumed to be thermally and calorically perfect. Pressure p_0 in the reservoir is 101.3 kPa. The inlet Mach number M at the entrance of the cavity is 1.83. On the solid walls, the no-slip conditions and no heat transfers were applied as the boundary conditions. Fixed conditions were set for the inflow. Zero order extrapolation was used at the outflow.

Figure 6.15(a) shows the time history of the static pressure at the position S1 for the cavity with control (when l/D = -0.25, t/D = 0.05 and T/D = 0.65). A significant amount of reduction of the amplitude of oscillations is obtained when two flat plates are used as an oscillation suppressor. Distribution of power spectrum density is shown in Fig.6.15(b). No peak frequency is found in this case. The reason of reduction of cavity pressure oscillations by the control device may be explained as the following way. The upstream traveling compression wave will be reflected off as it impinges on the front wall of the cavity. The reflected compression wave cannot strongly interact with the shear layer due to an obstruction imposed by the flat plate. Furthermore, the reflected wave becomes weaker gradually [58] as it travels downstream. As a result, the occurrence of resonance is discouraged in the cavity with control.

Simulations were also performed to determine the effect of the length of the vertical plate on the flowfield oscillations. It was observed that the length of the

vertical plate had a great influence in controlling cavity-induced pressure oscillations. Figure 6.16 shows time histories of static pressure with different lengths of the plate at the position S1 in the cavity. It shows that the amplitude of the oscillations reduces substantially with a decrease in the length of the vertical plate. Distributions of power spectrum density (Fig.6.17) showed that there were some peak frequencies when the length of the plate was relatively large (when $T/D =$ 0.25, 0.50 and 0.60) and there was no peak frequency at a relatively small length of the plate (when $T/D = 0.65$, 0.70 and 1.00). It is considered here that a decrease in the length of vertical plate allow more upstream compression waves to travel past the vertical plate and the reflected compression waves will be dissipated earlier than that of the reflected compression waves in case of longer vertical plate. For the reason, reductions of pressure oscillations are observed when $T/D = 0.65$, 0.70 and 1.00. The best performance was obtained when $T/D = 0.65$ as shown in Fig.6.15.

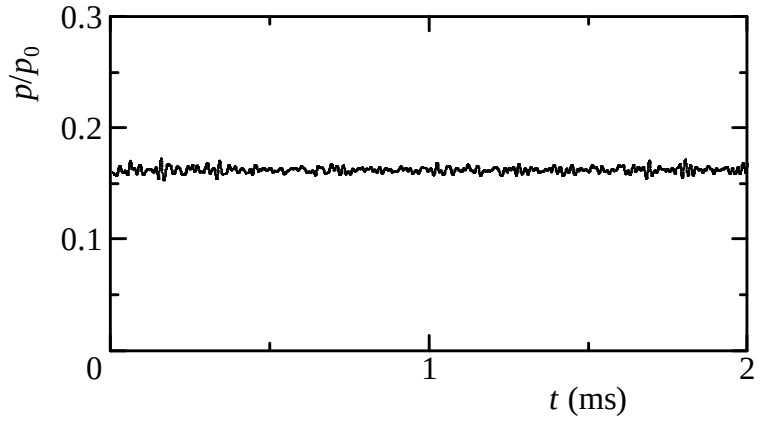

(a) Time history of static pressure

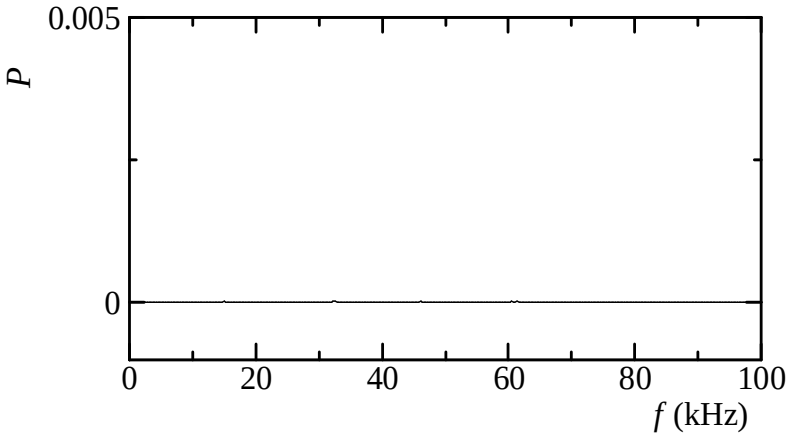

(b) Distribution of power spectrum density

Figure 6.15: Time history of static pressure and distribution of power spectrum density ($T/D = 0.65$)

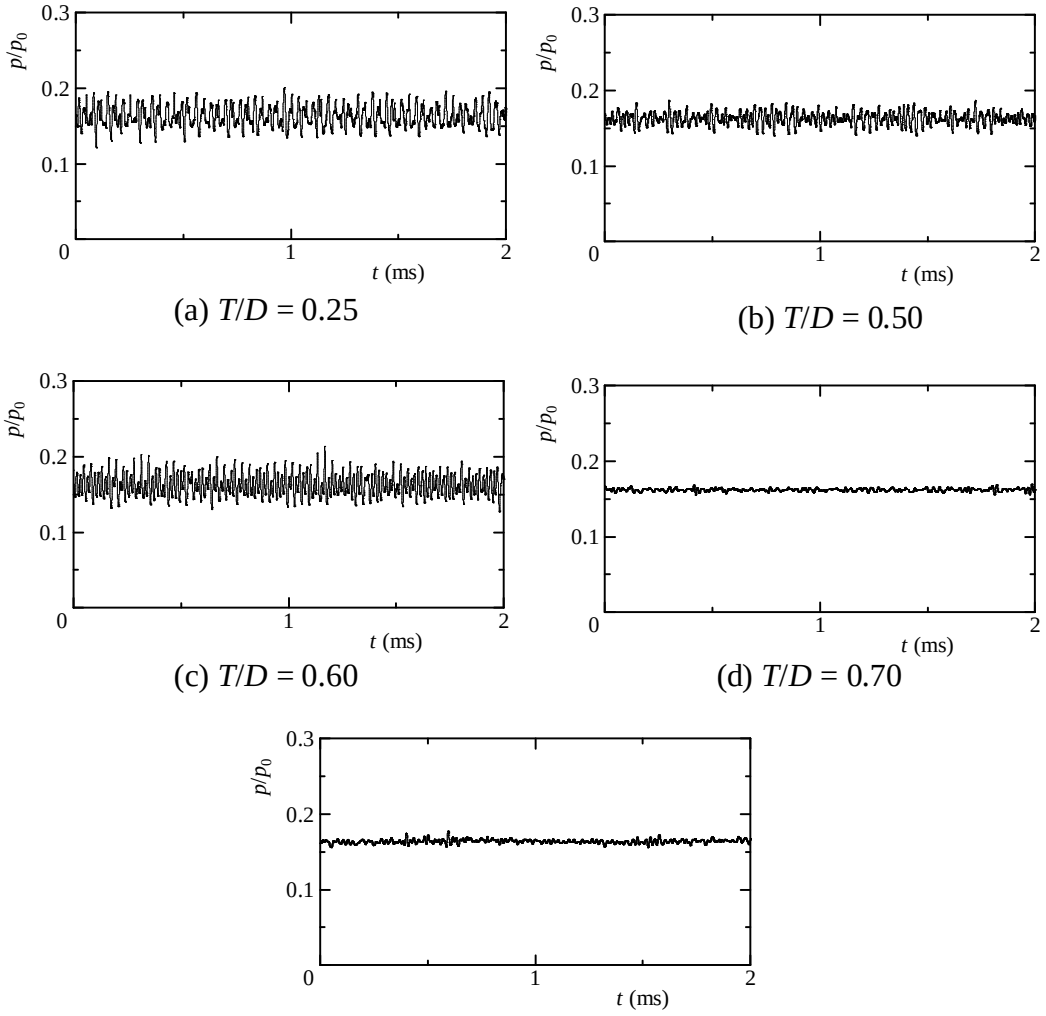

(a) $T/D = 0.25$

(b) $T/D = 0.50$

(c) $T/D = 0.60$

(d) $T/D = 0.70$

(e) $T/D = 1.00$

Figure 6.16: Time histories of static pressure

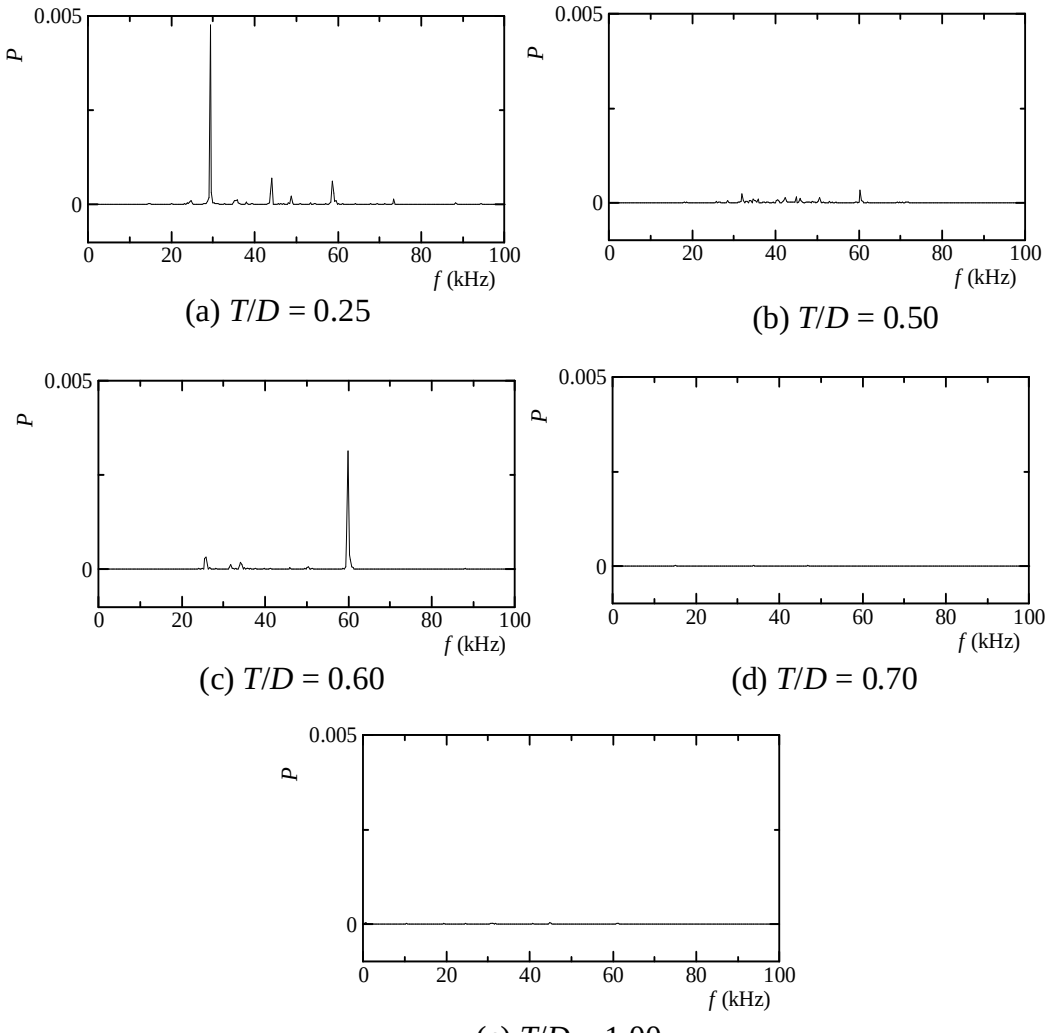

Figure 6.17: Distributions of power spectrum density

6.4 Effect of leading edge plate on the flowfield of rectangular cavities

Figure 6.18(a) shows the time history of static pressure at the position S1 inside the cavity for case with a rectangular cavity (length to depth ratio = 2.0) without control. There exist large amplitudes of oscillations at the position S1 as shown in Fig.6.18(a). Distribution of power spectrum density obtained from the static pressure history is shown in Fig.6.18(b). There are peak frequencies at cavity without control.

Figure 6.19(a) shows the time history of static pressure at the rectangular cavity with control. A reduction of the amplitudes was obtained when a flat plate is introduced in the cavity (when l/D = -0.50, t/D = 0.05, d/D = 1.0, and L/D = 2.0) Distribution of power spectrum density at the same rectangular obtained from the static pressure histories is shown in Fig.6.19(b). There are peak frequencies for case with control as shown in the Fig.6.19(b) (when l/D = -0.50, t/D = 0.05, d/D = 1.0, and L/D = 2.0).

Figure 6.20(a) shows the time history of static pressure at the position S1 inside a rectangular cavity (length to depth ratio = 3.0) without control. There exist large amplitudes of oscillations at the position S1 as shown in Fig.6.20(a). Distribution of power spectrum density obtained from the static pressure history is shown in Fig.6.20(b). There are peak frequencies in case of cavity without control.

Figure 6.21(a) shows the time history of static pressure at the rectangular cavity with control. A reduction of the amplitudes was obtained when a flat plate is introduced in the cavity (when l/D = -0.75, t/D = 0.05, d/D = 1.0, and L/D = 3.0) Distribution of power spectrum density at the same rectangular obtained from the static pressure histories is shown in Fig.6.21(b). There are peak frequencies for case with control as shown in the Fig.6.21(b) (when l/D = -0.75, t/D = 0.05, d/D = 1.0, and L/D = 3.0).

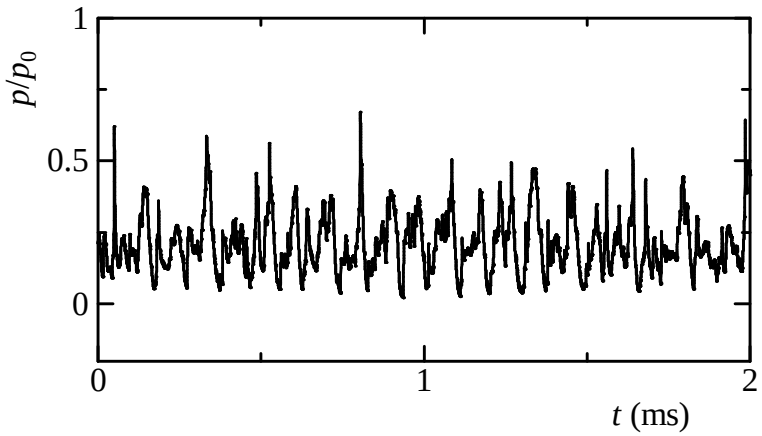

(a) Time history of static pressure

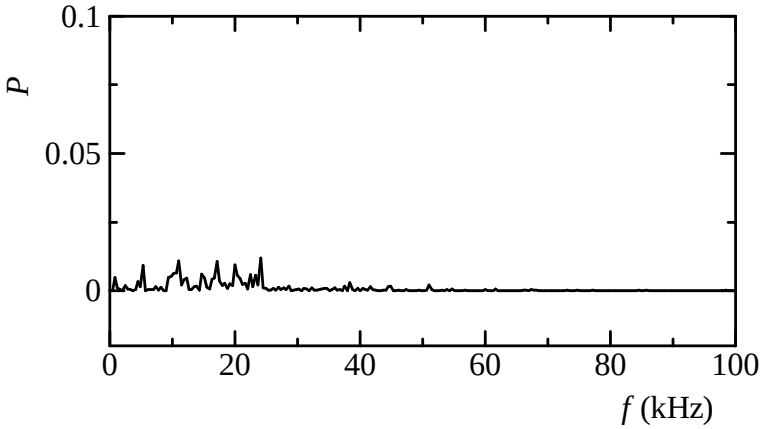

(b) Distribution of power spectrum density

Figure 6.18: Time history of static pressure and distribution of power spectrum density without control ($L/D = 2.0$)

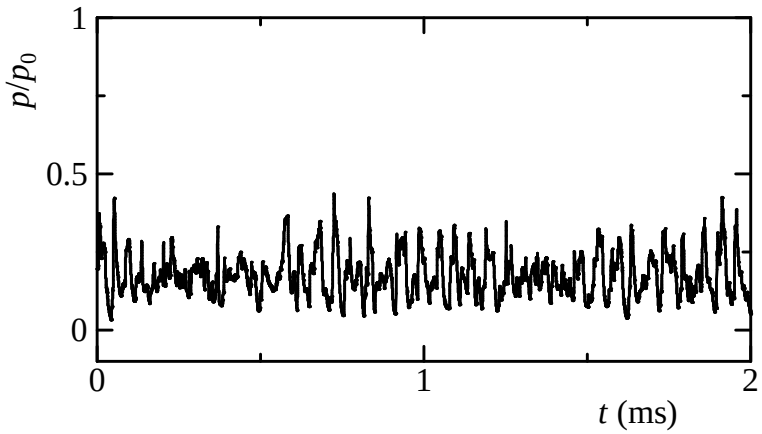

(a) Time history of static pressure

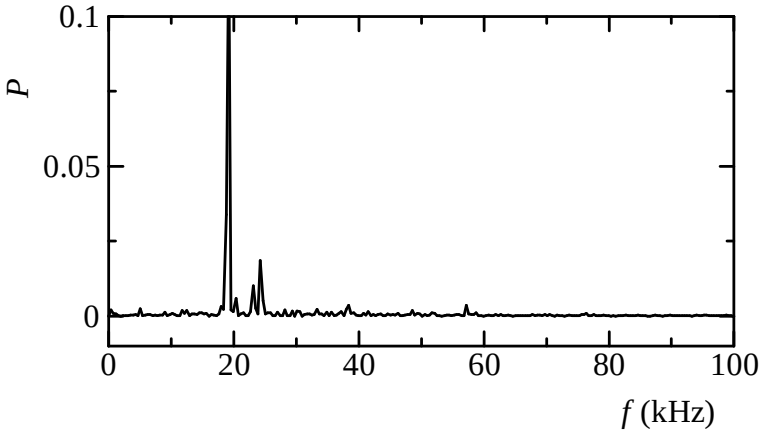

(b) Distribution of power spectrum density

Figure 6.19: Time history of static pressure and distribution of power spectrum density (l/D = -0.25, t/D = 0.05, d/D = 1.0, and L/D = 2.0)

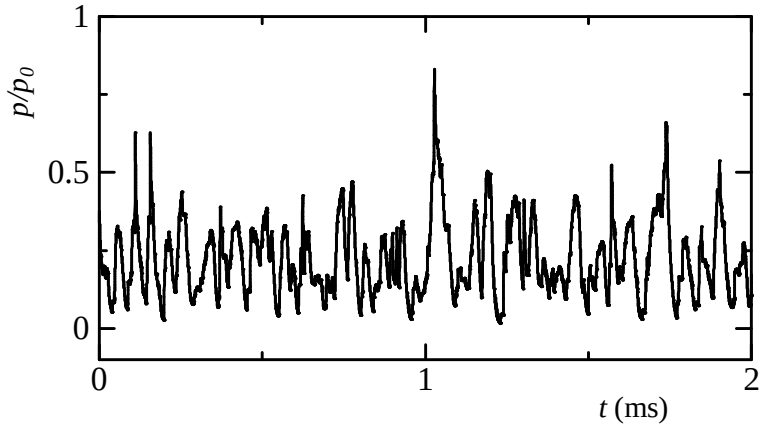

(a) Time history of static pressure

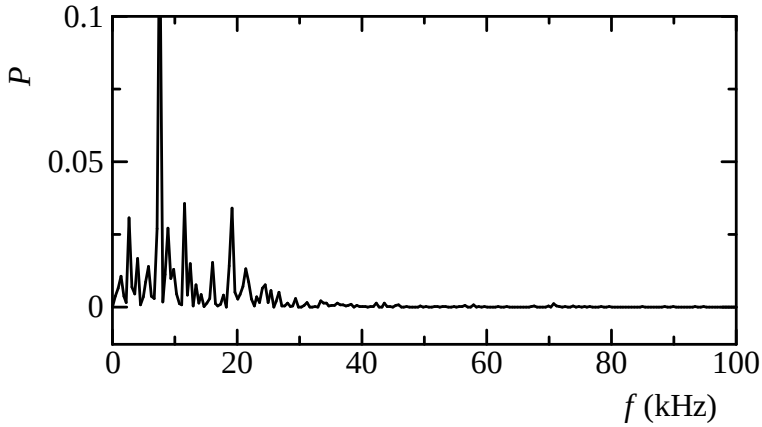

(b) Distribution of power spectrum density

Figure 6.20: Time history of static pressure and distribution of power spectrum density without control ($L/D = 3.0$)

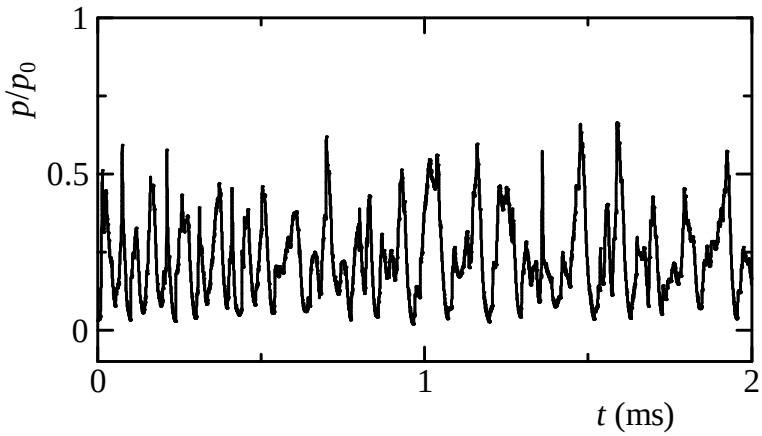

(a) Time history of static pressure

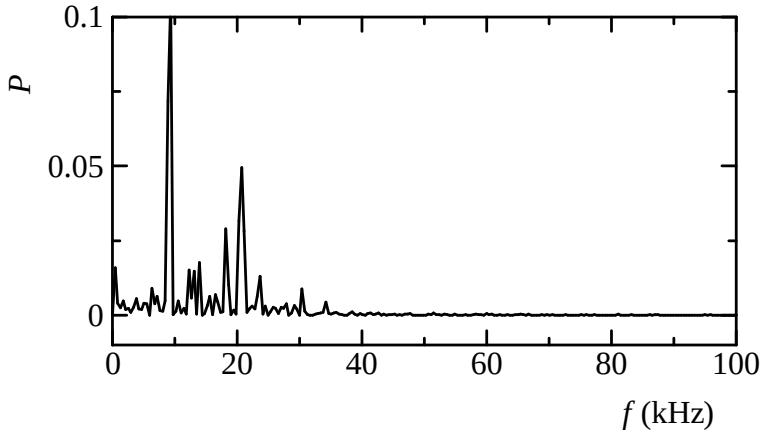

(b) Distribution of power spectrum density

Figure 6.21: Time history of static pressure and distribution of power spectrum density (l/D = -0.25, t/D = 0.05, d/D = 1.0, and L/D = 3.0)

6.5 Experimental investigation

6.5.1 Experimental conditions

In order to investigate the flowfield oscillations of cavity without control, both flow visualization and pressure measurements were performed in a cavity with depth and the length are the same (See Fig.6.22) and equal to 12 mm. Pressure p_0 and temperature T_0 of air in the reservoir are 101.3 kPa and 298.15 K, respectively. Dry air with initial degree of supersaturation, $S_0 = 0$ is used in the present experimental investigation. The inlet Mach number M_{inlet} at the entrance of the cavity is 1.83.

In order to visualize detailed flow structures, a Schlieren optical system was employed in the present experimental investigation. The Schlieren photograph is shown in Fig. 6.23.

6.5.2 Pressure measurement results

Figures 6.24(a) shows the time history of the static pressure in the cavity without control. There exist large amplitudes of oscillations without control as shown in Fig.6.24(a). Distributions of power spectrum density at the same position obtained from the static pressure histories are shown in Fig.6.24(b). There are dominant frequencies in case of cavity without control (Fig.6.24(b)).

6.6 Comparison between simulation and experimental results

In order to validate the computational code developed for the present numerical simulation, a two-dimensional open square cavity of length to depth ratio = 1.0 at Mach number M_{inlet} =1.83 at the cavity entrance was investigated in case without control and the solutions were compared with the present experimental results. The solutions were also compared with the experimental and numerical results of other researchers [49, 93, 60]. Figure 6.25 shows a comparison of the Strouhal numbers St among numerical, experimental and theoretical results. Open circle represents the experimental results reported by Zhang and Edwards [49] and Takakura et al. [93]. Solid lines are drawn by using the formulae of predicting oscillation frequencies proposed by Nishioka et al. [60]. Closed circle represents the results of the present simulation and the triangle represents the results of present experiments. The comparison shows a fairly good agreement between the present simulated and experimental results. The results also show a good agreement with the experimental and theoretical results of other researchers [49, 93, 60].

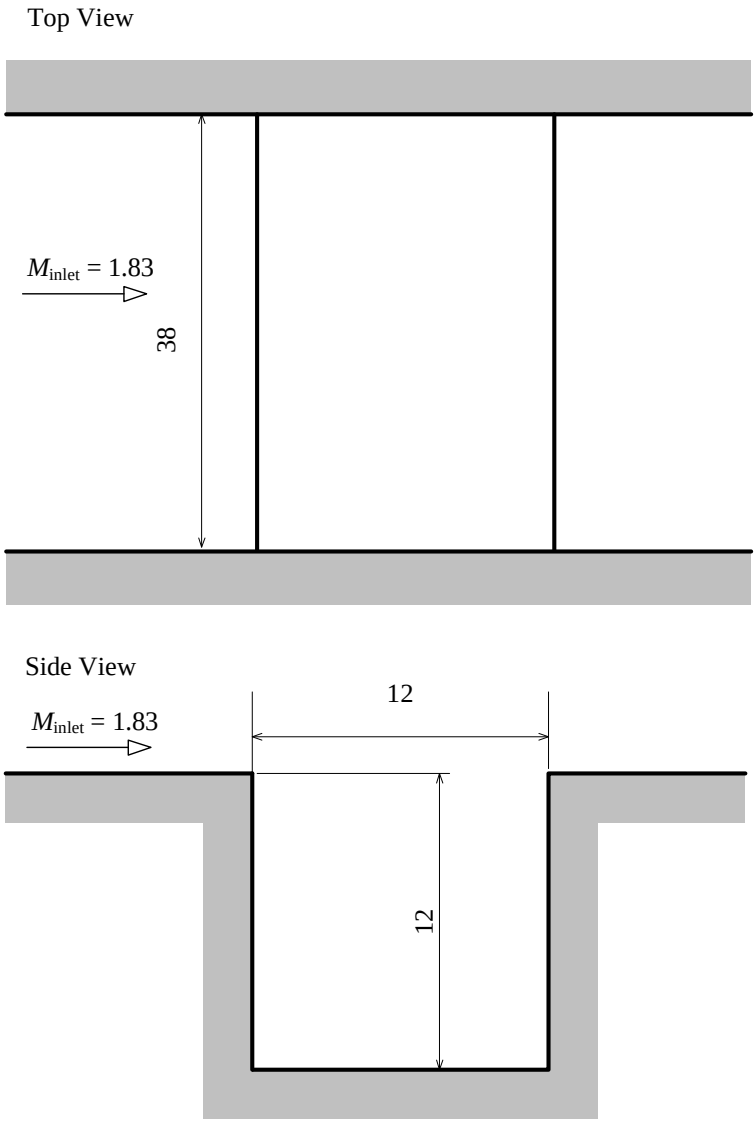

Figure 6.22: Details of cavity configuration

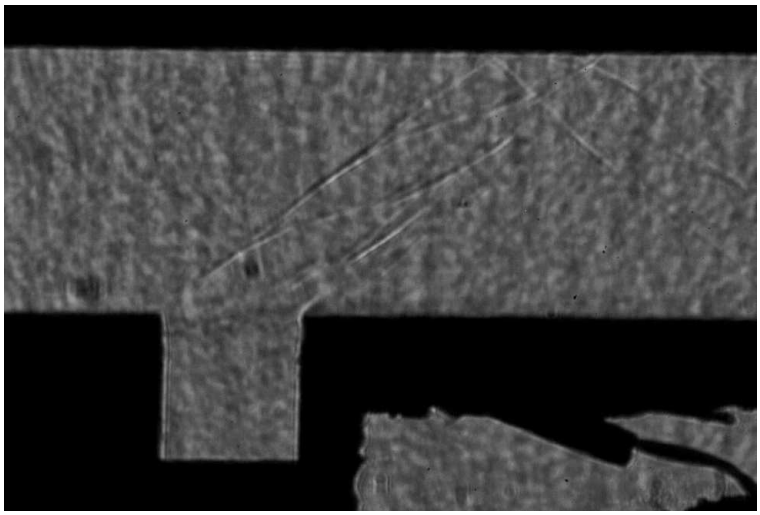

Figure 6.23: Schlieren photograph of cavity without control

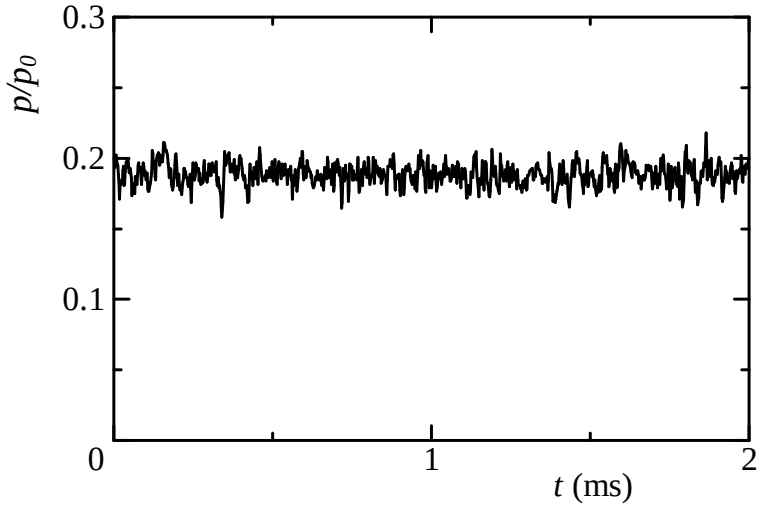

(a) Time history of static pressure

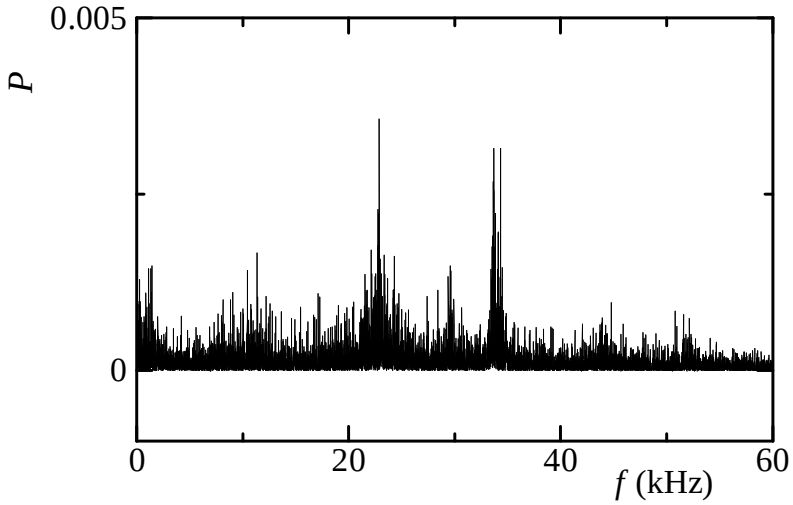

(b) Distribution of power spectrum density

Figure 6.24: Time history of static pressure and distribution of power spectrum density (without control)

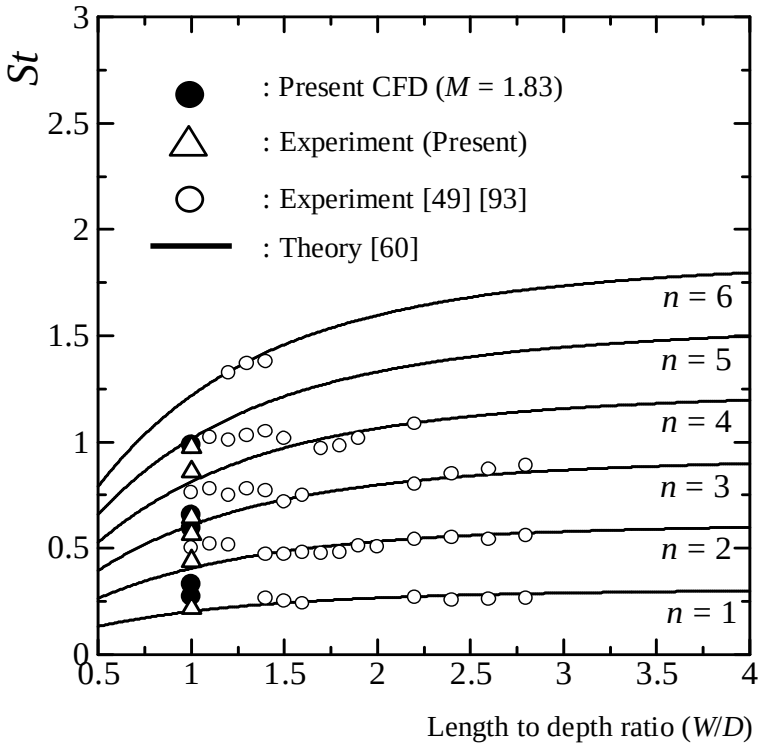

Figure 6.25: Comparison of simulation results with experimental and theoretical results

6.7 Summary

Computational investigation has been carried out for a supersonic two-dimensional flow over open, square cavities at Mach number 1.83 at the cavity entrance. A sub-cavity on the front wall of the cavity with a flat plate had been investigated for the effectiveness of controlling cavity pressure oscillations. The results showed that the length and thickness of the flat plate had a great influence in controlling the cavity-induced acoustic oscillations. The amplitudes of the oscillations were reduced substantially with an increase of the length of the flat plate. Furthermore, a decrease in the plate thickness also assisted to suppress the oscillations remarkably. The results also showed that the resultant amount of attenuation of cavity-induced acoustic oscillations was dependent on the depth of the sub-cavity.

CHAPTER 7
EFFECT OF POROUS WALL ON THE OSCILLATIONS

7.1 Conditions of numerical simulations

Figure 7.1 shows the grids and computational domain of the cavity. The height of the main flow section above the cavity is 24 mm. The origin O in $x-y$ coordinate is located at the leading edge of the cavity.

The objective of this paper is to determine the effectiveness of the proposed devices as a controller of cavity-induced pressure oscillations in a two-dimensional flow. Since the flowfield of a square cavity is two-dimensional according to Sakamoto et. al. [87], a square cavity has been investigated in this present computational study. The cavity depth and length are the same (i.e., D =12 mm). S1 in this figure denotes the measuring position of static pressure. Control devices consist of a sub-cavity and a porous wall attached in the cavity as shown in Fig. 7.1(b). The region between the porous plate and the cavity leading edge is defined as sub-cavity in this paper. The length and depth of the sub-cavity are L and D, respectively. The upper portion of the sub-cavity is covered by a leading edge plate of length L. Here porosity P is defined as the ratio of summation of the lengths of perforations (holes) in the porous wall to the total length of the wall. T_1 and T_2 indicate the size of perforation and length between two consecutive perforations of the porous plate, respectively. The parameters of cavity configuration for all the simulations performed are summarized in Table 7.1. The number of grids is 300×80 in the region of the main flow and 50×60 in the cavity.

In the present study, dry air is used as a working gas and assumed to be thermally and calorically perfect. Pressure p_0 in the reservoir is 101.3 kPa. The inlet Mach number M_{inlet} at the entrance of the cavity is 1.83. The Reynolds number is 2.1×10^5. On the solid walls, the no-slip conditions and no heat transfers were applied as the boundary conditions. Fixed conditions were set for the inflow boundary. Zero order extrapolation was used at the outflow boundary.

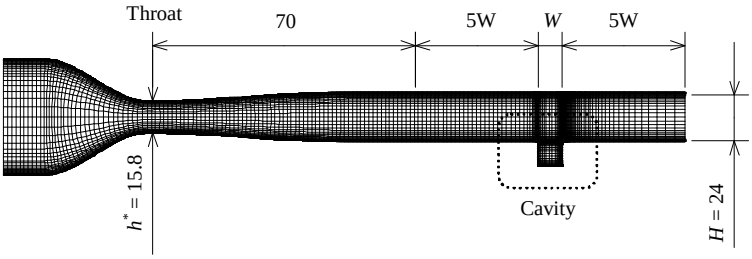

(a) Computational grids (Unit : mm)

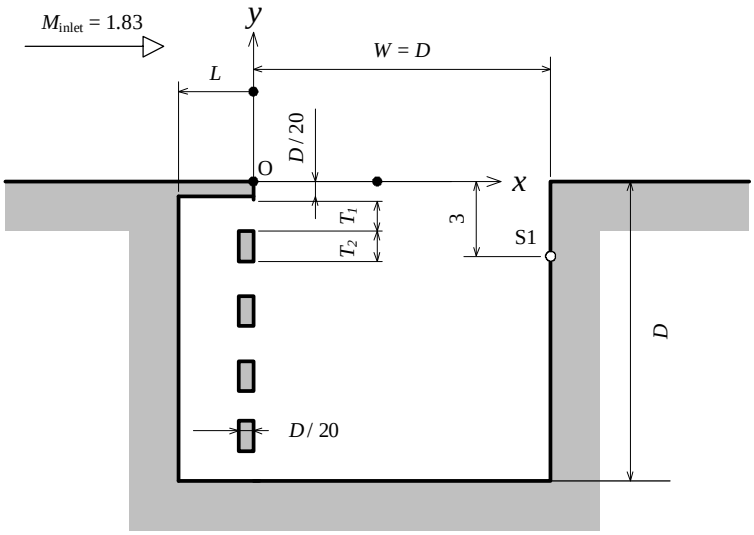

(b) Details of cavity configuration

Figure 7.1: Computational domain

Table 7.1: Parameters of cavity configuration

Parameters	T_1/D	T_2/D	L/D	$Porosity$
Without control	0	1	0	0
Case 1	0.10	0.10	-0.25	0.5
Case 2	0.10	0.10	-0.15	0.5
Case 3	0.10	0.10	-0.05	0.5
Case 4	0.05	0.05	-0.25	0.5
Case 5	0.15	0.15	-0.25	0.5
Case 6	0.10	0.07	-0.25	0.6
Case 7	0.10	0.183	-0.25	0.4
Case 8	0.10	0.216	-0.25	0.3
Case 9	0.10	0.375	-0.25	0.2

7.2 Analysis of simulation data

7.2.1 Effect of porous wall

There exist large amplitudes of oscillations at the position S1 in the cavity without control as shown in Fig.7.2(a). Distribution of PSD (power spectral density) at the same position obtained from the static pressure histories is shown in Fig.7.3(a). There is a dominant frequency at 17.5 kHz in case of cavity without control. On the other hand, a substantial reduction of oscillations was obtained when the front wall of the cavity was replaced by a sub-cavity with a porous wall as shown in Fig.7.2(b). Figure 7.2(b) show the time history of the static pressure at the position S1 for Case 1 with control. A significant amount of reduction of the amplitude of oscillations is obtained in the Case 1 as shown in Fig.7.2(b). PSD diagram (Fig.7.3(b)) also shows that there is no peak frequency in this case.

Contour maps of density (see Fig.7.4) show the flowfield with control. A reduction of oscillations and a more stable shear layer are found for a cavity with control as shown in Figs.7.2(b) and 7.4, respectively.

Figure 7.5 shows streamline contours resulting from the use of a porous wall with a sub-cavity (Case 1). It is clear from Figs.7.5(a) through Fig.7.5(d) that mass extraction and injection occur along the porous wall [23]. In their pseudo-perforated walls study, Sasoh et al. [94] showed that when a shock wave passes the entrance of perforation, it diffracts at the entrance of the perforation and expansion waves are generated. They also reported that when the perforation depth is shallow like the depth of present investigation and is connected to an open space (sub-cavity), expansion waves are generated on both sides of the opening. The reflected compression waves are attenuated due to the interaction of compression waves with expansion waves which are generated at the perforations. Therefore, this exchange of mass between sub-cavity and main cavity through the perforation with the generation of expansion waves helps in attenuating the resulting compression waves. Furthermore, Quinn [88] and Franke and Carr [31] showed that vortices were shed as the upstream traveling compression waves reflected from the forward bulkhead of the cavity. Here, the shedding of vortices is obstructed by the flat plate leaving a stable shear layer with reduced oscillations.

7.2.2 Effect of sub-cavity formed by porous plate and front wall of cavity

Observations were made by changing length of the sub-cavity (also the length of the leading edge plate) to investigate its effect on the cavity pressure oscillations. In Cases 1, 2 and 3, the porosity and the size of perforations T_2/D were 0.5 and 0.10, respectively. The simulation results show a considerable amount of attenuation of the amplitudes of oscillation in the case with a sub-cavity as shown in Figs.7.2 (b) and 7.6(a). It is also evident form the PSD diagrams that there is no peak frequency as shown in Fig. 7.7(a). When no sub-cavity or leading edge plate was provided at the front wall of the cavity, the cavity behaved liked an uncontrolled cavity. Therefore, large increase of oscillations was observed in the cavity without a sub-cavity. Increased amplitudes of oscillations (Fig.7.6(b)) and a very strong peak (Fig.7.7(b)) in Case 3 without a sub-cavity make it an unsatisfactory device to use as an oscillation suppressor.

7.2.3 Effect of size of perforations

The effect of the size of perforation on the cavity flowfield is also investigated in this computational study by using a porous wall with T_1/D=0.10 (Case 1), 0.05 (Case 4) and 0.15 (Case 5). It was observed that the size of perforation had some effects in controlling cavity flowfield oscillations. Figure 7.2(b) shows a substantial reduction of amplitude of oscillations at the position SI in the cavity controlled by

a sub-cavity with a porous wall (Case 1). A slight increase in the amplitudes of oscillations is observed for Cases 4 (Fig.7.8 (a)) and 5 (Fig.7.8 (b)) compared with that of Case 1 (Fig.7.2 (b)). Distributions of power spectrum density diagrams obtained form the histories of static pressure at the same position S1 inside the cavity also showed some very small peak frequencies for Cases 4 and 5.

7.2.4 Effect of porosity

Observations were also made to know the effect of porosity of the wall on the flowfield of the cavity. Porous wall with porosity $P = 0.2$ (Case 9), 0.3 (Case 8), 0.4 (Case 7), 0.5 (Cases 1 through 5) and 0.6 (Case 6) were tested to determine their effectiveness in controlling oscillations. It was observed that porous wall with porosity $P = 0.4$ and 0.5 were most effective in reducing cavity pressure oscillations as shown in Figs. 7.9(b) and 7.2(b), respectively. From those figures, it is evident that the amplitude of oscillations is reduced remarkably. Power spectrum density diagrams obtained from histories of static pressure also showed that there are no peak frequencies when the porosity is 0.4 and 0.5. An increase of amplitude of oscillations were found when the porosity were 0.6 (Fig.7.9(a)), 0.3 (Fig.7.9(c)), and 0.2 (Fig.7.9(d)). A decrease in the porosity causes the solid surface area of the porous wall to increase. This increased area of reflection will increase the strength of the reflected compression waves. These stronger reflected waves will disturb the shear layer to increase the instability and thereby increase the oscillations. For this reason the oscillations were increased when the porosity was 0.3 and 0.2.

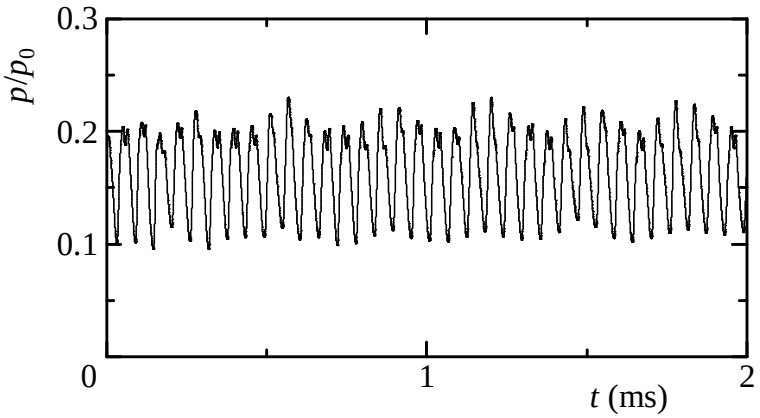

(a) Without control

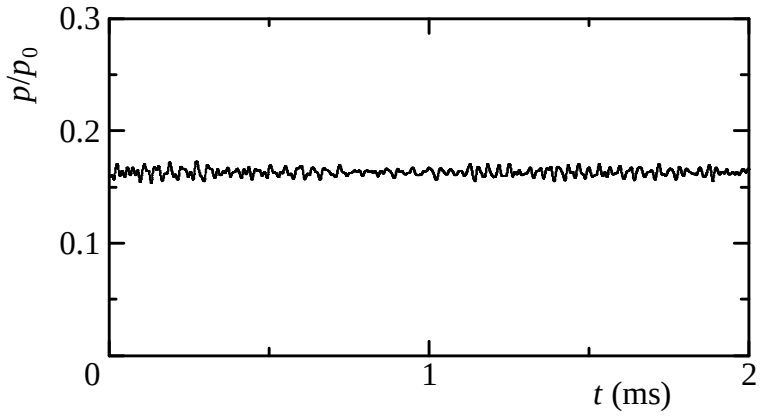

(b) Case 1

Figure 7.2: Time histories of static pressure

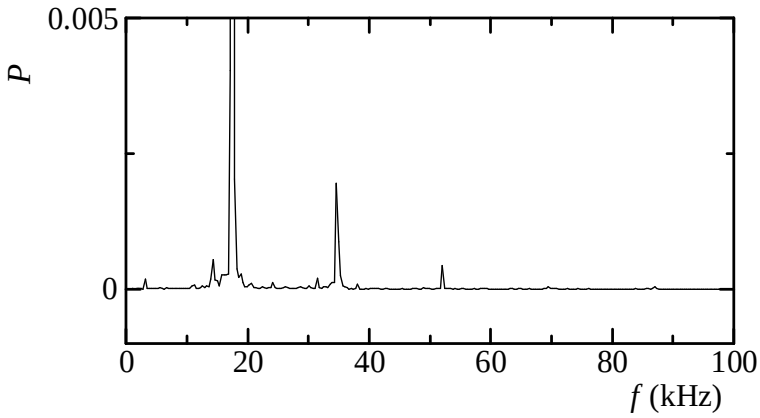

(a) Without control

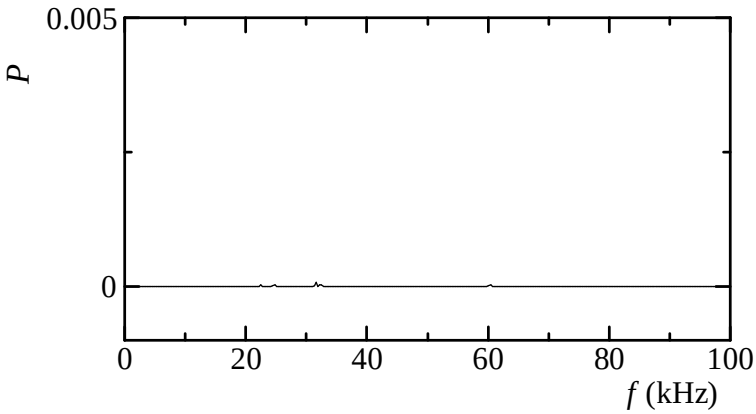

(b) Case 1

Figure 7.3: Distributions of power spectrum density

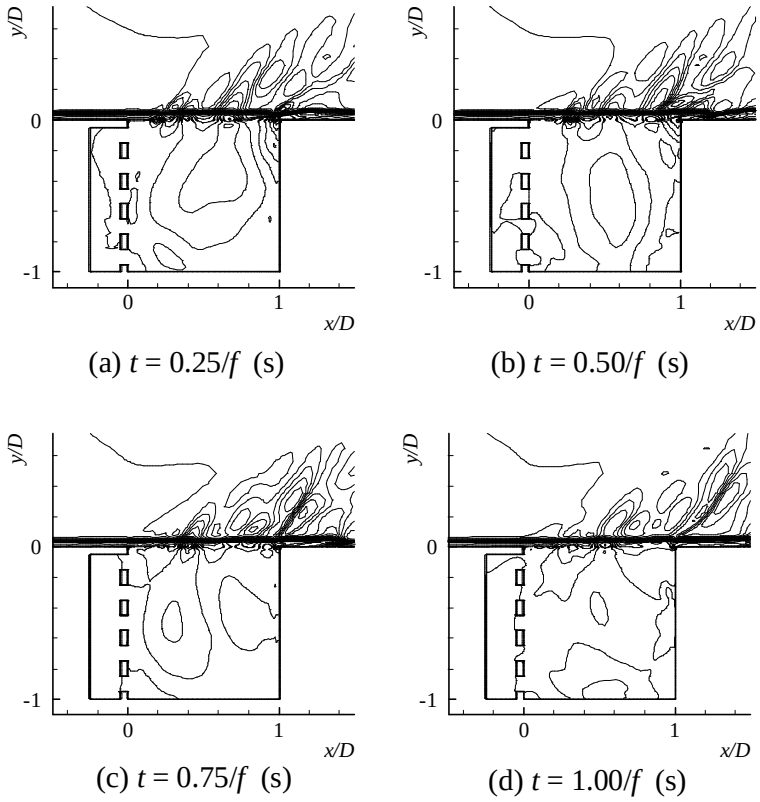

Figure 7.4: Contour maps of density showing the flowfield (Case 1)

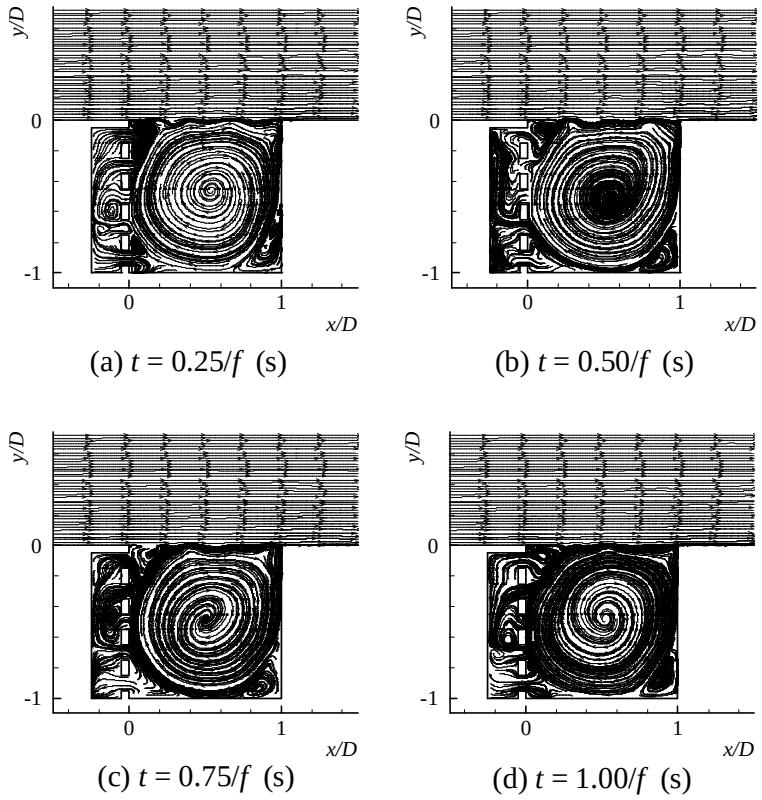

(a) $t = 0.25/f$ (s) (b) $t = 0.50/f$ (s)

(c) $t = 0.75/f$ (s) (d) $t = 1.00/f$ (s)

Figure 7.5: Streamline (Case 1).

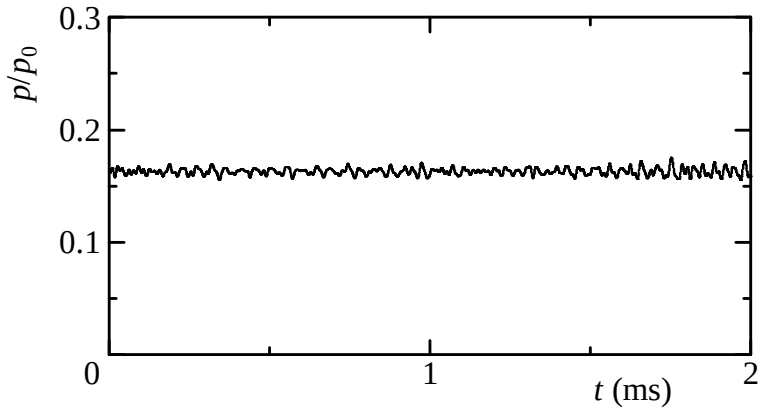

(a) Case 2

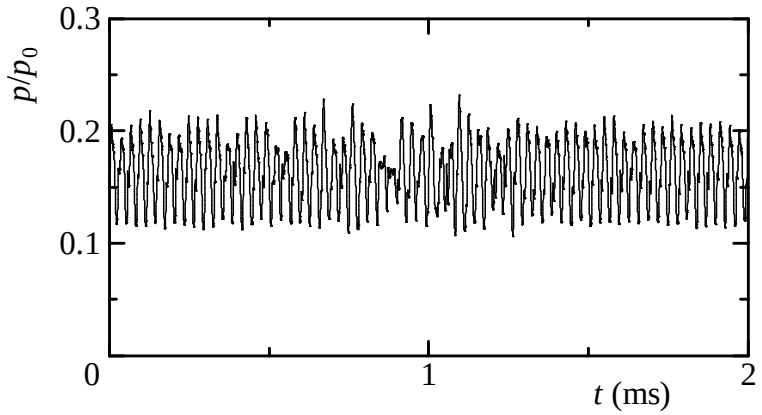

(b) Case 3

Figure 7.6: Time histories of static pressure

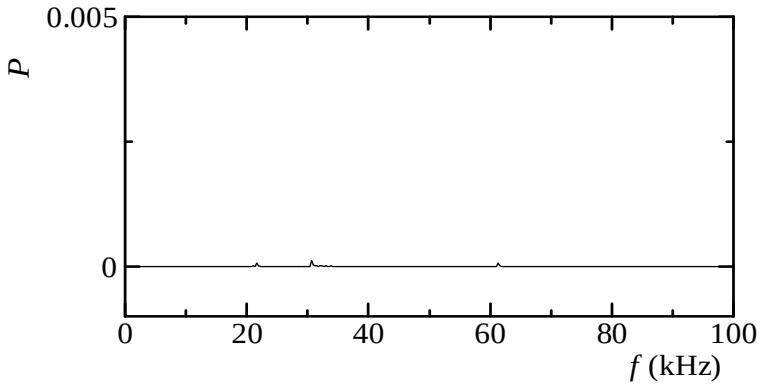

(a) Case 2

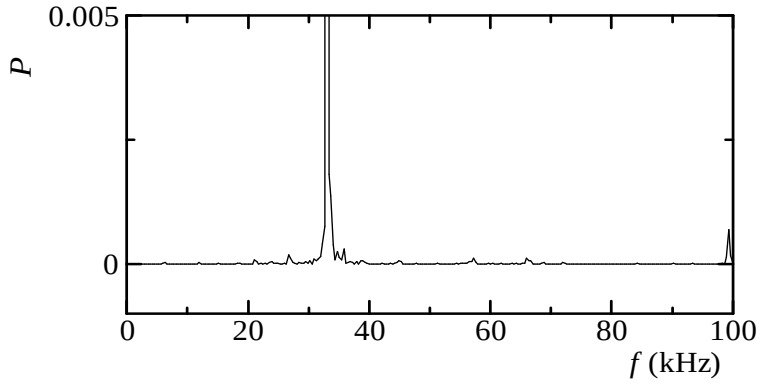

(b) Case 3

Figure 7.7: Distributions of power spectrum density

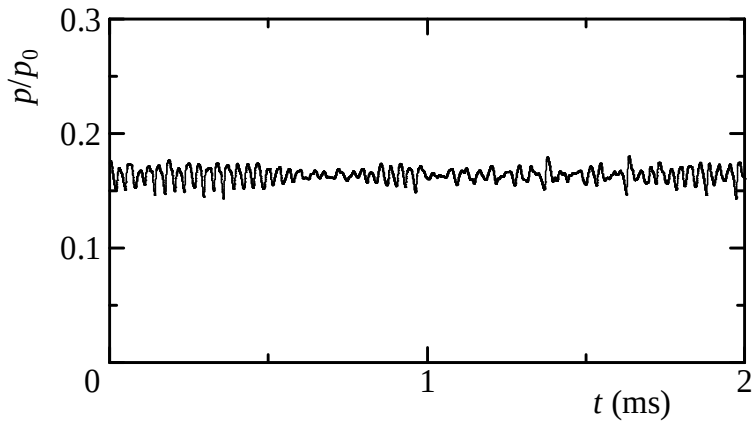

(a) Case 4

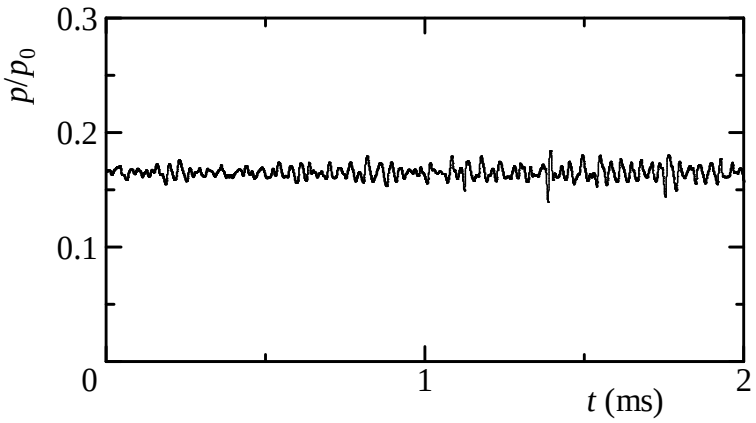

(b) Case 5

Figure 7.8: Time histories of static pressure

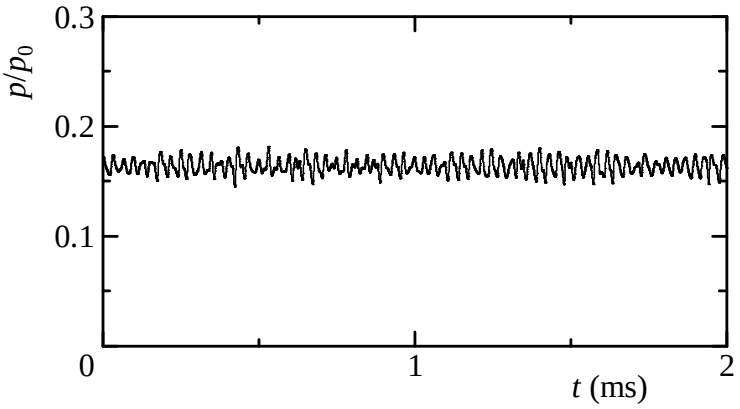

(a) Case 6

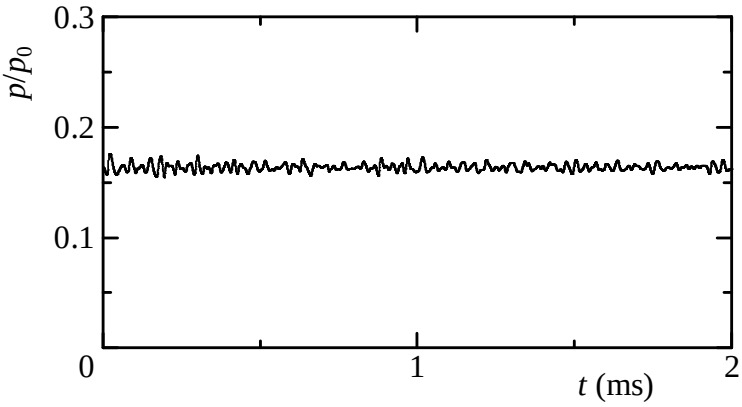

(b) Case 7

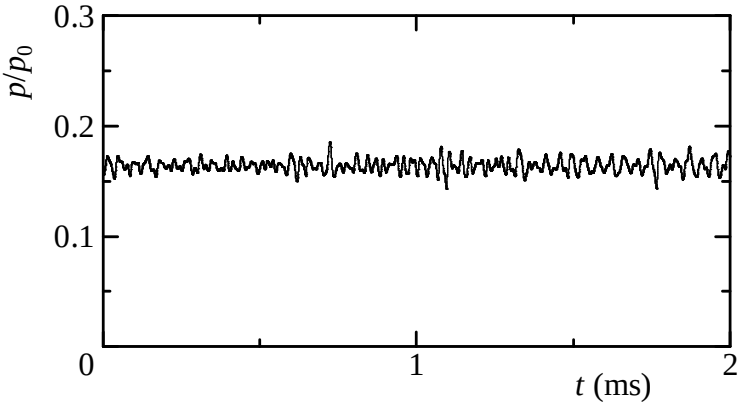

(c) Case 8

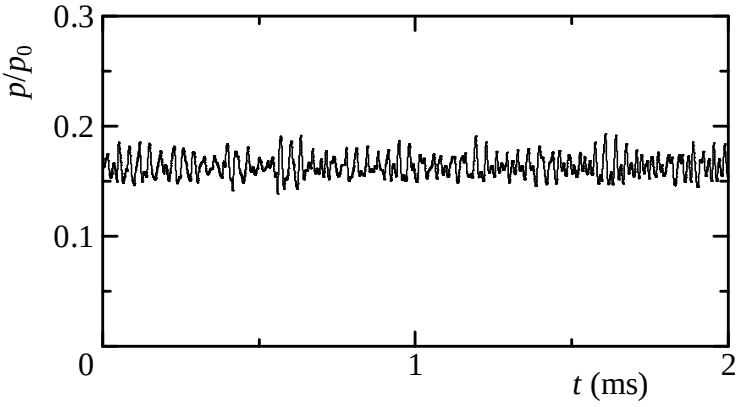

(d) Case 9

Figure 7.9: Time histories of static pressure

7.3 Effect of porous wall on the flowfield of rectangular cavities

Figure 6.18(a) shows the time history of static pressure at the position S1 inside the cavity for case with a rectangular cavity (length to depth ratio = 2) without control. There exist large amplitudes of oscillations at the position S1 as shown in Fig.6.18(a). Distribution of power spectrum density obtained from the static pressure history is shown in Fig.6.18(b). There are peak frequencies in case of cavity without control.

Figure 7.10(a) shows the time history of static pressure at the rectangular cavity with control. A reduction of the amplitudes was obtained when a flat plate is introduced in the cavity (when l/D = -0.50, t/D = 0.05, d/D = 1.0, and L/D = 2.0) Distribution of power spectrum density at the same rectangular obtained from the static pressure histories is shown in Fig.7.10(b). There are peak frequencies for case with control as shown in the Fig.7.10(b) (when l/D = -0.50, t/D = 0.05, d/D = 1.0, and L/D = 2.0).

Figure 6.20(a) shows the time history of static pressure at the position S1 inside the cavity for case with a rectangular cavity (length to depth ratio = 3) without control. There exist large amplitudes of oscillations at the position S1 as shown in Fig.6.20(a). Distribution of power spectrum density obtained from the static pressure history is shown in Fig.6.20(b). There is a dominant frequency at 8 kHz in case of cavity without control.

Figure 7.11(a) shows the time history of static pressure at the rectangular cavity with control. A reduction of the amplitudes was obtained when a flat plate is introduced in the cavity (when l/D = -0.75, t/D = 0.05, d/D = 1.0, and L/D = 3.0) Distribution of power spectrum density at the same rectangular obtained from the static pressure histories is shown in Fig.7.11(b). There are peak frequencies for case with control as shown in the Fig.7.11(b) (when l/D = -0.75, t/D = 0.05, d/D = 1.0, and L/D = 3.0).

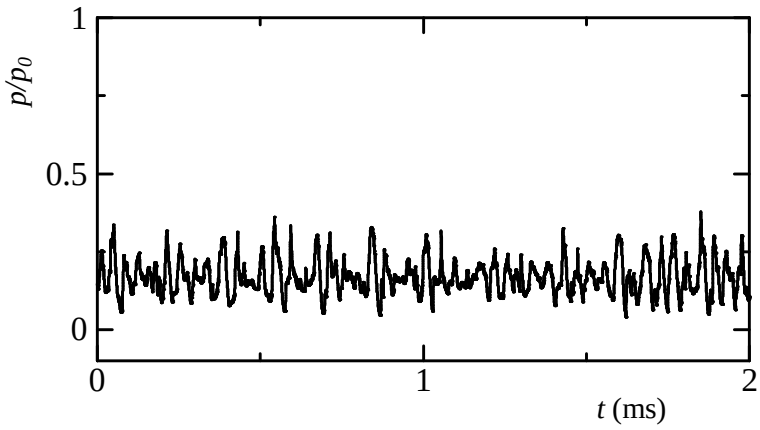

(a) Time history of static pressure

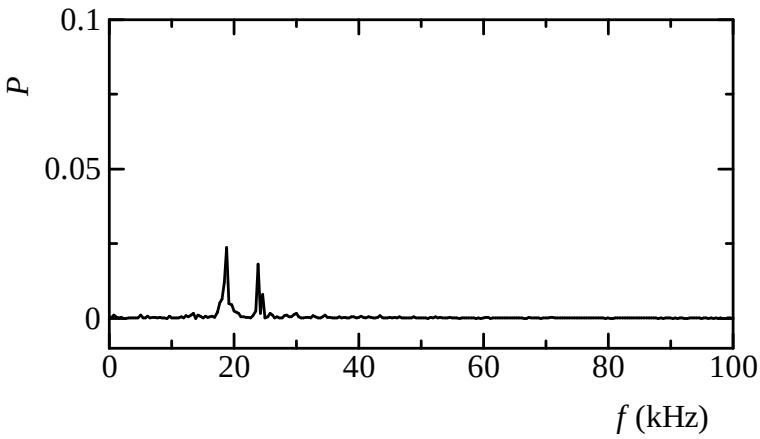

(b) Distribution of power spectrum density

Figure 7.10: Time history of static pressure and distribution of power spectrum density (l/D = -0.25, t/D = 0.05, d/D = 1.0, and L/D = 2.0)

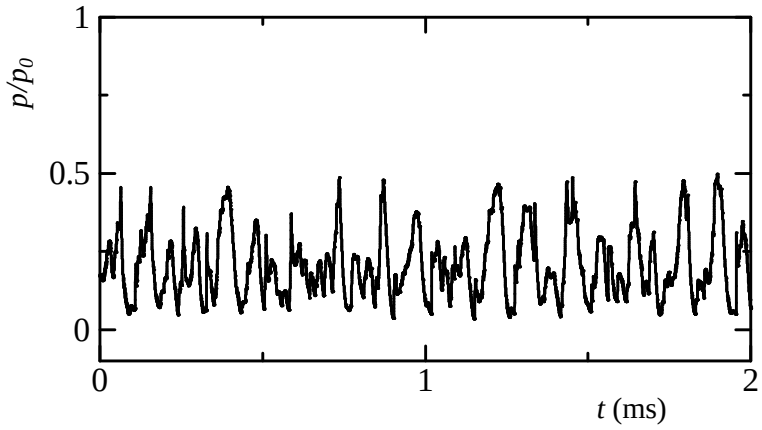

(a) Time history of static pressure

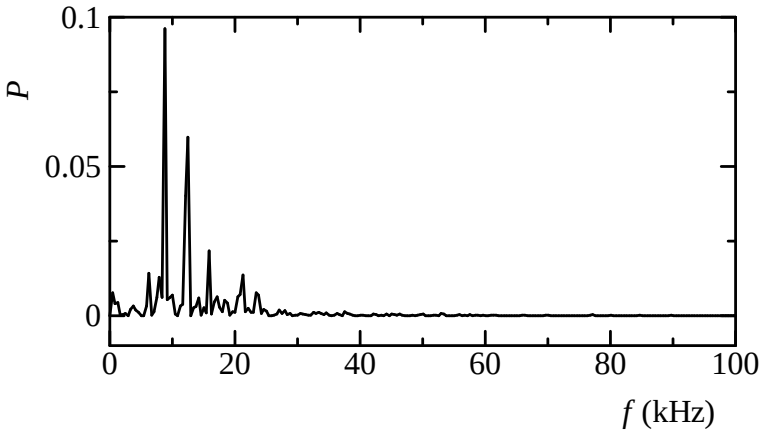

(b) Distribution of power spectrum density

Figure 7.11: Time history of static pressure and distribution of power spectrum density (l/D = -0.25, t/D = 0.05, d/D = 1.0, and L/D = 3.0)

7.4 Summary

Numerical simulations have been carried out for a supersonic two-dimensional flow over open, square cavities at Mach number 1.83 at the cavity entrance. A sub-cavity with a porous wall near the leading edge wall of the cavity covered by a flat plate had been investigated for the effectiveness of controlling the cavity induced pressure fluctuations. A self-sustaining feed-back loop and high pressure oscillations were observed in the cavity without control. The simulation results of controlled cavity showed that the sub-cavity with the porous wall is effective in reducing the

oscillations. The results also showed that the length of the leading edge plate and sub-cavity, porosity, the size of perforation of the porous wall had an influence in controlling the oscillations.

CHAPTER 8
EFFECT OF SPHERICAL SURFACE ON THE OSCILLATIONS

8.1 Conditions of numerical simulations

Figure 8.1 shows computational domain of a supersonic flow field with a cavity. The height of the main flow section at the entrance of the cavity is 24 mm. The cavity depth D (=12 mm) and its length W are the same. S1 in this figure denotes the measuring position of static pres-sure. The parameters of cavity configuration are summarized in Table 8.1. Since a spherical reflector [95] is effective in reducing sound pressure, the cavity front wall is replaced by a spherical surface in order to investigate its effect on flowfield oscillations. The radius of curvature of spherical surface and the length of leading edge plate are R and L, respectively. The number of grids is 300×80 in the region of the nozzle and 50×60 in the cavity. The origin in x-y coordinate is located at the cavity leading edge. Dry air is used as a working gas and assumed to be thermally and calorically perfect. Pressure p_0 in the reservoir is 101.3 kPa. The inlet Mach number M at the en-trance of the cavity is 1.83. On the solid walls, the no-slip conditions and no heat transfers were applied as the boundary conditions. Fixed conditions were set for the inflow boundary condition. Zero order extrapolation was used at the outflow boundary.

Table 8.1: Cavity configuration

Parameters	L/D	R/D
Without control	0	-
Case 1	0.25	1.93
Case 2	0.125	2.754

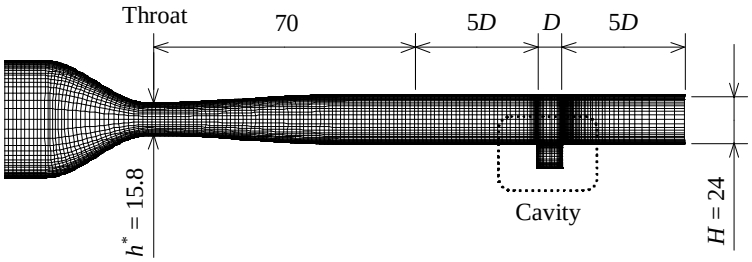

(a) Computational grids (Unit : mm)

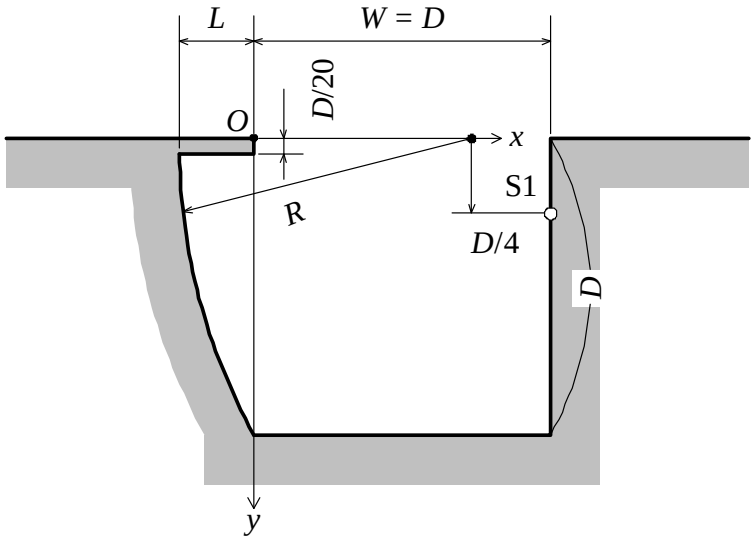

(b) Details of cavity configuration

Figure 8.1: Computational domain

8.2 Analysis of simulation data

8.2.1 Cavity without control

Figure 6.2(a) shows the time history of static pressure at the position S1 inside the cavity for case with a cavity (length to depth ratio = 1) without control. There exist large amplitudes of oscillations at the position S1 as shown in Fig.6.2(a). Distribution of power spectrum density obtained from the static pressure history is shown in Fig.6.2(b). There is a dominant frequency at 17.5 kHz in case of cavity without control.

Figure 6.3 shows contour maps of density during one period of flowfield oscillation for the cavity without control. Here, f represents the dominant frequency, which is equal to 17.5 kHz (see Fig.6.2(b)). It was observed that a compression wave (CW) from the trailing edge of the cavity moves upstream as time proceeds. The compression wave in Fig.6.3(i) converts into an upstream traveling compression waves (CW' shown in Fig.6.3(a)). The upstream compression waves impinge on the cavity leading edge and disturb the shear layer (Fig.6.3 (g)). This disturbance regenerates instability waves in the shear layer. While the shear layer reattaches at the rear wall of the cavity, generation of compression waves (CW) occurs due to the impingement of instability waves on the wall as shown in Fig.6.3(a). These compression waves propagate upstream within the cavity and further disturb the shear layer. The shear layer is continuously modified due to these subsequent disturbances and finally resonance occurs when frequency and the phase of the acoustic waves match with those of the shear layer instability waves.

Figure 6.4 shows a sequence of representative instantaneous streamline contours resulting from the cavity without control. There is a very good inclination to develop a single, large vortex in the cavity accompanied by some small vortices in the corner [2]. Furthermore, the shedding of vortices from the leading edge corner [31, 88] is also observed in the cavity without control such that the vortices at the leading edge corner (Figs. 6.4(a) and 6.4(b)) are shedding on the subsequent events (Figs. 6.4(c) through 6.4(f)) increases the instability of shear layer. Figures 6.4(g) through 6.4(i) show the development of another small vortex at the leading edge corner of the cavity.

8.2.2 Effect of spherical surface on flowfield oscillations

Figure 8.2(a) shows the time history of static pressure at the position S1 in the cavity for Case 1. The result shows that amplitude of oscillations is reduced remarkably when the front wall of the cavity is replaced by a spherical surface. Distribution

of power spectrum density shows that there is no peak frequency (Fig.8.2(b)).

Figure 8.3 shows contour maps of density of flow field for Case 1. It is also found from this figure that the compression wave becomes weaker when the flow is controlled by a spherical surface fitted vertically at front wall of the cavity. The weaker compression wave cannot disturb the shear layer strongly enough to regenerate the instability waves in the shear layer.

Figure 8.4 shows the streamlines of flowfield oscillations in a cavity with control (Case 1). There is a stable shear layer and there is a strong tendency to establish a single, large vortex in the cavity accompanied by some small vortices in the corner in the same manner as the results of Case 1.

Figure 8.5 shows time history of static pressure and power spectrum density for Case 2. The amplitude showed a similar tendency compared with that of the cavity without control and power spectrum density showed some small peak frequencies.

The placement of the spherical surface at the cavity front wall shifted the position of image source [95, 92] and minimized the sound pressure in such a way that the weak sound pressure could not excite the shear layer to regenerate the instability. Thus the formation of feedback loop was discouraged and the oscillations are minimized.

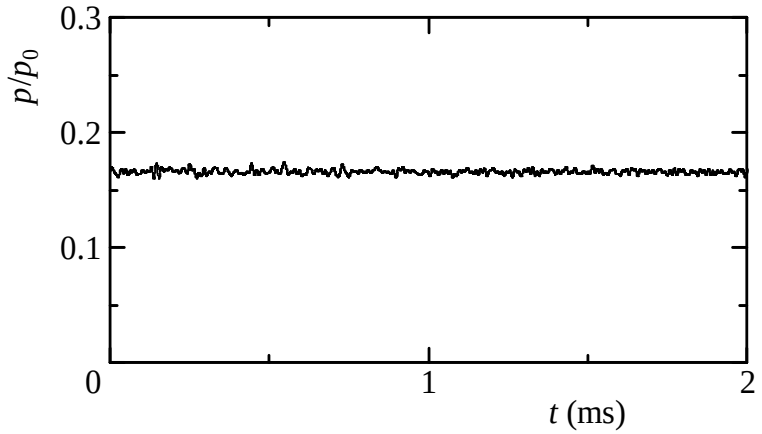

(a) Time history of static pressure

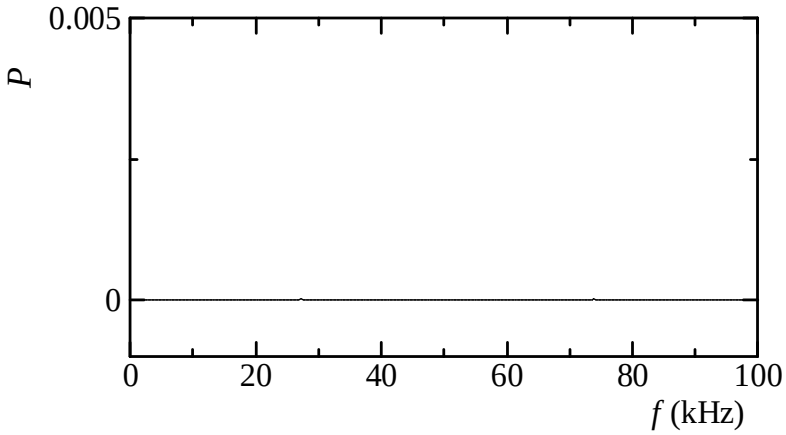

(b) Distribution of power spectrum density

Figure 8.2: Time history of static pressure and distribution of power spectrum density (Case 1)

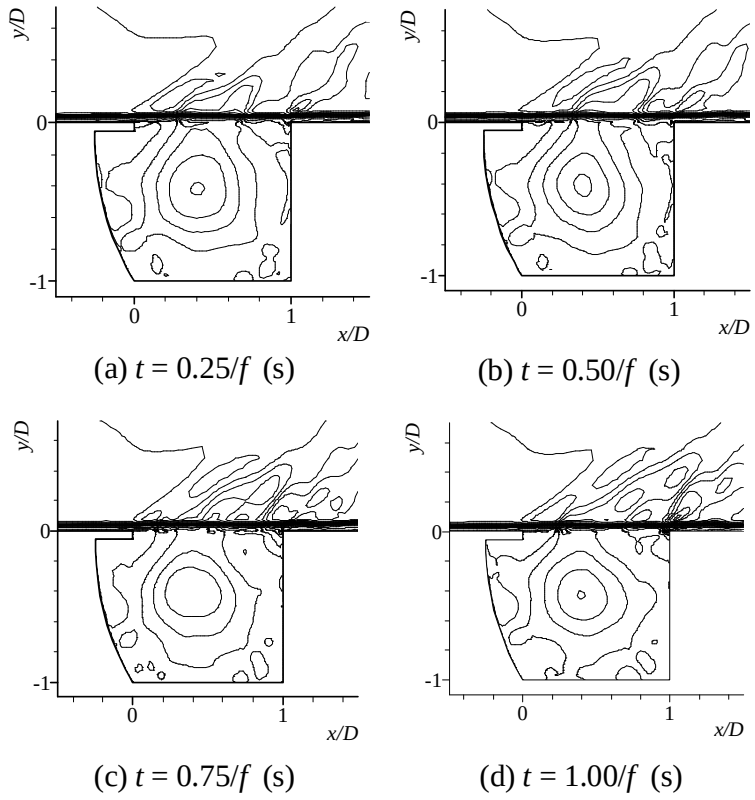

Figure 8.3: Contour maps of density showing the flowfield (Case 1)

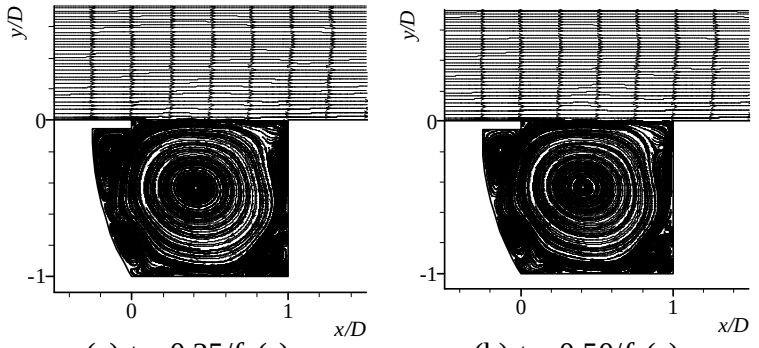

(a) $t = 0.25/f$ (s) (b) $t = 0.50/f$ (s)

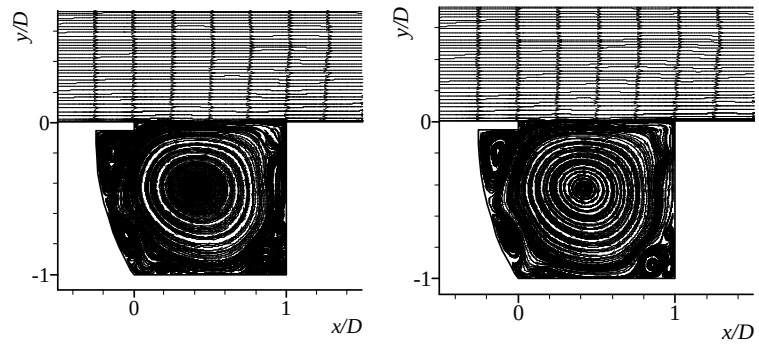

(c) $t = 0.75/f$ (s) (d) $t = 1.00/f$ (s)

Figure 8.4: Streamline (Case 1)

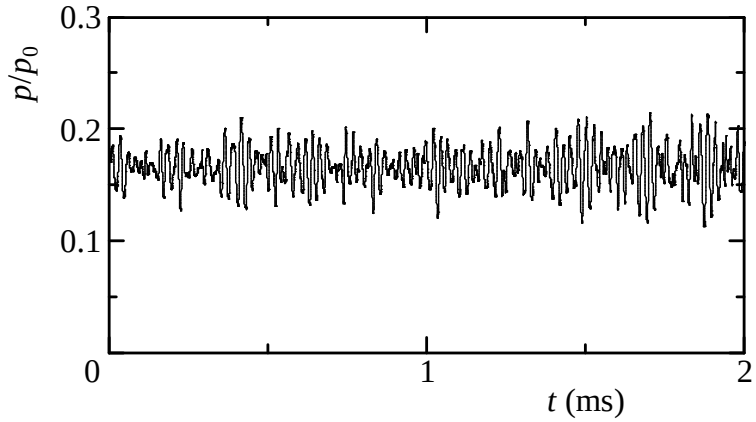

(a) Time history of static pressure

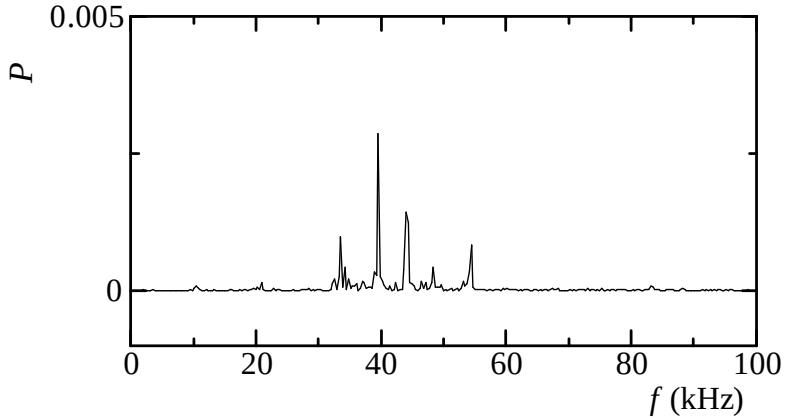

(b) Distribution of power spectrum density

Figure 8.5: Time history of static pressure and distribution of power spectrum density (Case 2)

8.3 Summary

A computational study has been carried out for a supersonic two-dimensional flow over open, square cavities at Mach number 1.83 at the cavity entrance. The front wall of the cavity has been modified with spherical surfaces to suppress the oscillations in a supersonic free stream flow. The results showed that the introduction spherical surfaces in the cavity changed the flow field in a favorable way such that the upstream compression waves became weaker and the disturbance of the shear layer by the reflected compression waves was not strong enough to regenerate the instability waves to sustain the process by completing the feedback loop.

CHAPTER 9
EFFECT OF NON-EQUILIBRIUM CONDENSATION ON THE OSCILLATIONS

9.1 Introduction

Supersonic cavity flow fields are often characterized by shock waves, expansion waves, shear layer and an oscillation inside the cavity. Many researches have been conducted over the past decades to investigate the supersonic external flows over the cavity [102, 103, 41, 49]. In recent years, researches for the supersonic internal flows around a cavity have been conducted in relation to a supersonic air-intake that is a component of an air breathing engine. The cavity plays an important role in the control of shock wave [104]. The supersonic air-intake flow tends to be unstable due to the separations induced by the shock wave / boundary layer or the shock wave / shear layer interactions [104, 105].

In supersonic internal flows past cavities, a non-equilibrium condensation may occur in the region where vapour is contained in the main flow. Many studies on the condensation occurring in the case of the rapid expansion of moist air or steam in a supersonic nozzle have been performed experimentally and numerically [106, 107, 108], and the characteristics of condensation have been nearly clarified. However, the effect of non-equilibrium condensation on the supersonic internal flows around the cavity has not yet been clarified satisfactorily.

In the present study, a condensing flow was produced by an expansion of moist air in a Laval nozzle, and the effect of non-equilibrium condensation on the supersonic internal flows around the cavity is clarified numerically.

9.2 Conditions of numerical simulations

Assumptions made in the present simulation of the two phase flow are as follows ; Both velocity slip and temperature difference do not exist between condensate particles and gas mixture, and the effect of the condensate particles on pressure is neglected. The governing equations used in the present simulation were the unsteady compressible Navier-Stokes equations and a rate of liquid-phase production [67] in a two-dimensional coordinate system. Latent heat, nucleation rate, critical radius of the nuclei, radius growth rate, density of liquid phase and surface tension

have already been described in Chapter 3. The governing equations are given in Chapter 4.

Figure 9.1 shows computational domain of a supersonic flow field with a cavity. The height H of the main flow section at the entrance of the cavity is 24 mm. The cavity depth D is fixed at 12 mm and the lengths L are 12 mm and 36 mm. S1, S2, and S3 in this figure denote the measuring positions of static pressure.

The number of grids in the nozzle is 300×80. The number of grids in the cavity is 50×60. The origin in $x - y$ coordinate is located at the corner of the cavity leading edge. In the present study, moist air is used as a working gas and assumed to be thermally and calorically perfect. The oncoming boundary layer is laminar. Pressure p_0 and temperature T_0 in the reservoir are 101.3 kPa and 298 K, respectively. Values of the initial degree of supersaturation S_0 (the ratio of the vapor pressure to the saturated vapor pressure) are 0 and 0.6. The inlet Mach number at the entrance of the cavity is 1.83. Non-slip velocity and no heat transfer are constrained on the solid wall. Fixed condition is used at the inflow boundary and zero order extrapolation is used at the outflow boundary. Condensate mass fraction $g = 0$ is set at the wall.

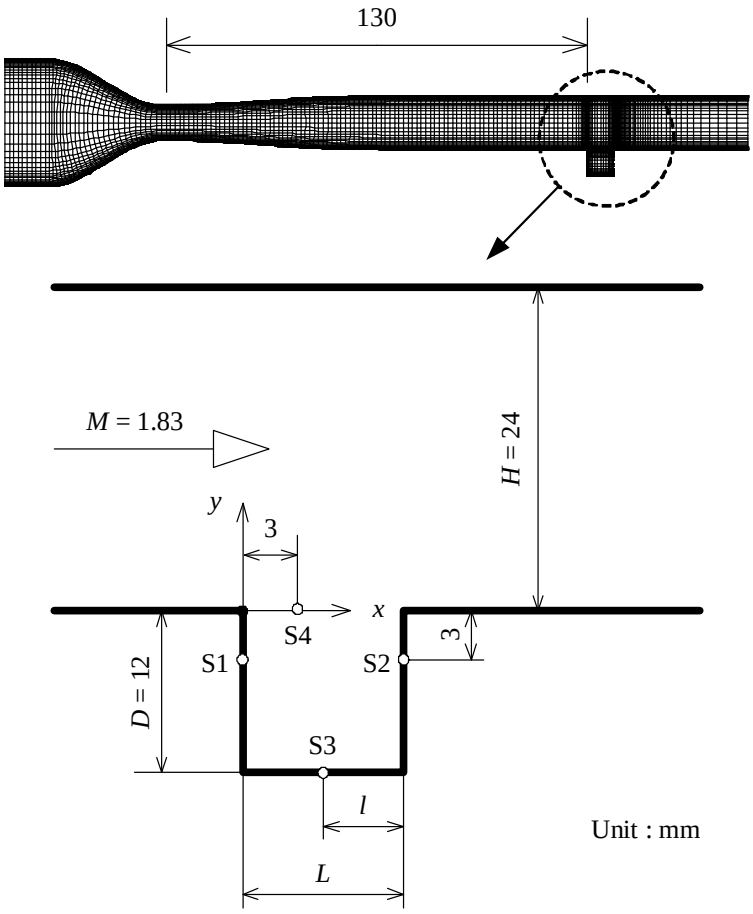

Figure 9.1: Computational domain.

9.3 Analysis of simulation data

9.3.1 Flowfield oscillation without condensation

In order to determine the effect of non-equilibrium condensation on supersonic internal flows around the cavity, first of all, observations were made with a cavity for case without condensation. Figure 9.2 shows static pressure histories at positions of S1, S2 and S3 in case of $S_0 = 0$. It is found from these figure that amplitudes of oscillation are almost the same at three positions. Distributions of power spectrum density obtained from static pressure histories are shown in Fig.9.3 and there is a dominant frequency at 17.5 kHz in case of $S_0 = 0$.

9.3.2 Effect of non-equilibrium condensation on the flowfield oscillation

Figure 9.4 shows static pressure histories at each position for $S_0 = 0.6$. In this case, amplitudes of oscillation are smaller than those without the non-equilibrium condensation.

Figure 9.5 shows distributions of power spectrum density at each position for $S_0 = 0.6$. There is a strong peak at 51.1 kHz in contrast to the case of $S_0 = 0$. Furthermore, the peak value of power spectrum for the dominant frequency becomes small in comparison with the case of $S_0 = 0$. It is found from this result that the non-equilibrium condensation affects strongly the oscillation in the flow field.

Figure 9.6 shows contour maps of density during one period of flow oscillation for $S_0 = 0$ (L/D=1.0). f_{nc1} and f_{wc1} are frequencies in cases of no condensation and the occurrence of condensation, respectively. In Fig.9.6 ($S_0 = 0$), a compression wave (CW) from the trailing edge of the cavity moves upstream as time proceeds. The compression wave CW in Fig.9.6(i) becomes an upstream travelling compression wave (CW !Gshown in Fig.9.6(a)). The upstream travelling compression wave CW !Greaches the front of the cavity (Fig.9.6(g)). Hence the shear layer is largely deflected by the compression wave and the instability of the shear layer regenerates the following compression wave (CW) as shown in Fig.9.6(a).

Figure 9.7 shows contour maps of density during one period of flow oscillation for $S_0 = 0.6$. In Fig.9.7 ($S_0 = 0.6$), a compression wave (CW) from the trailing edge of the cavity moves upstream as time proceeds. However, the strength seems to be weak in comparison with one in Fig.9.6. This is considered to be due to the occurrence of non-equilibrium condensation at the region close to the trailing edge. Furthermore, deflection of the shear layer waveform becomes small in comparison

with that in Fig.9.6.

Figures 9.8 shows contour maps of nucleation rate I during one period of flow oscillation corresponding to Figs.9.7. It is found from these figure that condensate nuclei are mainly generated in the main flow above the trailing edge. This means that latent heat is released by the non-equilibrium condensation. It is considered that the generation of condensate nuclei in the main flow above the trailing edge slows down the velocity of main flow. This consideration agrees well with the observation that the flow Mach number decreased by approximately 7.1 percent (M=1.70) and total pressure loss was 4.0 percent at the position of x/D =-5.0 in case of the non-equilibrium condensation (S_0 =0.6). This makes the difference of velocity between the upper and lower sides of the shear layer small and the instability of the share layer is reduced effectively. This weaker instability waves, when impinge on the wall of cavity trailing edge side, produces weaker compression waves. These compression waves cannot disturb the shear layer strongly enough to regenerate strong instability waves and thus the amplitude of oscillations reduces effectively as shown in Fig.9.4.

Figure 9.9 shows distributions of u (velocity component of x-direction) on the line normal to x-axis at the position of $x/D = 0.9$ for $S_0 = 0$. The velocity u is normalized using sound speed a_0 in the reservoir.

Figure 9.10 shows distributions of u (velocity component of x-direction) on the line normal to x-axis at the position of $x/D = 0.6$. In case of $S_0 = 0.6$, it is found that the velocity in main flow is small in comparison with the case of $S_0 = 0$. This is due to the occurrence of the non-equilibrium condensation in the main flow on the trailing edge as shown in Fig.9.8. This affects strongly the difference of velocity between the upper and lower sides of the shear layer.

Figure 9.11 shows distributions of the static pressure during one period of flow oscillation on the line normal to y-axis at the position of y/D = -0.042 for $S_0 = 0$. As seen from Fig.9.11, the compression wave (CW) propagates upstream in the cavity after the generation of compression wave at the trailing edge.

Figure 9.12 shows distributions of the static pressure during one period of flow oscillation on the line normal to y-axis at the position of y/D = -0.042 for $S_0 = 0.6$. In Fig.9.12, the compression wave propagates in the same manner as that for $S_0 = 0$. However, the strength seem to be weak in comparison with that for $S_0 = 0$.

Figure 9.13 shows variations of strength (p_2/p_1) of compression wave propagating upstream in the cavity obtained from results of Figs.9.11 and 9.12. From this figure, the strength in case of $S_0 = 0.6$ becomes weak as the wave propagates upstream in the cavity in comparison with the case of $S_0 = 0$.

It is considered that some peaks in the region of low frequency in Figs.9.3 is due to the strong interaction of the shear layer with the cavity that leads to the large deflection of the shear layer waveform as shown in Fig.9.6. In case with the peak in the region of high frequency that is 51.1 kHz in Fig.9.5, the strength of the compression wave in the cavity becomes weak as shown in Figs.9.12 and 9.13. This means the weak interaction of the shear layer with the cavity and the oscillation is dominated by the shear layer itself.

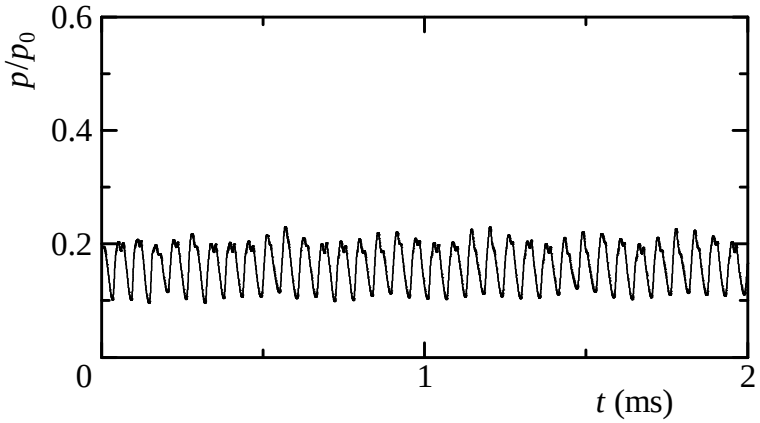

(a) S1

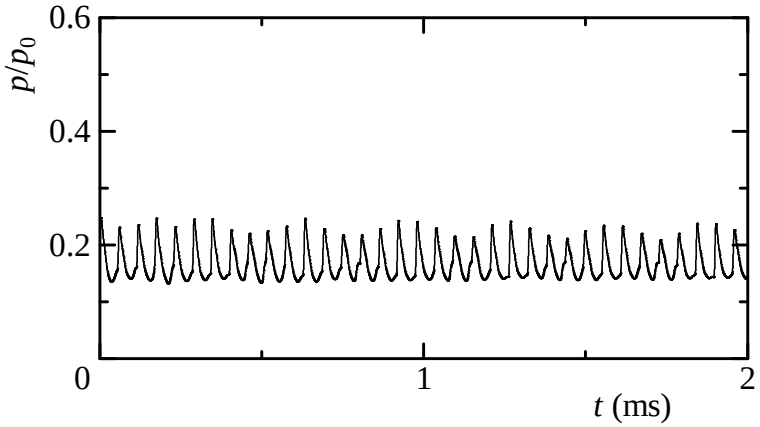

(b) S2

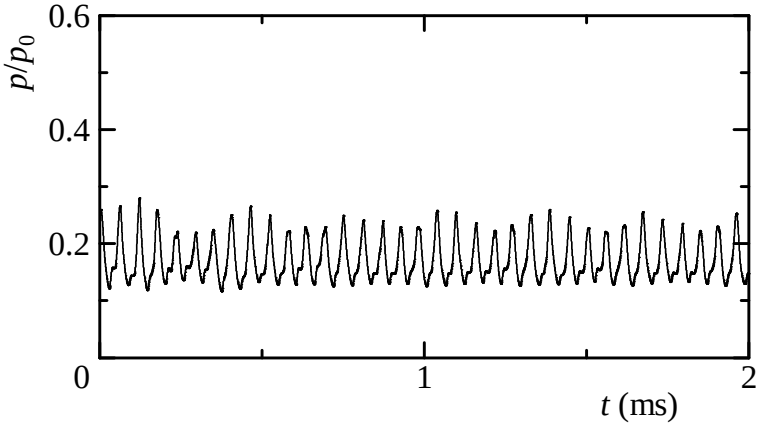

(c) S3

Figure 9.2: Time histories of static pressure ($S_0 = 0$).

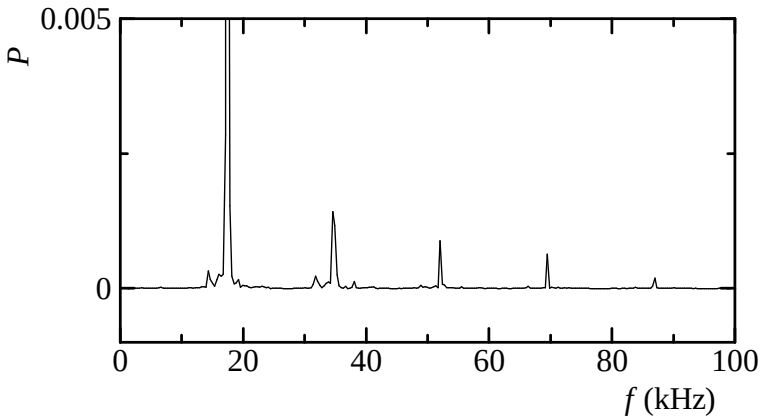

(a) S1

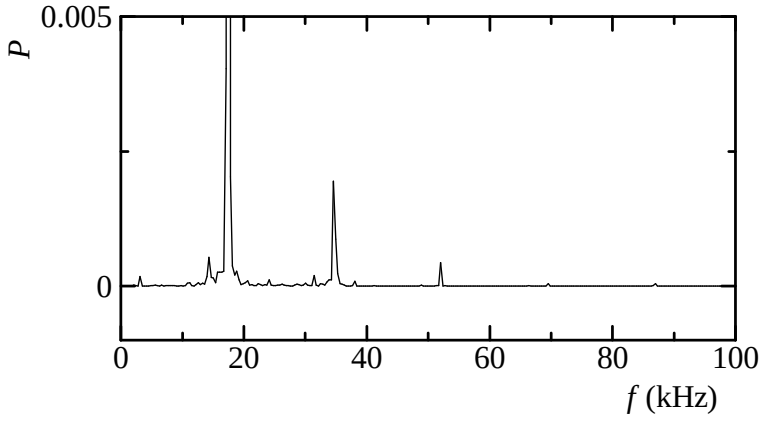

(b) S2

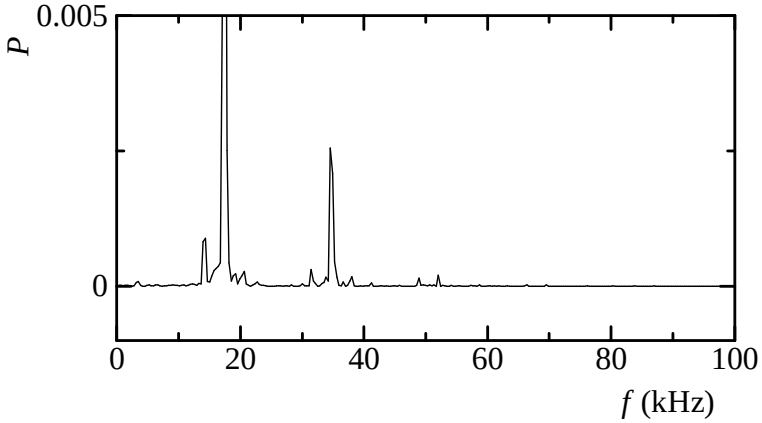

(c) S3

Figure 9.3: Distributions of power spectrum densities ($S_0 = 0$).

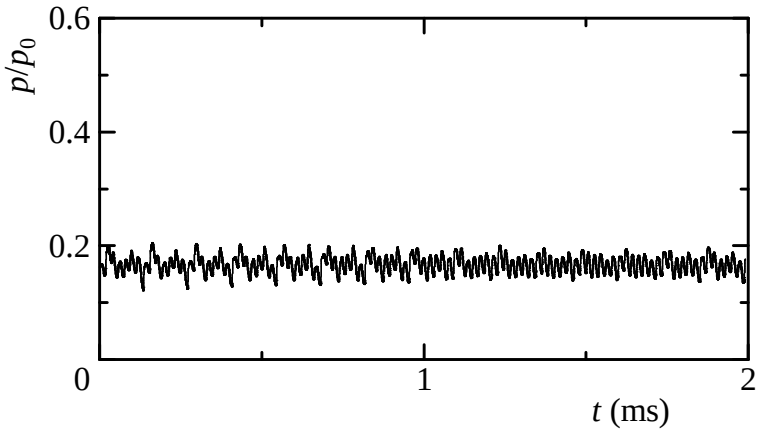

(a) S1

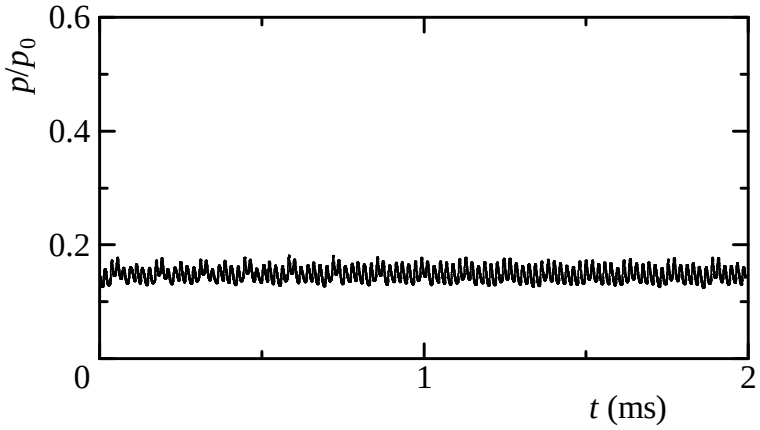

(b) S2

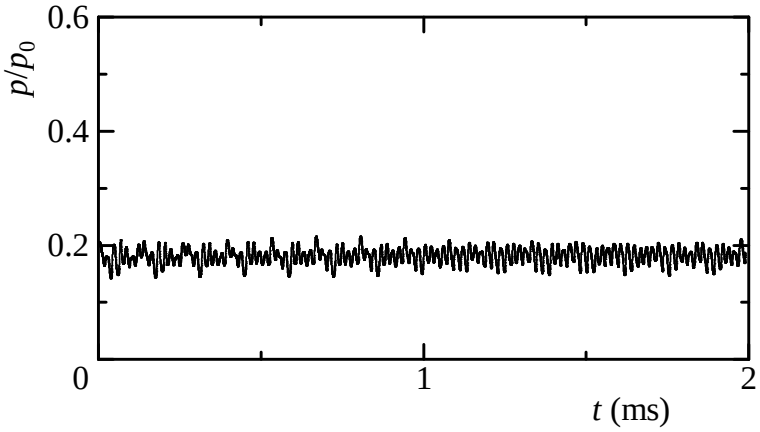

(c) S3

Figure 9.4: Time histories of static pressure ($S_0 = 0.6$).

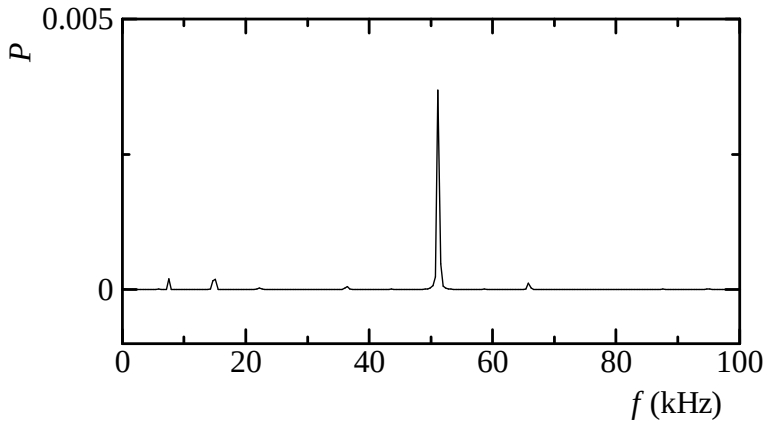

(a) S1

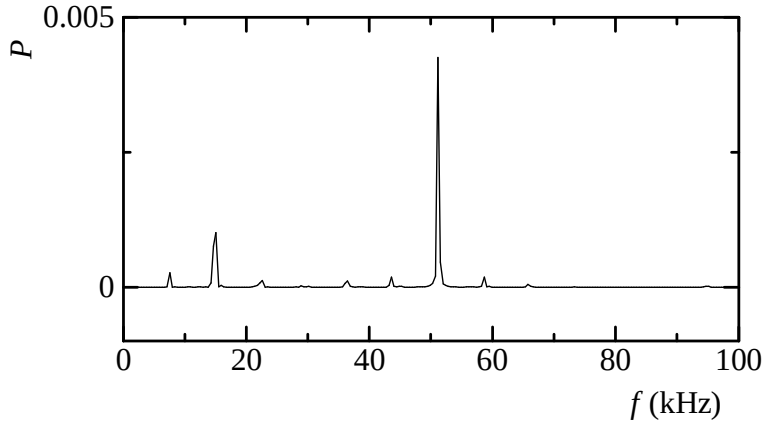

(b) S2

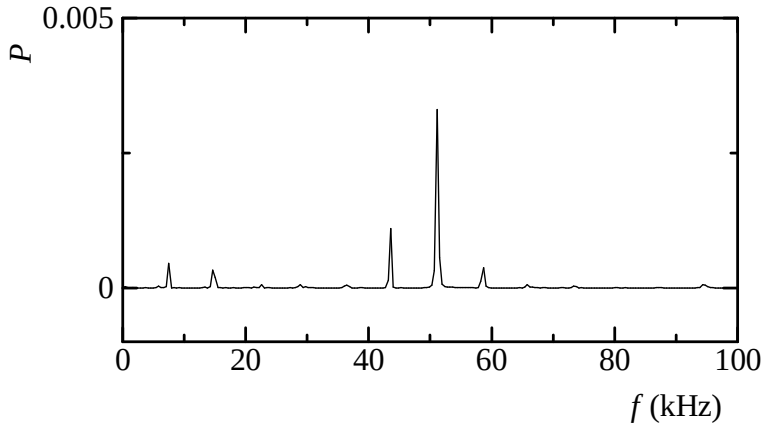

(c) S3

Figure 9.5: Distributions of power spectrum densities ($S_0 = 0.6$).

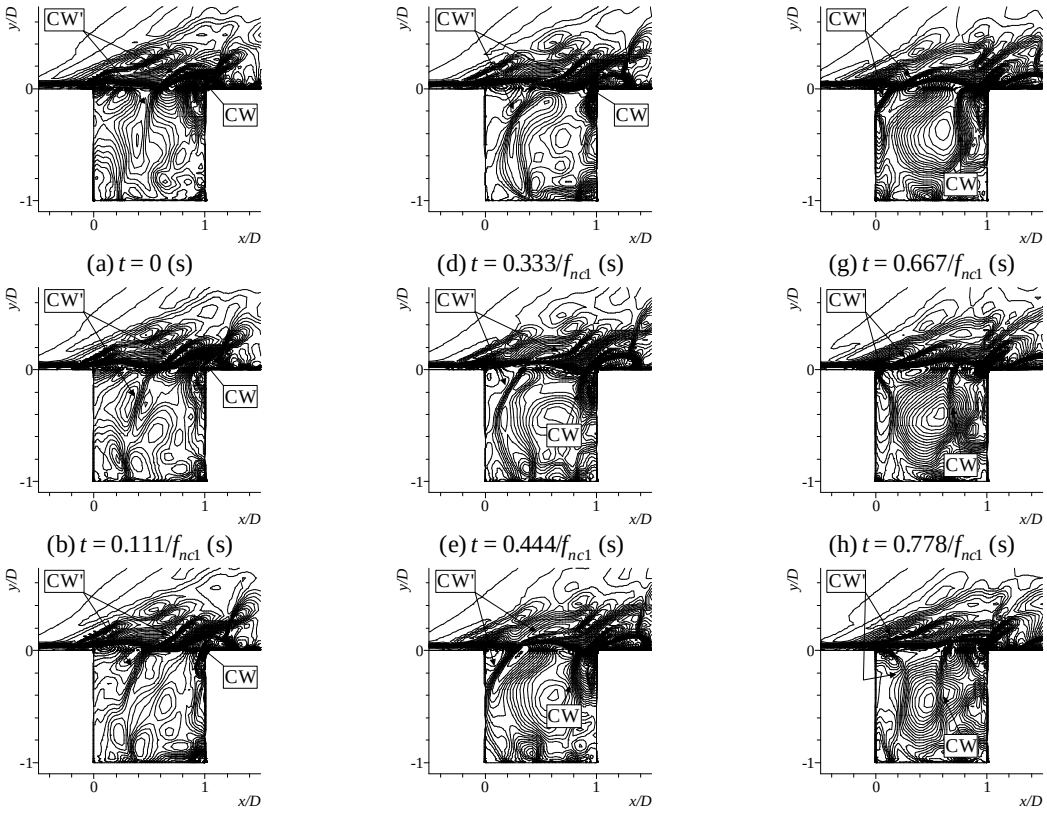

Figure 9.6: Contour maps of density showing flowfield oscillation ($S_0 = 0$).

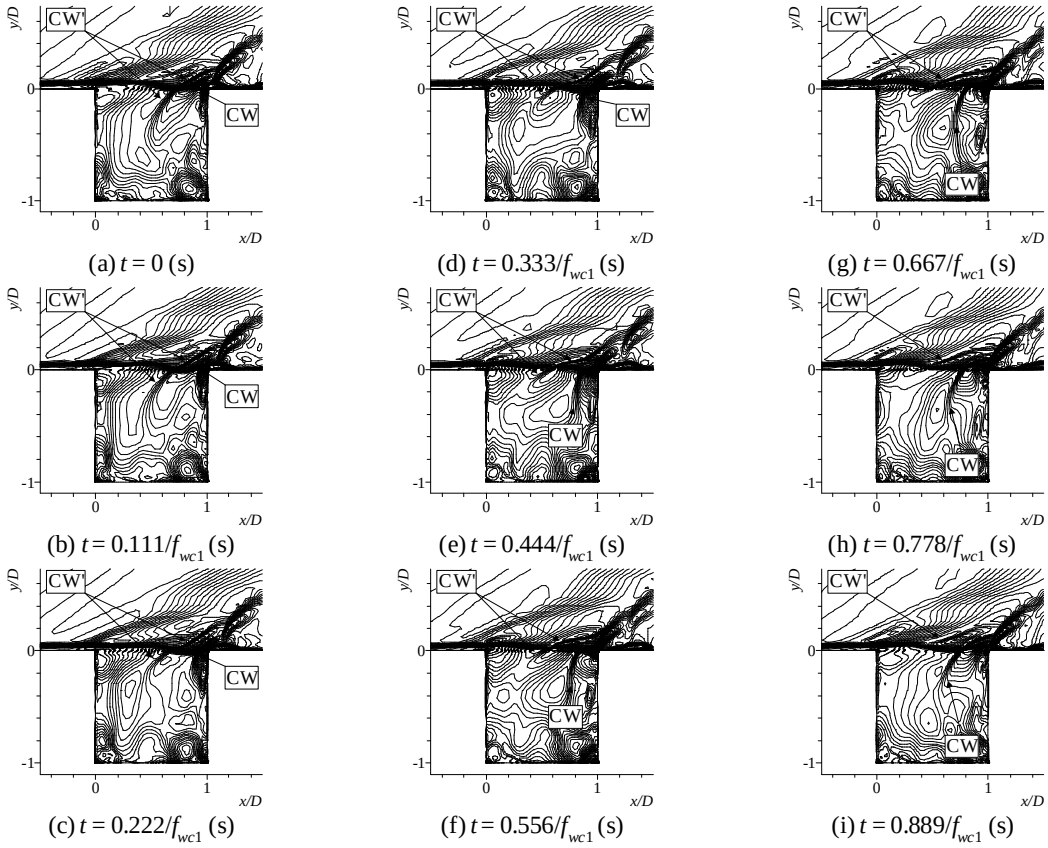

Figure 9.7: Contour maps of density showing flowfield oscillation ($S_0 = 0.6$).

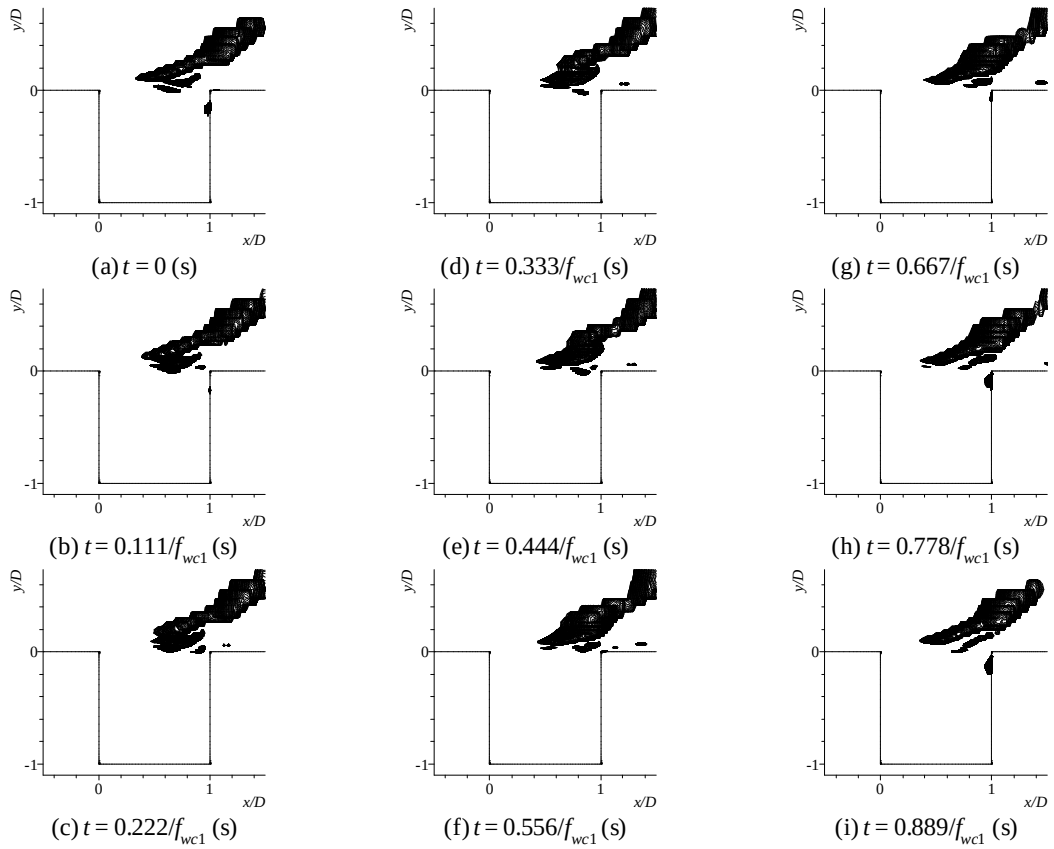

Figure 9.8: Contour maps of nucleation rate during one period of flowfield oscillation ($S_0 = 0.6$).

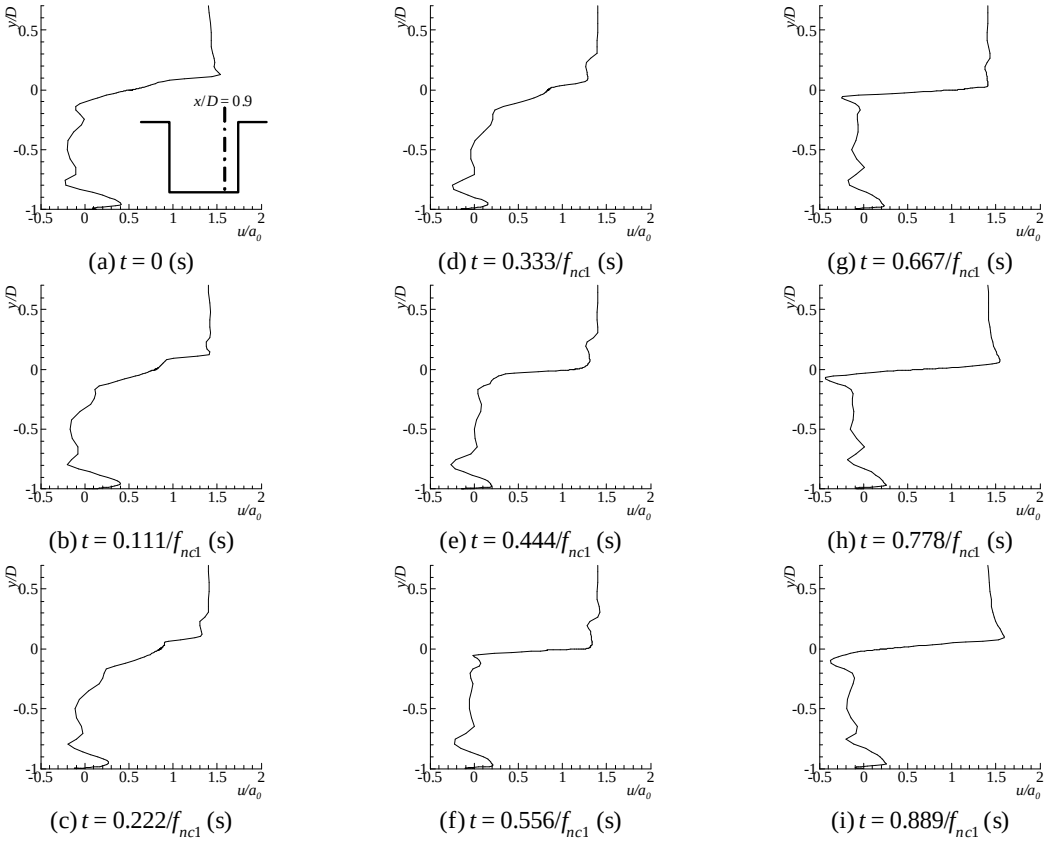

Figure 9.9: Distributions of u showing flow field oscillation ($S_0 = 0$, $x/D = 0.9$).

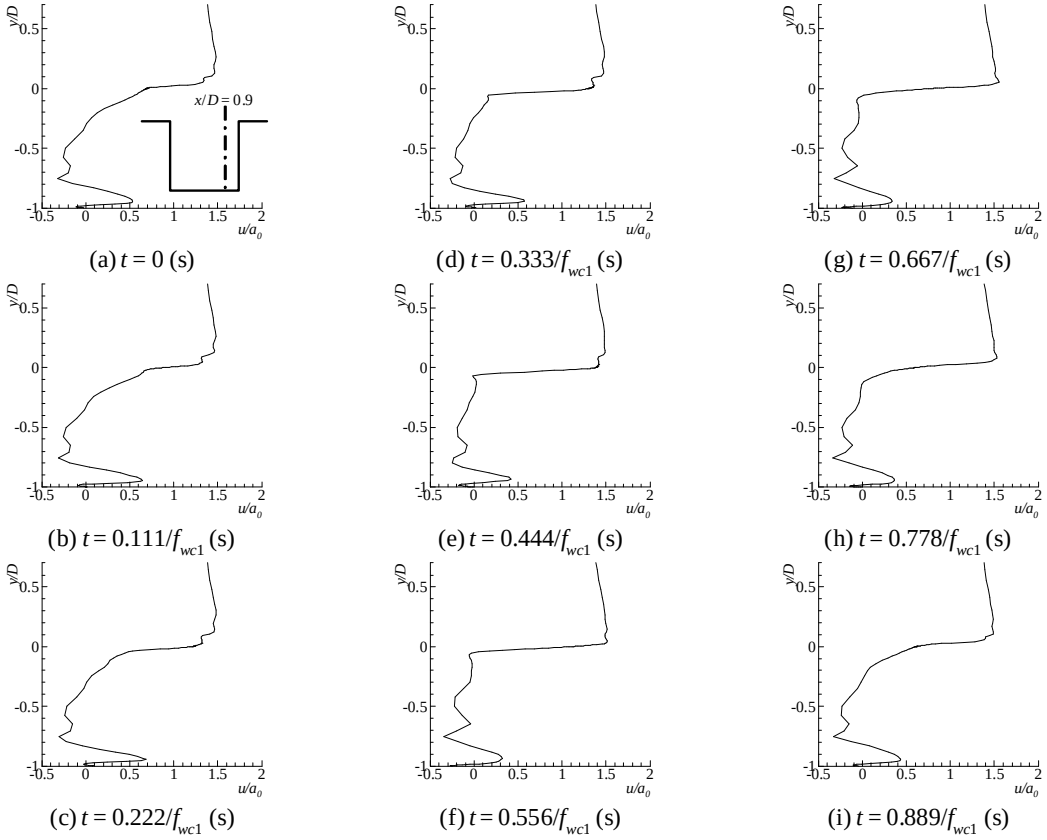

Figure 9.10: Distributions of u showing flow field oscillation ($S_0 = 0.6$, $x/D = 0.9$).

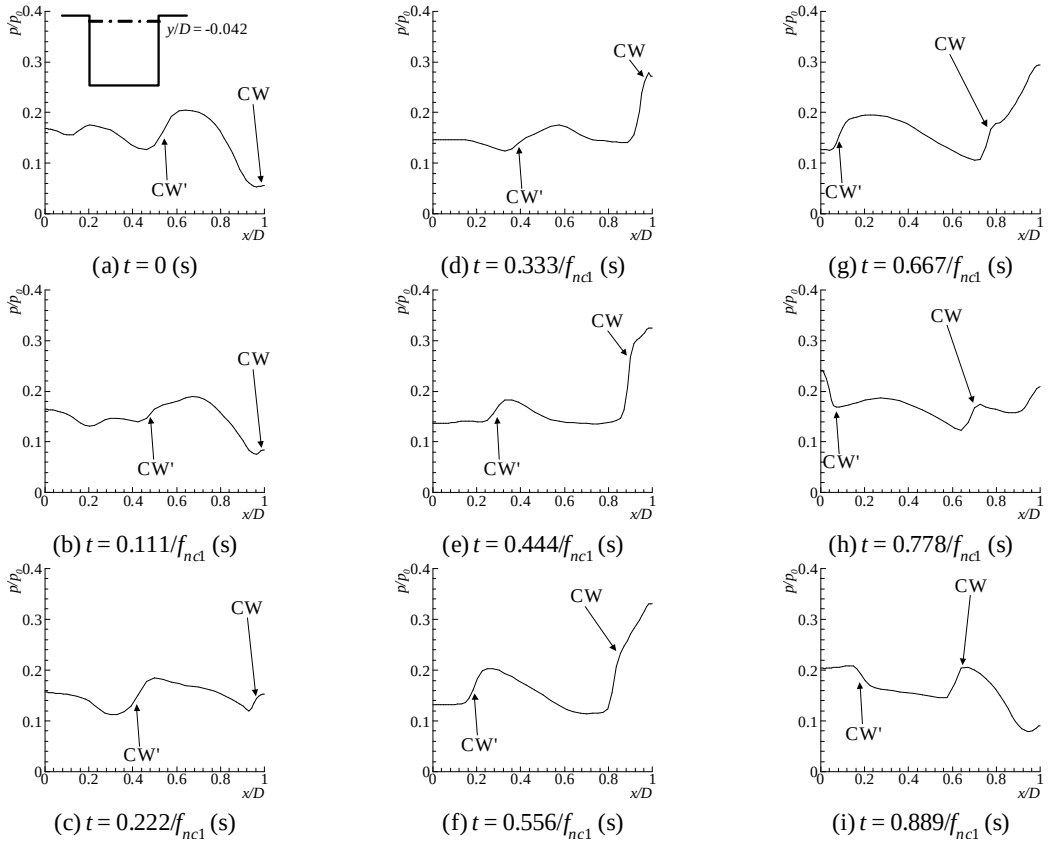

Figure 9.11: Distributions of static pressure showing flowfield oscillation ($S_0 = 0$, y/D = -0.042).

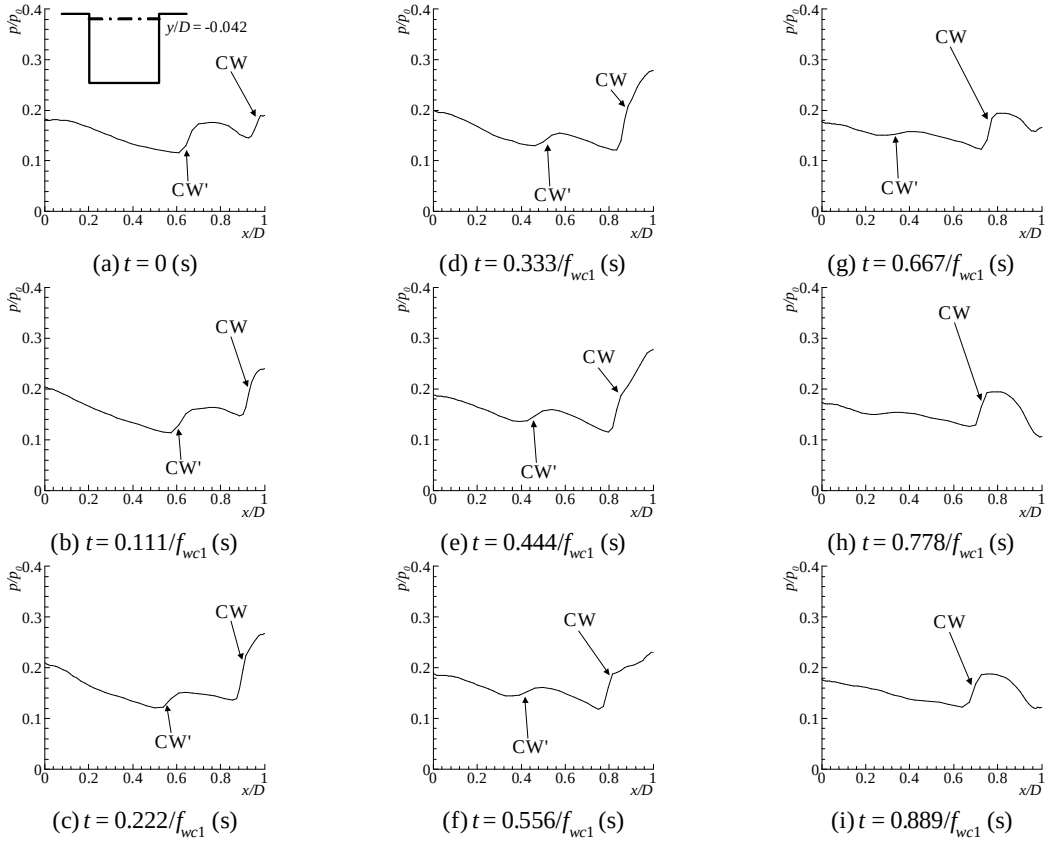

Figure 9.12: Distributions of static pressure showing flowfield oscillation ($S_0 = 0.6$, y/D = -0.042).

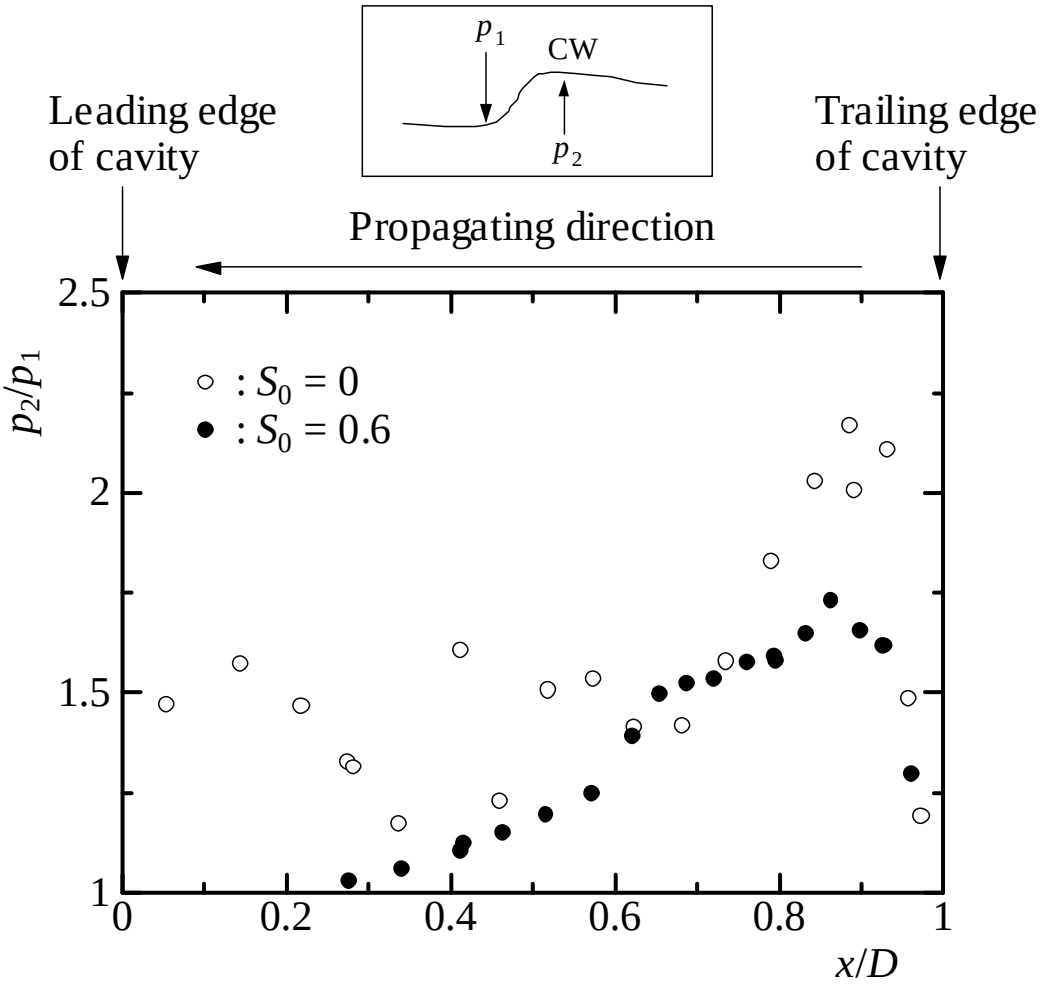

Figure 9.13: Strength of compression wave propagating upstream in cavity.

9.4 Summary

Numerical simulation was carried out for a supersonic two-dimensional internal flows over a rectangular cavity of L/D =1.0 a free stream Mach number = 1.83. The results showed that in the case with non-equilibrium condensation, amplitudes of oscillation in the cavity became smaller than those without the non-equilibrium condensation. Furthermore, the occurrence of the non-equilibrium condensation reduced the peaks of power spectrum density and the frequency of the flow field oscillation increased in comparison with the case of $S_0 = 0$.

CHAPTER 10
CONCLUSIONS

10.1 Summary

Computational and experimental investigations have been conducted to control cavity-induced pressure oscillations for a supersonic flow over open square cavities at Mach number 1.83 at the cavity entrance. A number of passive suppression techniques have been studied by modifying the front wall of a square cavity with leading edge plates, sub-cavity, porous and spherical surfaces to determine the effectiveness of controlling cavity-induced pressure oscillations.

The results of sub-cavity on the front wall of the cavity with a flat plate showed that the length and thickness of the flat plate had a great influence in controlling the cavity-induced pressure oscillations. It was observed that the introduction of a sub-cavity near the front wall of the cavity covered by a leading edge plate helped to alter the oscillating shear layer in a favorable way so that some of the undesirable effects resulting from supersonic cavity flows were eliminated. The amplitudes of the oscillations were reduced substantially with an increased of the length of the flat plate. Furthermore, a decrease in the plate thickness also assisted to suppress the oscillations remarkably. The results also showed that the resultant amount of attenuation of cavity-induced pressure oscillations was dependent on the depth of the sub-cavity.

The simulation results of cavity controlled by the sub-cavity with porous wall showed that the oscillations are reduced effectively. The results also showed that the length of the leading edge plate and sub-cavity, porosity, the size of perforation of the porous wall had an influence in controlling the oscillations.

The using of spherical surface at the front wall of a cavity changed the flow field in a favorable way such that the upstream compression waves became weaker and the disturbance of the shear layer by the reflected compression waves was not strong enough to regenerate the instability waves to sustain the process by completing the feedback loop. Furthermore, resultant amount of attenuation of oscillations was dependent on the radius of curvature of the spherical surface used as oscillation suppressors.

Numerical simulation was carried out for a supersonic internal flows over a rectangular cavity of L/D =1.0 a free stream Mach number = 1.83. The results

showed that in the case with non-equilibrium condensation, amplitudes of oscillation in the cavity became smaller than those without the non-equilibrium condensation. Furthermore, the occurrence of the non-equilibrium condensation reduced the peaks of power spectrum density and the frequency of the flow field oscillation increased in comparison with the case of $S_0 = 0$.

Experiments were conducted in order to verify the validity of calculation results. The comparisons between the present simulated and experimental results showed a fairly good agreement. The results also showed a good agreement with the experimental and theoretical results of other researchers.

10.2 Suggestions for future works

Since flow field characteristic appear to depend primarily upon the geometry of the cavity, inlet Mach number and the thickness of the boundary layer, further investigations are necessary to determine the characteristics of the proposed control devices in a changing flow environment such as changing the inlet Mach number, incoming boundary layer thickness etc. Two-dimensional numerical simulation has been conducted in the present study. However, three-dimensional simulations using Large Eddy Simulation (LES), Detached Eddy Simulation (DES) etc. are necessary in order to provide an insight into the detailed cavity flow mechanism.

APPENDIX A
EFFECT OF AXI-SYMMETRIC NOZZLE ON THE OSCILLATIONS

A.1 Introduction

It is well known that the supersonic air-intake flow tends to be unstable due to the separations induced by the shock wave /boundary layer or the shock wave/shear layer interactions [96, 97]. The flow unsteadiness associated with boundary layer separation occurs in a variety of internal flows such as in the inlets of air-breathing engines, in Scramjet engines, in supersonic diffusers [98], and also in high pressure power plants [98]. The flow unsteadiness can also occur in case of transonic flows with periodic self-excited oscillations and in case of cavities with self-excited oscillations. The oscillations should be suppressed in order to avoid many undesirable phenomena associated with oscillations such as noise and vibration.

Some passive control devices have been reported to control the flow unsteadiness associated with shock/boundary layer separations [99, 100]. McCormic [99] studied shock/boundary layer interaction control with low-profile vortex generators and passive cavity. He observed that the passive cavity could substantially reduce the total pressure loss through the shock system by causing a more isentropic compression. Asbury et al. [100] studied passive cavity concept for improving the off-design performance of fixed-geometry exhaust nozzles. They concluded that passive cavity ventilation added the ability to control off-design separation in the nozzle. Pandey et al.[101] studied annular cavities to control base flow for supersonic flow through axi-symmetric nozzle expanded suddenly into circular duct of larger cross-sectional area. They reported that the cavity aspect ratio influenced the base pressure significantly for low area ratio of the flow passage.

In the present computational study, a passive control method has been investigated for a supersonic flow at Mach number 1.83 at the entrance of a straight channel connected to an axi-symmetric nozzle. A good suppression of oscillations was obtained by the proposed control devices.

A.2 Conditions of numerical simulations

The governing equations are two-dimensional unsteady compressible Navier-Stokes equations coupled with turbulence kinetic energy and eddy viscosity equations. The turbulence model used in this simulation is a modifed $k - R$ (turbulent kinetic energy-eddy viscosity) model [77, 78, 79], which is a two-equation model applicable to both wall bounded and free shear flows. This model is also applicable to both structured and unstructured grids involving complex geometries. A third-order TVD (Total Variation Diminishing) finite difference scheme with MUSCL [73] was used to discretize the spatial derivatives and a second order central difference scheme for the viscous terms, and a second-order fractional step is employed for time integration.

Figure A.1 shows computational grids of a supersonic flow field with a cavity. The diameter of the main flow section at the entrance of the cavity d is 24 mm. The cavity depth D (=12 mm) and its length W are the same. S1, S2, S3 and S4 in this figure denote the measuring positions of static pressure. A solid surface of length $L = 3$ mm and thickness $t = 0.6$ mm which is most effective in reducing the oscillations [35] is attached at the leading edge of the cavity as shown in Fig.A.1(b). The origin in $x - y$ coordinate is located at the cavity leading edge. S1, S2, S3 and S4 in this figure denote the measuring positions of static pressure. Dry air is used as a working gas and assumed to be thermally and calorically perfect. Pressure p_0 in the reservoir is 101.3 kPa. The inlet Mach number M at the entrance of the straight channel is 1.83. On the solid walls, the no-slip conditions and no heat transfers were applied as the boundary conditions. Fixed conditions were set for the inflow boundary condition. Zero order extrapolation was used at the outflow boundary.

A.3 Analysis of simulation data

A.3.1 Flowfield oscillations without control

Figure A.2 shows time history of static pressure and power spectrum density at S1 in the cavity without control. There exist large amplitudes of oscillations at the position S1 without control in case of flow through asymmetric nozzle as shown in Fig.A.2(a). Distributions of PSD (power spectrum density) at the same position obtained from the static pressure histories are shown in Fig.A.2(b). There is a dominant frequency at 36.5 kHz in case of flow without control.

Figure A.3 shows contour maps of density during one period of flowfield oscillation in case without control. It shows sequences of events that form a typical

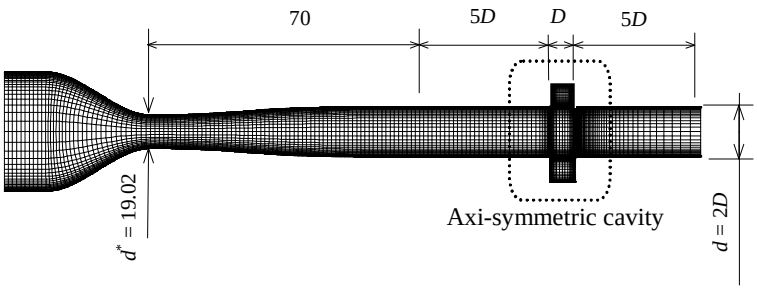

(a) Computational grids (Unit : mm)

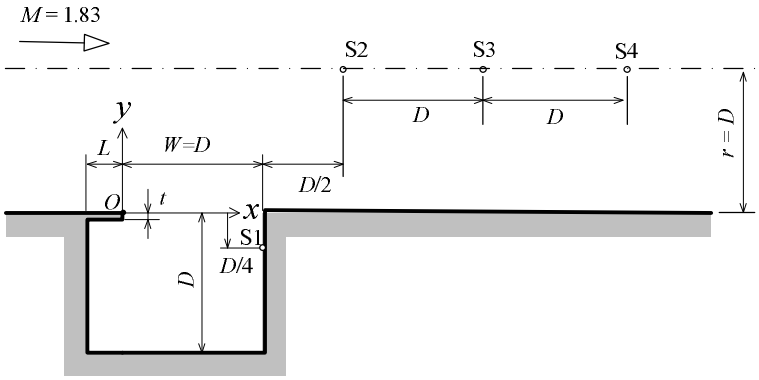

(b) Details of axi-symmetric cavity configuration

Figure A.1: Computational domain

feedback loop within the cavity. Here, f represents the dominant frequency, which is equal to 36.5 kHz (see Fig.A.2(b)). It is observed that a compression wave (CW) from the trailing edge moves upstream as time proceeds (Fig.A.3(a)). The upstream compression wave (UW) impinges on the leading edge (Fig.A.3(b)) and the reflection occurs (Fig.A.3(c)). The reflected wave (RW) disturbs the shear layer near the leading edge. This disturbance regenerates instability waves in the shear layer. While the shear layer reattaches at the rear wall, the compression wave (CW) is generated due to the impingement of instability waves on the wall as shown in Fig.A.3(d). The compression wave thus produced, moves upstream and becomes the upstream compression wave (UW) as shown in Fig.A.3(d). This completes the formation of the feedback loop.

Figures A.4 shows streamlines of the flowfield in case without control. It is observed that there is no tendency to develop a single, large vortex in the cavity.

Figure A.5 shows time history of static pressure at positions S2, S3 and S4 along the centerline of main flow without control. It shows that amplitudes of oscillations are significant in case of flow without control. However, the oscillations are larger at the position S2 (Fig.A.5(a)) than that of at S3 (Fig.A.5(b)) and S4(Fig.A.5(c)). Figure A.6 shows power spectrum density in case without control at each position. There are strong dominant peak frequencies in the flowfield without control.

A.3.2 Flowfield with control

Time histories of static pressure and power spectrum densities are shown in Figs. A.7 and A.8 in case with control, respectively. It is observed that amplitudes of oscillations at the positions S2, S3 and S4 are reduced when the flow is controlled by a plenum chamber covered partially by a solid surface as shown in Fig.A.7. However, distributions of power spectrum densities in Fig.A.8 show that there are some dominant peak frequencies at the positions S2, S3 and S4.

Figure A.9 shows time history of static pressure and power spectrum density at S1 in the cavity with control. A significant amount of reduction of the amplitude of oscillations is obtained as shown in Fig.A.9(a). Distribution of power spectrum density is shown in Fig.A.9(b) and there is no dominat peak frequency at the position S1 in the cavity with control. Here, f_c represents the frequency in case with control. Therefore, a cavity covered partially by a solid surface can reduce the pressure fluctuations not only at the region of main flow of axi-symmertic nozzle (Figs.A.7and A.8) but also at the inside position of the cavity (Fig.A.9).

Figure A.10 shows density contours for the cavity with control. There exist

a stable shear layer with no compression waves and no feedback loop as shown in Fig.A.10. The significant reductions of cavity-induced pressure oscillations that obtained by the present control device can be explained from the fact that the upstream compression waves that impinges on the front wall of the cavity below the leading edge surface cannot disturb the shear layer immediately after the reflection. It is found from Fig.A.10 that the compression wave becomes weaker when the flow is controlled by a solid surface fitted at the leading edge of the cavity. The weaker compression waves cannot disturb the shear layer strongly enough to regenerate the instability waves in the shear layer. Therefore, a reduction of oscillations (Fig.A.9(a)) and a more stable shear layer was found for a cavity with control as shown in Fig.A.10.

Figure A.11 shows streamlines for the cavity with control. It is observed that there is also no tendency to develop a single, large vortex in the cavity.

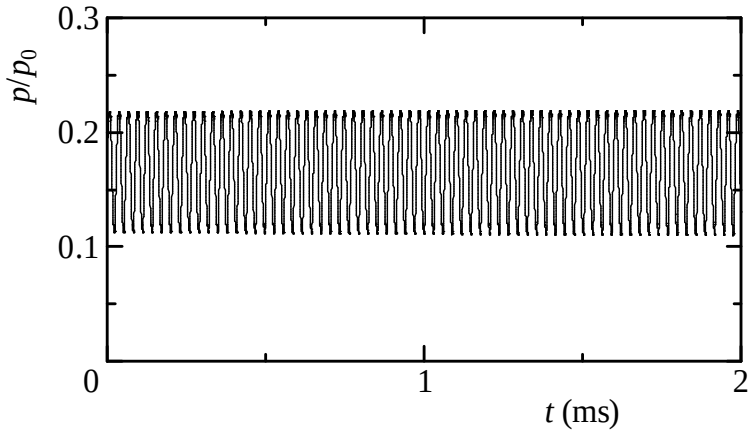

(a) Time history of static pressure

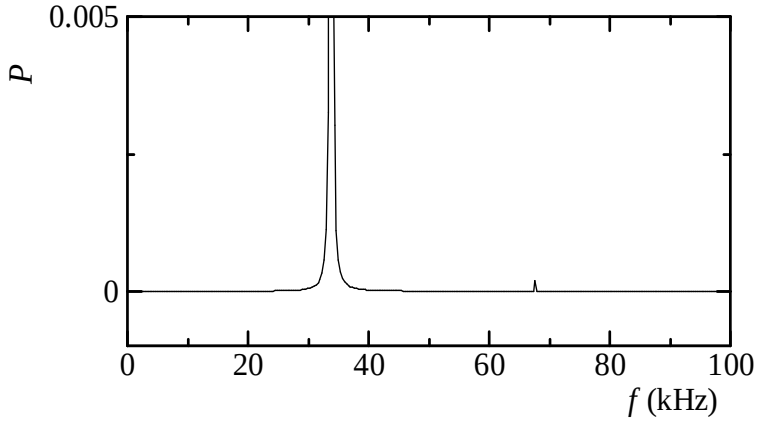

(b) Distribution of power spectrum density

Figure A.2: Time history of static pressure and distribution of power spectrum density (without control)

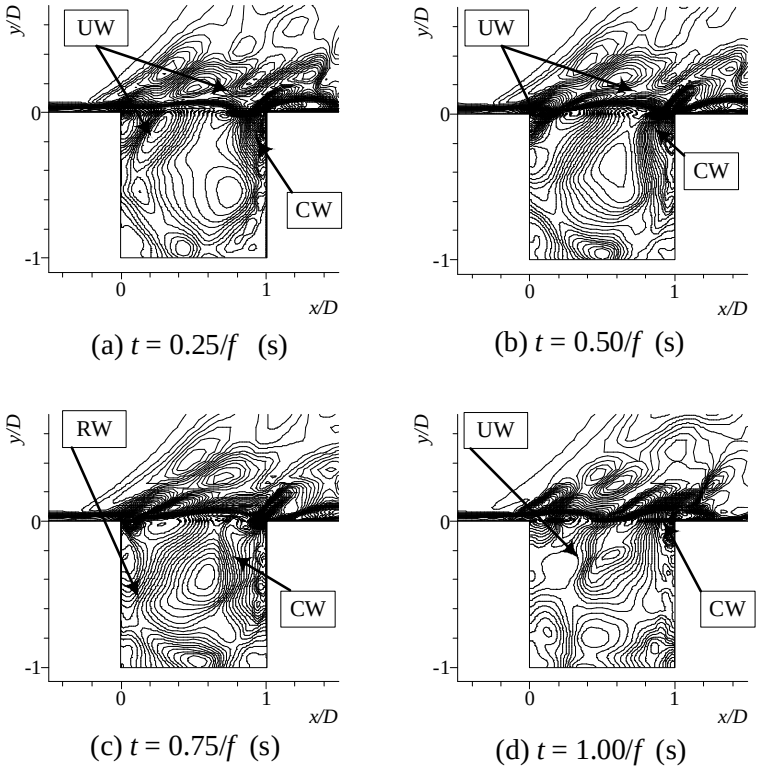

Figure A.3: Contour maps of density (without control).

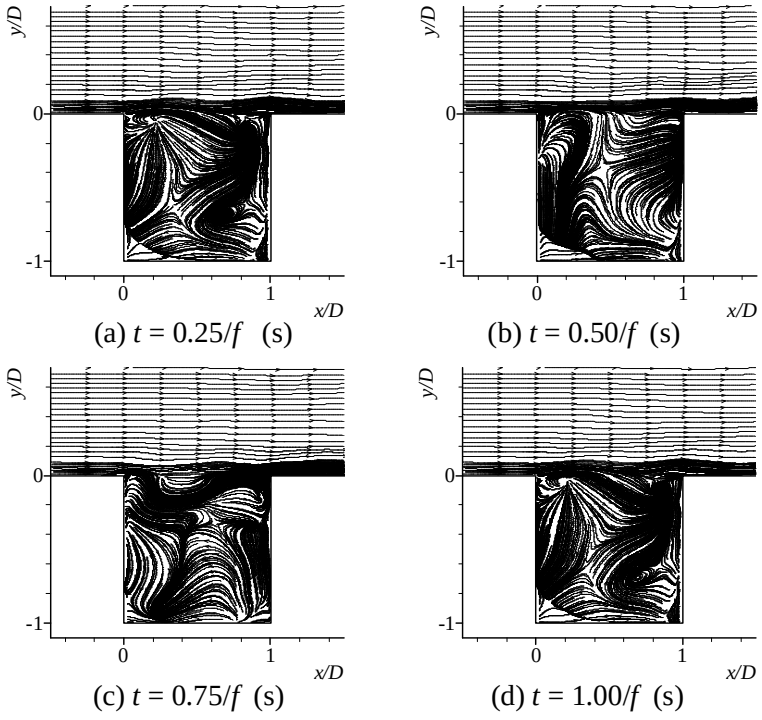

Figure A.4: Streamline (without control).

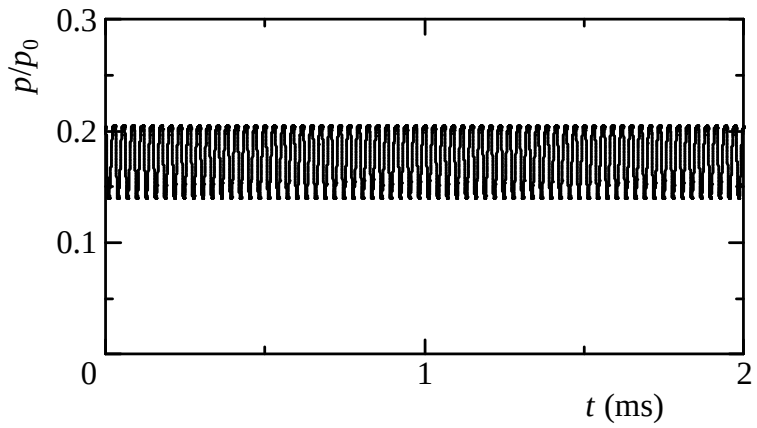

(a) S2

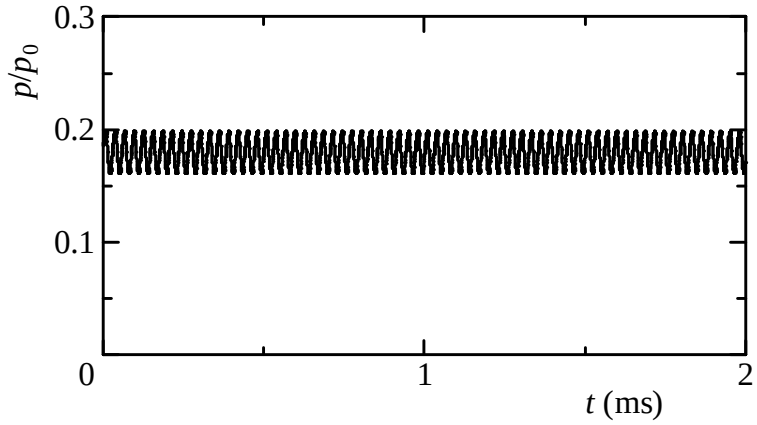

(b) S3

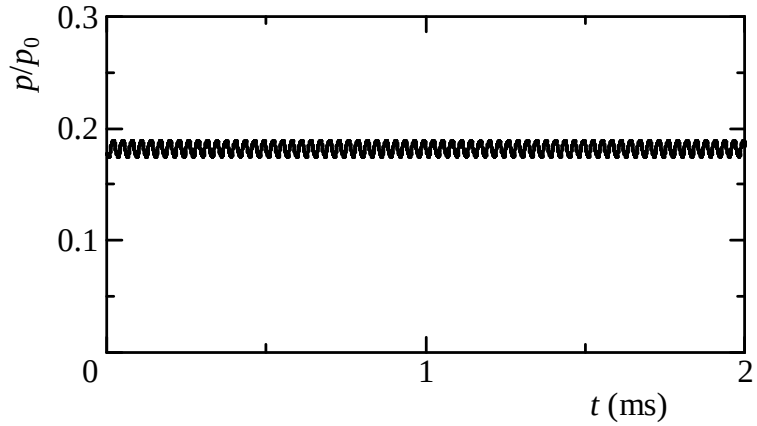

(c) S4

Figure A.5: Time histories of static pressure (without control).

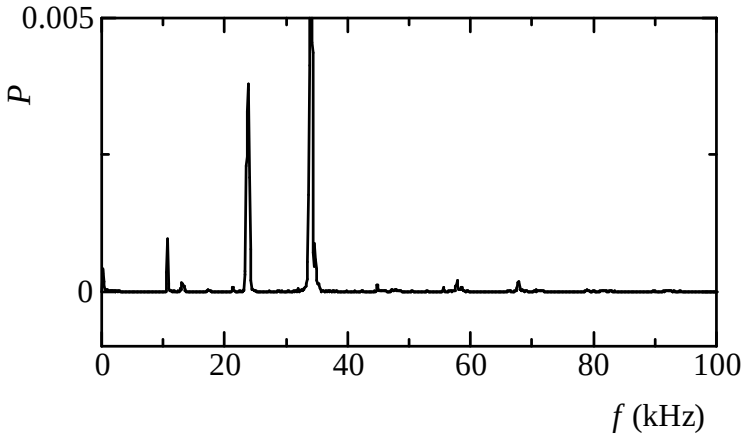

(a) S2

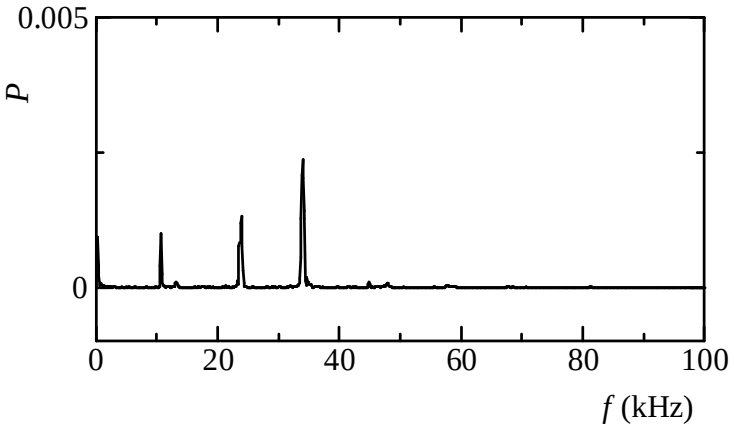

(b) S3

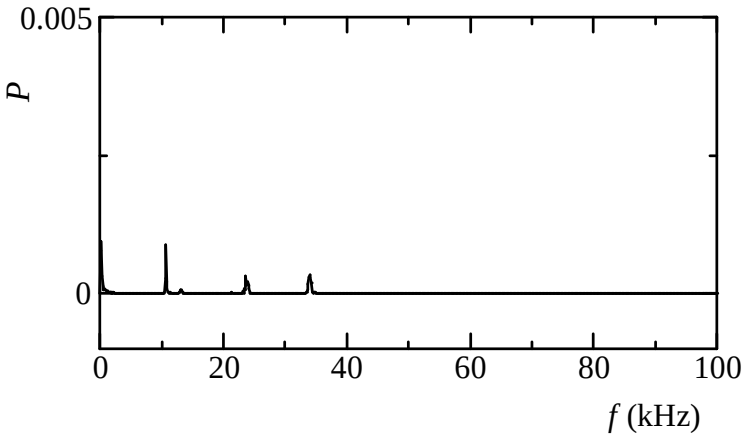

(c) S4

Figure A.6: Distributions of power spectrum density (without control).

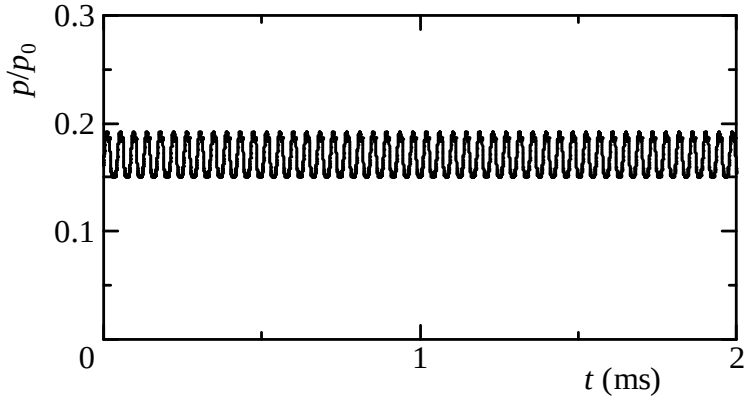

(a) S2

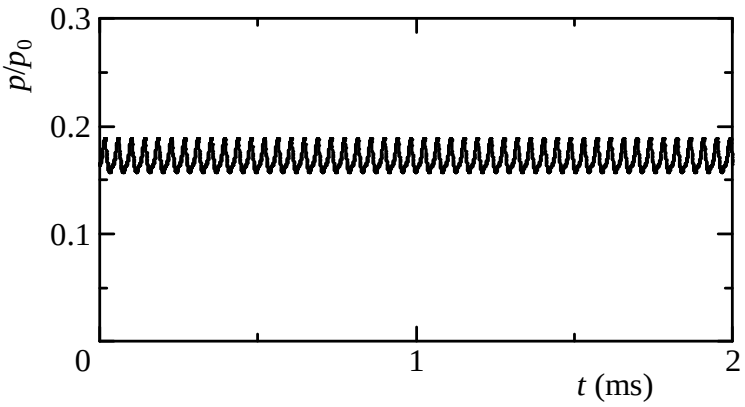

(b) S3

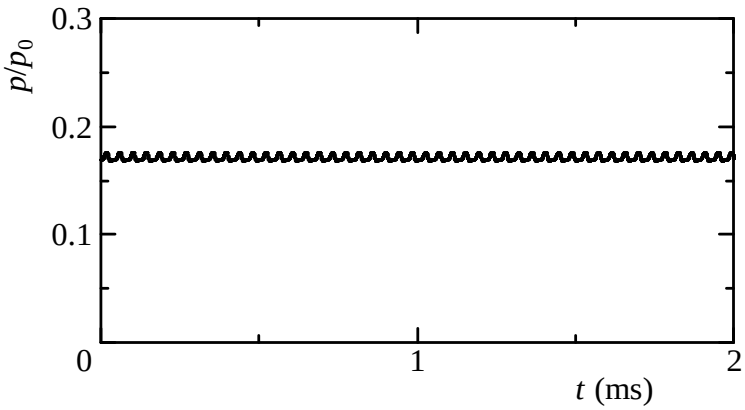

(c) S4

Figure A.7: Time histories of static pressure (with control).

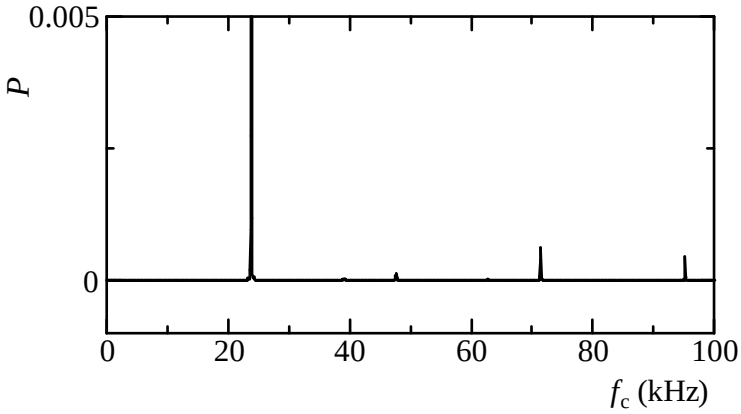

(a) S2

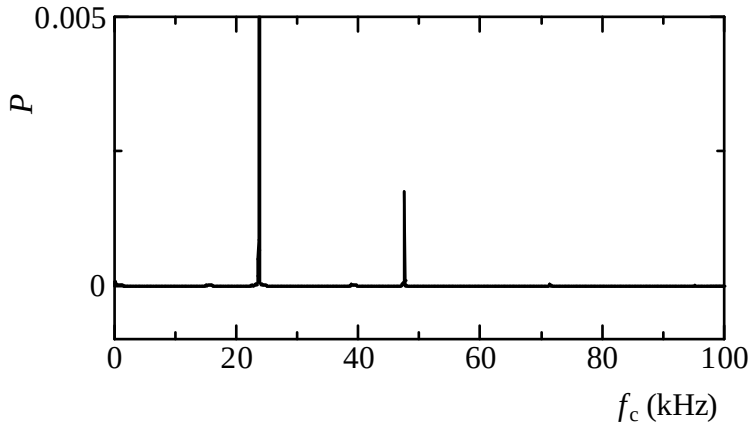

(b) S3

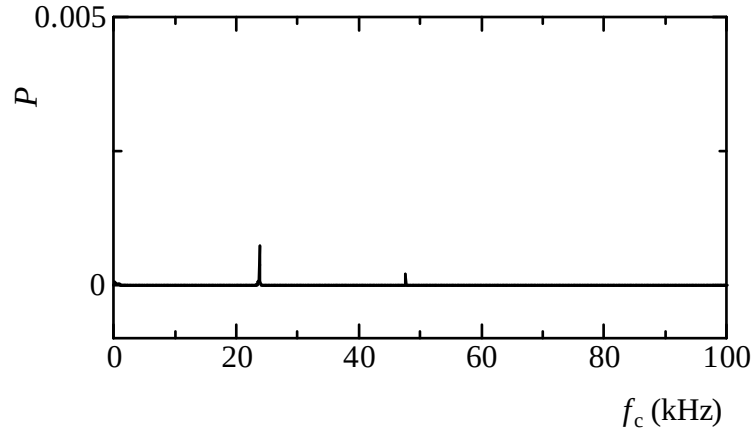

(c) S4

Figure A.8: Distributions of power spectrum density (with control).

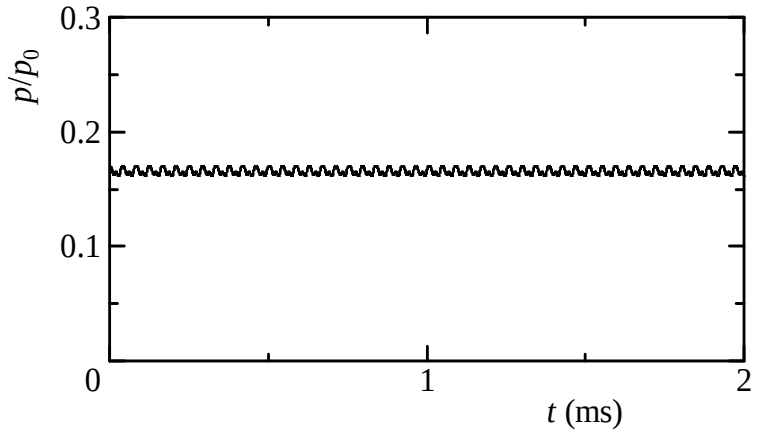

(a) Time history of static pressure

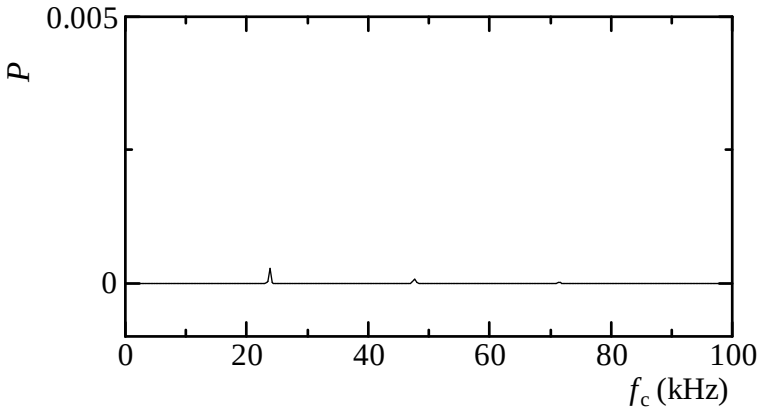

(b) Distribution of power spectrum density

Figure A.9: Time history of static pressure and distribution of power spectrum density (with control)

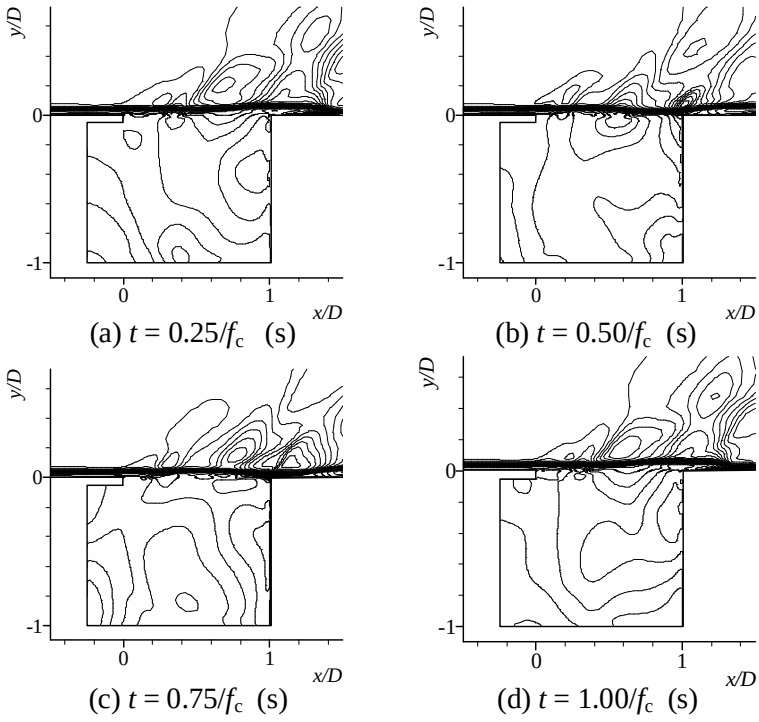

Figure A.10: Contour maps of density (with control).

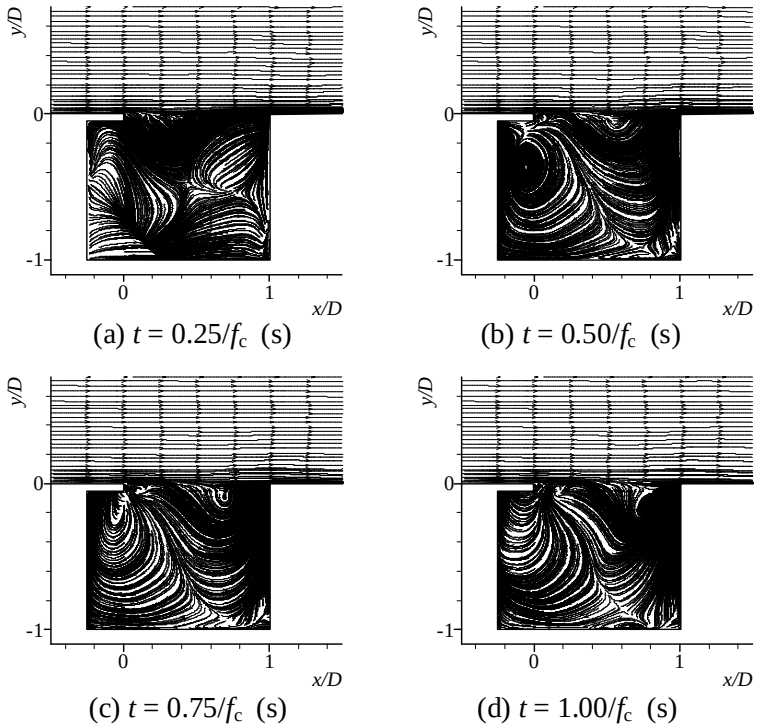

Figure A.11: Streamline (with control).

A.4 Summary

A computational study has been carried out for a supersonic two-dimensional flow at Mach number 1.83 at the entrance of a straight channel connected to an axi-symmetric nozzle. A passive control method consisted of a square cavity covered partially by a solid surface was investigated to control the oscillations in a supersonic free stream flow. The results showed that the amplitudes of oscillations were high in case of flow through axi-symmetric nozzle without control. The proposed control device can reduce the amplitudes of oscillations significantly not only at the region of main flow of axi-symmertic nozzle but also at the inside position of the cavity. However, the distributions of power spectrum densities showed some dominant peak frequencies in the flow field at the region of main flow.

REFERENCES

[1] Krishnamurty, K., Acoustic radiation from two dimensional rectangular cutouts in aerodynamic surfaces, NACA TN-3487, 1955.

[2] Roshko, A., Some measurements of flow in a rectangular cutout, NACA TN-3488, 1955.

[3] Rossiter, J.E., Wind-tunnel experiments on the flow over rectangular cavities at subsonic and transonic speeds, ARC RM-3438, 1964.

[4] Heller, H.H, Bliss, D.B., The physical mechanism of flow-induced pressure fluctuations in cavities and concepts for their suppression, AIAA Paper 75-491, 1975.

[5] Wilcox, FJ Jr., Passive venting system for modifying cavity flow-fields at supersonic speeds, AIAA Journal, 26(3), 1988, 374-76.

[6] Stallings, R.L., Plentovich, E.B., Tracy, M.B., Hemsch, M.J., Effect of passive venting on static pressure distributions in cavities at subsonic and transonic speeds, NASA TM-4549, 1994.

[7] Shaw, L., Clark, R., Talmadge, D., F-111 Generic weapons bay acoustic environment, Journal of Aircraft, 25(2), 1988, 147-153.

[8] Chokani, N., Kim, I., Suppression of pressure oscillations in an open cavity by passive pneumatic control, AIAA paper 91-1729, 1991.

[9] Sarno, R., Franke M., Suppression of flow-induced pressure oscillations in cavities, Journal of Aircraft, 31(1), 1994, 90-96.

[10] Ukeiley, L.S., Ponton, M.K., Seiner, J.M., Jansen, B., Suppression of pressure loads in cavity flows, AIAA Journal, 42(1), 2004, 70-79.

[11] Zhang, X., Chen, X., Rona, A., Edwards, J., Attenuation of cavity flow oscillation through leading edge flow control, Journal of Sound and Vibration, 221(1), 1999, 23-47.

[12] Smith, R.A., Gutmark, E., Schadow, K.C., Mitigation of pressure oscillations induced by supersonic flow over slender cavities, AIAA Paper 90-4019, 1990.

[13] Smith, B.R., Welterlen, T.J., Maines, B.H., Shaw, L.L., Stanek, M.J., and Grove, J.E., Weapons bay acoustic suppression from rod spoilers, AIAA Paper 2002-0662, 2002.

[14] McGrath, S.F. and Shaw, L.L., Jr., Active Control of Shallow Cavity Acoustic Resonance, AIAA 96-1949, June 1996.

[15] Shaw, L., Active control for cavity acoustics, AIAA 98-2347, June 1998.

[16] Mendoza, J.M. and Ahuja, K.K., Cavity noise control through upstream mass injection from a coanda surface, AIAA 96-1767, May 1996.

[17] Hsu, J.S. and Ahuja, K.K., Cavity noise control using Helmholtz resonators, AIAA 96-1675, May 1996.

[18] Lamp, A.M. and Chokani, N., Computation of cavity flows with suppression using jet blowing, Journal of Aircraft, 34(4), 1997, 545-551.

[19] Zhuang, N., Alvi, F.S., Alkislar, M.B., Shih, C., Sahoo, D., and Annaswamy, A.M., Aeroacoustic properties of supersonic cavity flows and their control, AIAA 2003-3101, May 2003.

[20] Clark, R.L., Weapons bay turbulence reduction techniques, Flight Dynamics Lab., AFFDL TM-75-147-FXM, Dec. 1975

[21] Kegerise, M.A., Spina, E.F., and Cattafesta, L. N. III, An experimental investigation of flow-induced cavity oscillations, AIAA Paper 99-3705, June 1999.

[22] Cattafesta, L.N., III, Garg, S., Kegerise, M.A., and Jones, G.S, Experiments on compressible flow-induced cavity oscillations, AIAA 98-2912, June 1998.

[23] Jeng, Y.N., Payne, U.J., Numerical study of a supersonic open cavity flow and pressure oscillation control, Journal of Aircraft, 32(2), 1995, 363-369.

[24] Rizzetta, D.P., Visbal, M.R., Large-eddy simulation of supersonic cavity flowfields including flow control, AIAA Journal, 41(8), 2003, 1452-1462.

[25] Mongeau, L., Kook, H., and Franchek, M.A., Active control of flow-induced cavity resonance, AIAA 98-2349, 1998.

[26] Shaw, L. and Northcraft, S., Closed loop active control for cavity resonance, AIAA 99-1902, May 1999. Also see Rothfuss, D.A. and Northcraft, S.A., Active control of weapons bay acoustics, AFRL-VA-WP-TR-1998-3039, June 1998.

[27] Vakili, A.D., and Gauthier, C., Control of cavity flow by upstream mass-injection, Journal of Aircraft, 31(1), 1994, 169-174.

[28] Stanek, M., Raman, G., Kibens, V, Ross, J., Odedra, J., and Peto, J., Control of cavity resonance through very high frequency forcing, AIAA 2000-1905, June 2000.

[29] Cattafesta, L.N., Garg, S., Choudhari, M., and Li, F., Active control of flow-induced cavity resonance, AIAA 97-1804, June 1997. Also see active suppression of shear-layer/cavity resonance interactions, NAS2-14248, May 1997.

[30] Baysal, O., Yen, G.W., and Fouladi, K., Navier-Stokes computations of cavity aeroacoustics with suppression devices, Journal of Vibration and Acoustics, 116, 1994, 105-112.

[31] Franke ME, Carr DL. Effect of geometry on open cavity flow-induced pressure oscillations. AIAA Paper 75-492, 1975.

[32] Dix, R.E., Butler, C., Cavity aeroacoustics, Proceedings of Store Carriage, Integration and Release Conference, Bath, U.K., The Royal Aeronautical Society, April 1990.

[33] Cattafesta, L., Williams, D., Rowley, C., and Alvi, F., Review of active control of flow-induced cavity resonance, AIAA Paper 2003-3567, 2003.

[34] Setoguchi, T., Alam, M.M., Matsuo, S., Teramoto, K., and Yu, S., A numerical study on passive control of cavity- induced pressure fluctuations in two-dimensional supersonic flow, International Journal of Turbo and Jet Engines, 23(3), 2006, 155-164.

[35] Alam, M.M., Matsuo, S., Teramoto, K., Setoguchi, T. and Kim, H.D., Proc. of the 5th Asian-Pacific Conference on Aerospace Technology and Science, CD-ROM, Guilin, China, 30 Oct.-3 Nov. 2006.

[36] Matsuo, S., Alam, M.M., Setoguchi, T., Kim, H.D., Yu, S., A new passive method of controlling cavity-induced pressure oscillations, Proceedings of the

8th International Symposium on Experimental and Computational Aerothermodynamics of Internal Flows, (ISAIF8), Ecole Centrale de Lyon, France, July 2-5, 2007.

[37] Heller, H.H., Holmes, D.G., and Covert, E.E, Flow induced pressure oscillations in shallow cavities, Journal of Sound and Vibration, 18(4), 1971, 545-553.

[38] Ben-Yakar, A, Hanson, R.K., Cavity flame-holders for ignition and flame stabilization in scramjets: An overview. Journal of Propulsion and Power, 17(4), 2001, 869-877.

[39] Ukeiley, L., Ponton, M., Seiner, J., and Jansen, B., Suppression of pressure loads in cavity flows, AIAA Paper 2002-0661, 2002.

[40] Williams, D.R., Fabris, D., Morrow, J., Experiments on controlling multiple acoustic modes in cavities, AIAA Paper 2000-1903, 2000.

[41] Rockwell, D., Naudascher, E., Review - self-sustaining oscillations of flow past cavities. ASME Transactions, Journal of Fluids Engineering, 100, 1978, 152-165.

[42] Karamcheti, K., Bauer A.B., Shields, W.L., Stegen, G.R., and Woolley, J.P., Some features of an edge tone flow field, NASA SP 207, 1969, 275-304.

[43] Woolley, J.P., and Karamcheti, K., Role of jet stability in edge-tone generation, AIAA Journal, 12(11), 1974, 1457-1458.

[44] King, J.L., Boyle, P., Ogle, J.B., Instability in slotted wall tunnels, Journal of Fluid Mechanics, 4, 1958, 283-305.

[45] Martin, W.W., Naudascher, E.N, Padmanabhan, M., Fluid dynamic excitation involving flow instability, Proc. ASCE, Journal of Hydraulics Div., HY6, June 1975, 681-698.

[46] Rockwell, D., Prediction of oscillation frequencies for unstable flow past cavities, ASME Journal of Fluids Engineering, 99, 1977, 294-300.

[47] Reeder, M., Subramanian, C., Mean and instantaneous flow properties of an object exiting a cavity, AIAA Paper 2003-3723, 2003.

[48] Murray, R., and Elliott, G., Characteristics of the compressible shear layer over a cavity, AIAA Journal, 39(5), 2001, 846-856.

[49] Zhang, X., Edward, J. A., An investigation of supersonic oscillatory cavity flows driven by thick shear layers, Aeronautical Journal, 1990, 355-364.

[50] Unalmis, O.H., Clemens, N.T., and Dolling, D.S., Experimental study of shear-layer/acoustics coupling in Mach 5 cavity Flow, Journal of Aircraft, 39(2), 2001, 242-252.

[51] Schlichting, Herman, Boundary-layer theory, Seventh Edition, McGraw-Hill Publishing, 1979, 5-45.

[52] Jeng, Y.N., Wu, T.J., Numerical study of supersonic open cavity flow with geometric modification on aft bulkhead, AIAA paper 92-2627, 1992.

[53] Zhang, X., Edward, J.A., Computational analysis of unsteady supersonic cavity flows driven by thick shear layers, Aeronautical Journal, 92, 1988, 365-374

[54] Zhang, X., Edward, J.A., Analysis of unsteady supersonic cavity flow employing an adaptive meshing algorithm, Computers and Fluids, 25(4), 1995, 373-393.

[55] Tam, C.-J., Orkwis, P.D. and Disimile, P.J., Supersonic open cavity flow physics ascertained from algebraic turbulence model simulations, AIAA Paper 96-0075, 1996.

[56] Chakravarthy, S., Peroomian, O., and Sekar, B., Some internal flow applications of a unified-grid CFD methodology, AIAA Paper 96-2024, 1996.

[57] Rockwell, D., Naudasher, E., 1979, Self sustained oscillations of impinging free shear layers, Annual Review of Fluid Mechanics, 11, 1979, 67-94.

[58] Tam, C.J, Orkwis, P.D, Disimile, P.J., Algebraic turbulence model simulations of supersonic open-cavity flow physics, AIAA Journal, 34(11), 1996, 2255-2260.

[59] Nishioka, M., Asai, T., Sakaue, S., Shiraji, K. On the mechanism of supersonic cavity flow oscillations. Proc. 5th Experimental Heat Transfer, Fluid Mechanics and Thermodynamics Conference, Thessaloniki, Greece, 2001, 153-163.

[60] Nishioka, M, Asai, T., Sakaue, S., Shirai, K., Some thoughts on the mechanism of supersonic cavity Flow oscillation, Part 2 A new formula for the oscillation frequency, Journal of Japan Society of Fluid Mechanics, 21, 2002, 368-378.

[61] Shapiro, A.H., Free surface water table, physical measurements in gas dynamics and combustion, Edited by Ladenburg, R.W., Lewis, B., Pease, R.N., Taylor, H.S., 1954.

[62] Schindel, L.H., Store separation, Advisory Group for Aerospace Research and Development (AGARD), AGARDograph No. 202, 1975.

[63] Bueno, P., Unalmis, O., Clemens, N., Dolling, D., The effects of upstream mass injection on a Mach 2 Cavity Flow, AIAA Paper 2002-0663, 2002.

[64] Grove, J., Shaw, L., Leugers, J., Akroyd, G., UASF/RAAF F-111 Flight test with active separation control, AIAA Paper 2003-0009, 2003.

[65] Samimy, M. and Kastner, J., Effects of forcing frequency on the control of an impinging high speed jet, AIAA Paper 2003-0006, 2003.

[66] Adam, S., Numerische und experimentelle untersuchung instationärer Düsenströmungen mit energiezufuhr durch homogene kondensation, Dissertation, Fukaltät für Maschinenbau, Universität Karlsruhe (TH), Germany, 1999.

[67] Sislian, J.P., Condensation of water vapor with or without a carrier gas in a shock tube, UTIAS Report, No. 201, 1975.

[68] Michael, H., Instationäre Phänomene in homogen/heterogen kondensierenden Duüsen- und Turbinenströmungen, Dissertation, Fakultät für Maschinenbau, Universität Karlsruhe(TH), Germany, (1999).

[69] Frenkel, J., Kinetic Theory of Liquids, (1946), Oxford University Press.

[70] Otobe, Y., Matsuo, S., Tanaka, M., Kashimura H. and Setoguchi, T., A study on characteristics of under-expanded condensing Jet, JSME International Journal, Series B, 49(4), 2006, 1165-1172.

[71] Harten, A., A high resolution scheme for the computation of weak solutions of hyperbolic conservation laws, Journal of Computational Physics, 49, 1983, 357-393.

[72] Godunov, Sergie, K., A difference scheme for numerical solution of discontinuous solution of hydrodynamic equations, Math. Sbornik, 47, 1959, 271-306, translated US Joint Publ. Res. Service, JPRS 7226, 1969.

[73] Yee, H.C. A class of high-resolution explicit and implicit shock capturing methods. NASA TM-89464, 1989.

[74] Jones, W.P. and Launder, B.E., The prediction of laminarization with a two-equation model of turbulence. International Journal of Heat and Mass Transfer, 15, 1972, 301-314.

[75] Wilcox, D.C., Reassessment of the scale determining equation for advanced turbulence models, AIAA Journal, 26, 1988, 1299-1310.

[76] Speziale, C.G, Abid, R. and Anderson, E.C., Critical evaluation of two-equation models for near-wall turbulence. AIAA Journal, 30, 1992, 324-331.

[77] Goldberg, U.C., Toward a pointwise turbulence model for wall-bounded and free shear flows, ASME Transactions, Journal of Fluids Engineering, 116, 1994, 72-76.

[78] Goldberg, U.C., Exploring a three-equation $R-k-\epsilon$ turbulence model, ASME Transactions, Journal of Fluids Engineering, 118, 1996, 795-99.

[79] Heiler, M., Instationäre phänomene in homogen/heterogen kondensierenden duüsen- und turbinenströmungen. Dissertation, Fakultät für Maschinenbau, Universität Karlsruhe, Germany, 1999.

[80] Kim, J., Moin, P., and Moser, R., Turbulence statistics in fully developed channel flow at low Reynolds number. Journal of Fluid Mechanics, 177, 1987, 133-166.

[81] Durbin, P.A., Near-wall turbulence closure modeling without damping functions. Theoretical and Computational Fluid Dynamics, 3, 1991, 1-13.

[82] Suga, K., Nagaoka, M., Horinouchi, N., Abe, K. and Kondo, Y., Application of a three equation cubic eddy viscosity model to 3-D turbulent flow by the unstructed grid method. In Hanjalic, K., Nagano, Y. and Tsuji, T., editors, 3:rd Int. Symp. on Turbulence, Heat and Mass Transfer, Aichi Shuppan, Nagoya 2000, 373-381.

[83] Pulliam, T.H., and Chaussee, D.S., A Diagonal form of an implicit approximate-factorization algorithm, Journal of Computational Physics, 39, 1981, 347-363.

[84] Maccormack, R.W., Paullay., Computational efficiency achieved by time splitting of finite difference operators, AIAA-1972-154, 1972.

[85] Goede, E.D, A time splitting method for three dimensional shallow water equations, The Center for Mathematics and Computer Science, Stichting Mathematisch Centrum, Report NM-R9013, Amsterdam.

[86] Wicker, L.J., Skamarock, W., Time-splitting methods for elastic models using forward time schemes, Monthly Weather Review, 130, 2002, 2088-2097.

[87] Sakamoto, K., Matsunaga, K., Fujii, K., Tamura, Y., Experimental investigation of supersonic internal cavity flows, AIAA paper 95-2213, 1995.

[88] Quinn, B., Flow in the orifice of a resonant cavity, AIAA Student Journal, 1, 1963, 1-5.

[89] Ponton, M.K., Seiner, J.M., The effects of nozzle exit lip thickness on plume resonance, Journal of Sound and Vibration, 154(3), 1992, 531-49.

[90] Raman, G., Cessation of screech in underexpanded jets. Journal of Fluid Mechanics, 336, 1997, 69-90.

[91] Jorgenson, P.C.E., Loh, C.Y., Computing axisymmetric jet screech tones using unstructured grids. AIAA Paper 2002-3889, 2002.

[92] Tam, C.K.W., Block, P.J.W., On the tones and pressure oscillations induced by flow over rectangular cavities. Journal of Fluid Mechanics, 89, 1978, 373-99.

[93] Takakura, Y., Suzuki, T., Higashino, F, Yoshida M, Numerical study on supersonic internal cavity flows : What causes the pressure fluctuations?. AIAA Paper 99-0545, 1999.

[94] Sasoh, A., Matsuoka. K., Nakashio, K., Timofeev, E., Takayama, K., Voinovich, P., Saito, T., Hirano, S., Ono, S., Makino, Y., Attenuation of weak shock waves along pseudo-perforated walls, Shock Waves, 8, 1998, 149-159.

[95] Khan, M.T.I., Seto, K., Xu, Z. and Ohta, H., The effect of spherical surface on noise suppression of a supersonic jet, Journal of Thermal Science, 12(2), 2002, 144-150.

[96] Dussauge, J-P, Dupont, P. and Debieve, J-F, Unsteadiness in shock wave

boundary layer interactions with separation, Aerospace Science and Technology, 10(2), 2006, 85-91.

[97] Dolling, D.S., Fifty years of shock wave/boundary layer interaction research: What next?, AIAA Journal, 39(8), 2001, 1517-15-31.

[98] Yamane, R., Oshima, S., Nakamura, Y., Ishii, T. and Park, M.K., Numerical simulation of pseudo-shock in straight channels, JSME lnt. Journal, Series B, 38(4), 1995, 549-554.

[99] McCormick, D.C., Shock/boundary-layer interaction control with vortex generators and passive cavity, AIAA Journal, 31(1), 1993, 91-96.

[100] Asbury, S.C., Hunter, C.A. and Gunther, C.L., A passive cavity concept for improving the off-design performance of fixed geometry exhaust nozzles, AIAA-96-2541, 1996.

[101] Pandey, K.M. and Rathakrishnan, E., Annular cavities for base flow control, Int. Journal of Turbo and Jet Engines, 23(2), 2006, 113-127.

[102] Charwat, A.F., Ross, J.N., Dewey, F.C. and Hitz, J.A., An investigation of separated flows - Part I: The pressure Field, J. the Aerospace Sciences, 28(6), 1961, 457-470.

[103] Hahn, M., Experimental investigation of separated flow over a cavity at hypersonic speed, AIAA Journal, 7(6), 1969, 1092-1098.

[104] Seddon, J. and Goldsmith, E.L., Intake Aerodynamics, AIAA Education Series, 1985.

[105] Dougherty, N.S., Hot, J.B., Nesman, T.E. and Farr, R.A., Time-accurate Navier-Stokes computational of self-excited two-dimensional unsteady cavity flows, AIAA-90-0691, 1990.

[106] Wegener, P.P., Mack, L.M., Condensation in supersonic hypersonic wind tunnels, Advances in Applied Mathematics, 5, Academic Press, 1958, 307-447

[107] Matsuo, K., Kawagoe, S., Sonoda, K., Sakao, K., Studies of condensation shock waves (part 1, mechanism of their formation), Bulletin of JSME, 28, 1985, 2577-2582.

[108] Schnerr, G.H., Homogene kondensation in stationaeren transsonischen stroemungen durch Laval-duesen und um Profile, Hab. schrift, Universitaet Karlsruhe, 1986.